Periodic Structure in Graded-Index Multimode Fiber

Su Lei

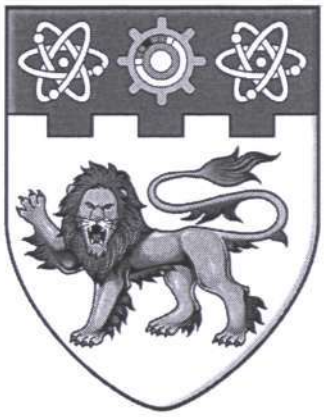

School of Electrical & Electronic Engineering

A thesis submitted to the Nanyang Technological University

in fulfillment of the requirement for the degree of

Doctor of Philosophy

2005

Statement of Originality

I hereby certify that the work embodied in this thesis is the result of original research and has not been submitted for a higher degree to any other University or Institution.

Oct. 21, 2005 Su Lei

TABLE OF CONTENTS

To my family

ACKNOWLEDGMENT

On completion of this dissertation, I feel indebted to many people who have been so generous with their help. Their expertise rendered vivid color to each single word in this work. Otherwise it would not have been possible.

First I would like to express my very sincere gratefulness to my supervisor, Associate Professor Lu Chao, who has served as a beacon of knowledge, guidance, and encouragement to me and many other students and researchers at the Nanyang Technological University and the Lightwave Department. I thank him for accepting and getting me involved in this interesting research, especially at the hardest time when I started. Without his endless support, none of this research work could be possible.

Also I would like to take this opportunity to thank Professor Chiang Kin-Seng, at City University of Hong Kong. His generosity and patience, as well as his thoughtful guidance and valuable advice, made me capable of composing this dissertation.

My thanks go to staffs and students at NTRC, Nanyang Technological University. To Associate Professor Shum Ping, for providing continuous support during my graduate study. To Dr. Dong Xinyong, Dr. Dong Hui, Dr. Xia Li, Mr. Yan Min, Mr. Tang Ming, Mr. Liu Duan, and Mr. Yuan Hai, for those inspirational discussions. To

NTRC laboratory technicians: Mr. Poh Khoon Yong, Ms. Wee-Chew Lee Foong, Ms. Thung Lina, and Mr. Chong Lui Tat, for their kind assistance. To all others who contributed to my research and to my experience as a graduate student.

I must thank all my colleagues and friends at Lightwave Department, Institute for Infocomm Research, especially Mr. Ng Jun Hong, Dr. Hao Jianzhong, Dr. Wang Yixin, Mr. Varghese Paulose, Dr. Yang Xiufeng, Dr. Chen Jian, Dr. Wen Yangjing, Mr. Li Zhaohui, Mr. Xu Zhaowen, Miss Xie Bing and Mr. Wang Ying for helping me out in several tasks in the laboratory, entertainment, and friendship.

I am grateful to my grandma Daoyu, my parents Qiyu and Zujin, my wife Yalan and my brother Zhang Chi, for their love, and understanding of my absence due to this thesis work.

Finally, I have to thank Nanyang Technological University for offering me a research scholarship during my graduate studies.

SUMMARY

This thesis studies the periodic structures in graded-index multimode fibers (GRIN MMF), including fiber Bragg grating (FBG), long period grating (LPG), and periodic microbend. Their fabrication processes, mode coupling analyses, and applications are investigated both theoretically and experimentally.

Multimode fiber Bragg grating (MMFBG), written with ultraviolet (UV) light, is investigated. Mode coupling and reflection spectrum of the MMFBG are studied. The responses of MMFBG to strain and temperature changes are examined.

It is shown that in LPG formed in GRIN MMF strong mode couplings take place when the pitch of the grating is equal to a specific value, known as the critical spatial period of the fiber. LPG in GRIN MMF is fabricated by deforming the geometry of the fiber periodically with a focused CO_2-laser beam. Transmission characteristic experiments conducted on the LPG confirm the value of critical spatial period. The responses of the fabricated gratings to the axial strain and the change in the surrounding refractive index are measured and good sensitivities are achieved. Thus such MMF LPGs can be used as potential physical and chemical sensors.

A theoretical analysis of the mode coupling effects at a periodic microbend along a GRIN MMF is presented. By matching the incident and excited mode fields at the

microbend, the coupling coefficients among the guided modes at different microbending conditions are obtained. The theoretical results agree well with the experimental results from near-field measurements on a GRIN MMF subject to microbending. The applications of the theory, in explaining the behavior of microbend based optical fiber devices, are presented.

Based on the microbend theory, a microbend sensor, consisting of a single-mode fiber lead, a multimode sensing fiber, and a single-mode fiber Bragg grating, is proposed for simultaneous measurement of a mechanical parameter and temperature. The sensor is demonstrated experimentally with two demodulation schemes based on a broadband source and a tunable laser respectively. The sensor extends the capacity of a conventional microbend sensor and offers many additional advantages, including higher stability, higher sensitivity, single-end access, and superior multiplexing capability.

The spectral tuning ability of the MMFBG is exploited for implementation of wavelength-switchable erbium-doped fiber lasers. Two effective schemes have been demonstrated. Firstly and interestingly, the combination of a periodic microbend theory and the MMFBG is proposed to form the wavelength-switchable fiber laser. Secondly, a spatial excitation and filtering scheme is described to implement the laser. The wavelength for laser operation can be selected from more than 30 discrete wavelengths with 0.8-nm spacing over a wide wavelength range.

ABBREVIATIONS

ASE	Amplified Spontaneous Emission
AOM	Acousto-Optic Modulator
CTE	Coefficient of Thermal Expansion
CW	Continuous Wave
ECSL	External-Cavity Semiconductor Laser
EDF	Erbium-Doped Fiber
EDFA	Erbium-Doped Fiber Amplifier
EDFL	Erbium-Doped Fiber Laser
FBG	Fiber Bragg Grating
FFP	Fiber Fabry-Perot
FWHM	Full Width at Half-Maximum
GRIN	Graded Index
IMD	Intermodal Dispersion
ISO	Isolator
LD	Laser Diode
LPG	Long Period Grating
MB	Methylene Blue
MCVD	Modified Chemical Vapor Deposition
MMF	Multimode Fiber
MMFBG	Multimode Fiber Bragg Grating
OSA	Optical Spectrum Analyzer
PC	Polarization Controller
PCF	Photonic Crystal Fiber
POF	Plastic Optical Fiber
RI	Refractive Index

SI	Step Index
SMF	Single Mode Fiber
SMFBG	Single Mode Fiber Bragg Grating
UV	Ultra Violet
VCSEL	Vertical-Cavity Surface-Emitting Laser
WDM	Wavelength Division Multiplexing

LIST OF FIGURES

LIST OF TABLES

CHAPTER 1

INTRODUCTION

1.1 Overview of periodic structures in SMF

Periodic structures in optical fibers investigated in this thesis fall into three categories: short period grating (FBG), long period grating (LPG), and periodic microbend. The operational principles of them are all based on the phase matching of mode coupling. Formed with a period comparable to the light wavelength, an FBG leads to the mode coupling between counter-propagating modes, while LPG or periodic microbending structure introduces co-propagating mode coupling with a relatively large period. The major difference in the coupling mechanism between an LPG and a periodic micorbending structure is whether the fiber coating exists along the grating region. In an LPG, cladding modes are able to be effectively coupled with the core modes without the absorptive fiber coating. But for the microbend structure the cladding modes are immediately absorbed by the fiber coating, and therefore, ideally no more cladding power can couple back into fiber core again.

Periodic structures in single-mode fiber (SMF) have been widely investigated with extensive applications in optical communications and optical fiber sensors [1-4]. SMFs with FBG and LPG, in particular, have opened the door for a variety of optical

fiber devices that were not previously possible.

In telecommunications, FBG has been incorporated in optical devices simply to act as a wavelength selective reflector thereby transforming the device into a practical component with enhanced performance. One example of such applications is the fiber laser containing an FBG as the wavelength selection element. By using FBGs as wavelength-selective resonator mirrors and erbium-doped fiber as the gain medium, such cost-effective all fiber lasers can be constructed. Narrow-linewidth fiber lasers of this kind are suitable as externally-modulated continuous wave (CW) sources for gigabit/s transmission experiments [5, 6]. Besides, FBG serves as feedback mirrors in wavelength-stabilized semiconductor lasers [7], reflectors for double-passing the input signal in optical amplifications [6, 8], pump reflectors in phase conjugators [9], isolation filters in bidirectional lightwave transmission [10], filters in wavelength division multiplexing (WDM) multiplexers or de-multiplexers [11], and dispersion compensators in transmission [12, 13].

Apart from applications in telecommunications, fiber Bragg grating is recognized as a simple, intrinsic, and effective sensing element and has all the advantages normally attributed to fiber sensors [2, 14-16]. In addition, FBG has an inherent self referencing capability and is easily multiplexed in series along a single fiber. The basic principle of operation commonly used in a FBG-based sensor system is to monitor the shift in wavelength. When an FBG is subjected to strain or temperature

variation, the shift in Bragg wavelength serves as a measure of the environment parameters. Several FBG sensors with different Bragg wavelengths could be interrogated by inputting a broadband spectral light thus forming a distributed sensor network. Besides the sensing applications of a uniform FBG in strain and temperature measurement, specially structured FBGs are also proposed as sensing elements, including the chirped FBG and the etched FBG [2] [17], which allows the sensing of many other parameters.

LPGs in SMF were initially developed for the use as band-rejection filters [18], since they operates in the transmission mode. LPGs have also been used as gain-flattening equalizer for erbium-doped fiber amplifiers (EDFA) in telecommunication [19]. Most importantly, LPG presents unique potential in optical fiber sensing applications [20-25]. The center wavelength for the LPG resonance peak depends critically on the index difference between the core and the cladding, and thus any index variation caused by strain, temperature, or changes of the surrounding index, can lead to large shifts in resonance wavelength. Compared with FBG based strain and temperature sensors, LPG resonance at a given wavelength λ can have a very different sensitivity, depending on the fiber type and grating period. In addition, the responses of two resonance bands of the same LPG usually differ in magnitude, which makes LPG particularly useful for multi-parameter sensors [23, 26].

Periodic microbend structure in SMF has been used to form the single-mode fiber

LPG [3, 27], by considering that it induces the co-propagating mode coupling. Particularly, periodic microbending is effective in forming the LPG in those fibers that are not photosensitive or in those cases where the mode coupling efficiency needs to be tuned. Therefore, periodic microbending was proposed to implement fiber-optic modal coupler [28] and to form the LPG in the photonic crystal fiber (PCF) [29], where the conventional UV method is difficult to be used. In comparison with the applications of periodic microbend in MMF as intensity based mechanical sensors, SMF with periodic microbends is not widely used for sensing applications, because of its limited dynamic range [30].

1.2 Motivation

While the characteristics and applications of the periodic structure in SMF are investigated extensively, to date the only periodic structure in MMF that has been widely studied and commercialized is the MMF with periodic microbends. Only recently, grating structures in MMF began to receive attention and several works were reported on these topics.

In fact, the first MMFBG was reported when the holographic UV method was proposed for fabricating single-mode FBG [31]. As a matter of fact, MMFBG had been overlooked due to following reasons. Firstly, it was shown that an MMFBG displayed multiple transmission dips distributed over a wide wavelength range [31].

Compared with the absolutely single-wavelength reflection, the downside of the multiple reflections is that the absolute band rejection is impossible at a given wavelength. Therefore, MMFBG can not be used as a single-wavelength filter in the MMF transmission system. Secondly, MMFBG is difficult to be integrated with the SMF system due to the difficulties and losses at the SMF/MMF connection, which in a way limits the applications of the MMFBG. On the other hand, the large core of MMF allows the efficient coupling with other non-single-mode devices, and thus is advantageous if the optical sensors are made in MMF. Furthermore, the multiple reflection peaks or transmission dips in the spectrum of an MMFBG are due to the reflections to fiber modes, and hence the spectrum could be changed by varying the modal power distribution [32]. This interesting property allows MMFBG to be used as tunable filters and leads to novel MMFBG based devices in telecommunication. Therefore, by considering the current strong interest in the studies and applications of the FBG in SMF, further studies on the MMFBG and its applications would be highly useful.

As mentioned previously, LPGs formed in SMF [18] have been studied extensively over the recent years owing to their many applications in optical communications and optical fiber sensors. On the other hand, there has been little work on the study of LPGs fabricated in MMFs [33-35]. The reason is that an MMF LPG does not produce a useful filter response, i.e., a transmission spectrum that exhibits distinct rejection or passing bands. Published works on theoretical analyses

and experimental results are still fairly primitive. This is because the reported MMF LPG for sensor applications were formed using the UV-irradiation method [33, 34], and the mode coupling efficiency, which can be offered by a multimode fiber LPG written by the UV-irradiation method, is likely to be low as the UV irradiation can change only the refractive index of the fiber core [18, 33]. To get a strong mode coupling, a periodic change in the geometric structure of the fiber is desired [36]. Recently a CO_2 laser was proposed as an alternative method of fabricating LPGs and this has attracted considerable interests [37], which is capable of geometric deformation along the MMF. To date, CO_2 laser fabricated MMF LPGs have not been reported. Therefore, a study on LPGs in MMF, especially the MMF LPG fabricated using CO_2 laser irradiation, is desirable, and it could lead to interesting applications.

Periodic microbend structure in MMF has been fruitfully exploited and commercialized. The application of periodic microbending along an MMF can introduce significant radiation loss and mode coupling in the fiber. A number of fiber-optic sensors based on microbending loss have been developed for the measurement of pressure and displacement [38-41]. While there have been a number of studies on the bending and microbending effects in an optical fiber [42-47], such studies concern mainly the calculation of the radiation loss, i.e., the amount of power that is coupled from the guided modes to the radiation modes. Meanwhile, mode scramblers and many other kinds of microbend-based devices are commercially

available [6]. These applications bring forward a need for detailed theoretical analysis on the mode coupling mechanism in a periodic microbend in MMF.

The conventional microbend sensors [39] use a single MMF as both the sensor lead and the sensing element and, therefore, may suffer from instability caused by the fluctuations in the modal distribution in the MMF lead. The problem had been solved recently by using SMFs as the input and output leads of the sensor [48]. While the use of SMF leads reduces the output power of the sensor, it can provide higher sensitivity and better stability [48]. In this thesis, configurations and potential applications of this kind of microbend sensors will be investigated, because such microbend sensors, using SMF leads at both the input and output, offer many advantages over the conventional microbend sensors.

The mechanism of periodic microbending also shows that the micobending can change the modal power distribution in an MMF. Therefore, the reflection spectrum of an MMFBG can be tuned by providing microbending at the MMF input, and the combination of the microbending and MMFBG is possible to achieve tunable filters that allow the implementations of new photonic devices. Such applications are fully worth considering.

1.3 Objectives

The main objective of this thesis is to study both characteristics and applications of the periodic structure in GRIN MMF. The reason for choosing GRIN MMF is that such fibers are commercially available and have been widely adopted in optical communication systems. This approach, however, can be extended to any other kind of MMFs. The goals of this work include:

1) To study the spectral characteristics of the MMFBG. In particular, the uniform MMFBG, as any other special FBG designs can be derived from this basic form.
2) To verify the potential applications of MMFBG in sensing and telecommunication, where the study is focused on the spectrum-tuning ability of an MMFBG.
3) To investigate the mode-coupling mechanism in a MMF LPG. The LPG fabricated, using CO_2 laser irradiation, will be examined.
4) To study the sensing applications of CO_2 laser formed LPG in MMF.
5) To develop a microbend-induced mode coupling theory for the guided mode coupling in an MMF that has been subjected to microbending. It would be able to quantify the working principles of microbend based mode scramblers, the mode converters and microbend sensors.
6) To design new microbend MMF sensors with SMF leads at both the input and output.

1.4 Major contributions

A theoretical study on the mode coupling mechanism is presented for the LPG in GRIN MMF. The coupling among co-propagating core modes in a GRIN MMF is found to be wavelength-independent, and therefore does not produce distinct rejection or passing bands. Strong mode couplings take place in the LPG when the pitch of the grating is selected as the critical spatial period of the fiber. An analytical equation is obtained to predict the critical spatial period. The validity of theory is confirmed by experiments.

MMF LPGs fabricated with a CO_2 laser are proposed and demonstrated. The grating is formed by exposing a GRIN MMF to a CO_2-laser beam point by point along the fiber. The laser beam is intense enough to deform the fiber locally resulting in a periodic variation in the fiber diameter (i.e., a periodic taper). The effects of the pitch, the degree of deformation, and the number of periods on the transmission of the grating are measured and discussed. To demonstrate the potential of the grating as an effective physical or chemical sensor, the responses of the grating to axial strain and surrounding refractive index are presented.

A theory to describe the microbend-induced mode coupling in a GRIN MMF is developed. While existing theoretical studies focus on the transmission power loss of a microbent MMF, the theory here is mainly dealing with the microbend induce core mode coupling. By matching the incident and excited mode fields at the microbend,

the coupling coefficients among the guided modes at different microbending conditions are obtained. The theory suggests that the fundamental mode is selectively coupled to a high-order mode, whose order is determined by the degree of microbending. Near-field measurement results for a GRIN MMF subjected to microbending and the reflection spectra of an FBG in a GRIN MMF at different microbending conditions are presented to verify the theory. The usefulness of the theory is demonstrated with applications in predicting the performance of microbend sensors, quantifying the function of mode scramblers in the form of a periodic microbend, and explaining the operational principle of the microbend based mode converter.

Based on the microbending theory developed, a compact microbend sensor, operating in the reflection mode, for simultaneous measurement of a mechanical parameter and the temperature is proposed. The sensor is composed of a single-mode fiber lead, a multimode sensing fiber, and an SMF Bragg grating, where microbending is applied to the MMF for mechanical-parameter measurement and the grating provides an additional signal for temperature measurement. The sensor is demonstrated experimentally with two demodulation schemes based on a broadband source and a tunable laser respectively. The sensor extends the capacity of a conventional microbend sensor and offers many additional advantages, including higher stability, higher sensitivity, single-end access, and superior multiplexing capability.

The spectral characteristics of MMFBG are studied, including the phase matching of mode coupling, the locating of reflection wavelengths, the spacing of neighboring reflections, and the tuning of the spectrum. The application of MMFBG for implementing wavelength-switchable EDFLs is proposed. Two wavelength switching schemes are developed. The first scheme is realized by taking advantage of the combination of microbend-induced mode coupling theory developed and the properties of an MMFBG. The other is accomplished by varying the alignment position of an SMF against an MMFBG to achieve selective mode excitation and filtering. Stable single-wavelength lasing is accomplished over a wide wavelength range with various switchable discrete lasing lines.

1.5 Organization

This thesis is organized into 7 Chapters.

Chapter 1 is an introduction to the motivations, objectives, and major contributions of this work presented in the thesis.

Chapter 2 provides an overview of the periodic structures in GRIN MMF, including fundamental theories, basic concepts, and literature reviews.

Chapter 3 is about FBGs in GRIN MMF, where the grating properties and responses to strain and temperature are included.

Chapter 4 presents a study on the LPGs in GRIN MMF, addressing grating characterizations and potential sensing applications.

Chapter 5 mainly deals with the periodic microbend structure in MMF. Firstly, a theory is developed to study the core mode coupling in an MMF that is subjected to periodic microbending. Secondly, based on the theory, a sensor consisting of a microbended MMF and a SMFBG is proposed and demonstrated to enable the simultaneous measurements of a mechanical parameter and temperature.

Chapter 6 demonstrates the applications of MMFBG in erbium-doped fiber lasers. Two schemes to implement the MMFBG assisted wavelength switchable fiber lasers are presented.

Chapter 7 summarizes the current work and suggests the future direction of work in the area.

CHAPTER 2

FUNDAMENTAL THEORIES AND LITERATURE REVIEW

2.1 Overview

This chapter introduces the fundamental theories of the GRIN MMF and mode coupling analysis, covering basic properties of GRIN MMF, modal behavior, and coupled-mode theory. The grating formation, the recent interests for periodic structures in GRIN MMF, and their current applications are also reviewed.

2.2 Graded-index multimode fiber

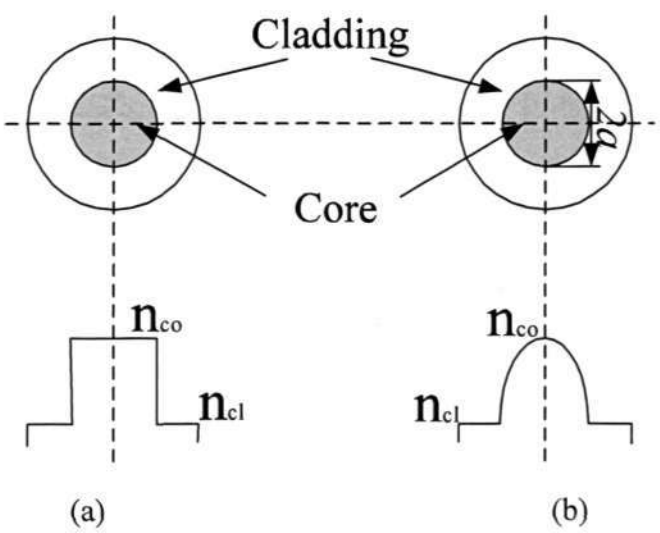

Fig. 2.1 Index profiles of (a) step-index fiber and (b) parabolic graded-index fiber

Generally optical fibers are classified into two categories, namely, SMFs and MMFs [49-52]. While SMFs usually have a step-index (SI) profile, among MMFs, two subcategories, SI MMFs and GRIN MMFs, are characterized depending on its core-refractive-index profile as shown in Fig. 2.1.

GRIN MMF was first studied in detail by Gloge in 1973 [53]. In Gloge's approach, WKB method was used to obtain the analytical solutions for a GRIN MMF. WKB analysis on GRIN MMF is an approximate approach, but it gives fairly accurate results.

In general, the core refractive index profile of a GRIN MMF is often written as [53]:

$$n(r) = \begin{cases} n_{co}\left[1-2\Delta(r/a)^{\alpha}\right]^{\frac{1}{2}} & \text{for} \quad 0 \le r \le a \\ n_{cl} = n_{co}\left[1-2\Delta\right]^{\frac{1}{2}} & \text{for} \quad r > a \end{cases}, \tag{2.1}$$

where $n(r)$ is the refractive index distribution along the fiber radius direction r from the axis of the core, n_{co} and n_{cl} are the refractive indices of the fiber core at its axis and cladding respectively, a is the core radius, α is the parameter describing the index profile, and Δ is a scale factor describing the scale of profile change and is given as

$$\Delta = (n_{co}^2 - n_{cl}^2)/2n_{co}^2 . \tag{2.2}$$

Obviously, unlike the SI MMF, GRIN MMF has varying core refractive index that is a function of the radial distance r from the axis of the fiber. The important

advantage of GRIN MMFs is the reduced intermodal dispersion (IMD) effect that always limits the transmission bit rate and distance. A good example is the parabolic index distribution ($\alpha = 2$) that was predicted to nearly equalize the group velocities of the propagating modes [54]. The reduced IMD in the parabolic GRIN MMF allows it to be used as high bit rate and long distance transmission medium. Therefore, such MMFs are commercially available and widely adopted in current optical data networks. In this thesis, all studies have been conducted on the periodic structures that have been fabricated in the MMF with a parabolic profile. The GRIN MMFs henceforth will be referred to as the parabolic profile MMFs. Most approaches and results in this thesis should be applicable to the applications of SI MMF.

2.3 Vector modes of parabolic-index multimode fiber

The modes in GRIN MMF can be classified into guided modes, leaky modes, and radiation modes [46]. The following discussions focus exclusively on the guided modes of a GRIN MMF.

From the Maxwell's equations (see Appendix A) [49], one may derive the wave equation

$$\left(\nabla^2 + k^2 n^2(\omega)\right)\begin{pmatrix}\vec{E}\\ \vec{H}\end{pmatrix} = 0\,. \tag{2.3}$$

Each mode is indeed a specific solution of Eq. (2.3). It satisfies the appropriate boundary conditions and has the property that its spatial distribution does not change with propagation.

An infinite cladded parabolic refractive-index profile is one of the few profiles where solutions of the scalar wave equation can be found in a closed analytical form. These solutions are also applicable to the vector wave equation where the weakly guiding condition is satisfied [55-57]. Using scalar wave equation solution $\psi^i_{\mu,v}(r)$ for radial variation, in the cylindrical coordinates, the transverse components of the electric and magnetic fields of the modes are given by [55-57]

$$\vec{E}^i_t(r,\phi,z) = (n_{co}Y_0)^{-1/2}(\mp i\hat{u}_r - \hat{u}_\phi)\cdot\psi^i_{\mu,v}(r)\cdot\exp[-i(v\phi+\beta^i_{\mu,v}z)], \tag{2.4}$$

$$\vec{H}^i_t(r,\phi,z) = n_{co}Y_0 \times \vec{E}^i_t. \tag{2.5}$$

The scalar modes for a GRIN MMF are given by

$$\psi^i_{\mu,v}(r) = \frac{1}{w_0}\left[\frac{4(\mu-1)!}{\pi e_v(\mu-1+v\mp1)!}\right]^{1/2}\left(\frac{\sqrt{2}r}{w_0}\right)^{v\mp1} L^{v\mp1}_{\mu-1}\left(\frac{2r^2}{w_0^2}\right)\exp\left(\frac{-r^2}{w_0^2}\right), \tag{2.6}$$

with an axial propagation constant

$$\beta^i_{\mu,v} = \{n^2_{co}k^2_0 - [v\mp1+2(\mu-1)+1]/w^2_0\}^{1/2}, \tag{2.7}$$

where w_0 is the spot size associated with the fundamental mode, which is given as

$$w^2_0 = 2a/[k_0 n_{co}(2\Delta)^{1/2}]. \tag{2.8}$$

In the above equations,

$$L_{\mu-1}^{v}(x)=\exp(x)\left(\frac{x^{-v}}{(\mu-1)!}\right)\left(\frac{d^{\mu-1}(\exp(-x)\cdot x^{\mu+v-1})}{dx^{\mu-1}}\right), \tag{2.9}$$

$$e_v=\begin{cases}1, & v=1\\ 2, & v\neq 1\end{cases} \quad \mu,v=1,2,3,\ldots, \tag{2.10}$$

$\hat{u}_r$ $\hat{u}_\phi$, and $\hat{u}_z$ are unit vectors in the r, ϕ, and z directions of the cylindrical coordinates, Y_0 is the intrinsic admittance of free space, k_0 is the wave number in free space, $d(\ )/d(\ )$ denotes the differential operation, and i = 1, 2 corresponds to the upper (-) and lower (+) signs in the above equations. The coefficient $(n_0Y_0)^{-1/2}$ is used to normalize the power in the μ,v mode to unity.

Transverse modes guided in an optical fiber can be classified into TE (Transverse Electric) modes, TM (Transverse Magnetic) modes, and Hybrid modes [52, 58]. TE modes have no electric field in the direction of propagation; TM modes have no magnetic field in the direction of propagation; and Hybrid modes are those which have both electric and magnetic field components in the direction of propagation. The Hybrid modes can be expressed as HE and EH or HG modes. In the set of HE modes, their axial magnetic field (H_z) makes a greater contribution than electric field (E_z). In the other set (EH modes), it is the axial electric field (E_z) that makes the greater contribution. In those cases where the symmetry of the optical resonator is restricted

by polarizing elements, transverse modes with rectangular symmetry are formed, which are given as HG modes.

Assuming that the E_r component is symmetrical about some axis in the fiber input plane through the fiber center, the imaginary part of the azimuthal variation is used to get the HE modes ($i = 1$):

$$E_r = +(n_{co}Y_0)^{-1/2}\psi^1_{\mu,v}(r)\cos(v\phi)\exp(-i\beta^1_{\mu,v}z), \tag{2.11a}$$

$$E_\phi = -(n_{co}Y_0)^{-1/2}\psi^1_{\mu,v}(r)\sin(v\phi)\exp(-i\beta^1_{\mu,v}z), \tag{2.11b}$$

$$H_r = -(n_{co}Y_0)^{+1/2}\psi^1_{\mu,v}(r)\sin(v\phi)\exp(-i\beta^1_{\mu,v}z), \tag{2.11c}$$

$$H_\phi = -(n_{co}Y_0)^{-1/2}\psi^1_{\mu,v}(r)\cos(v\phi)\exp(-i\beta^1_{\mu,v}z). \tag{2.11d}$$

For the EH modes ($i = 2$), a similar set of expressions is also obtained with an interchange of the signs of Eqs. (2.11a) and (2.11d). In the case where E_r components have an anti-symmetrical part, a similar set of field functions is obtained with $\cos(v\phi)$ replaced by $\sin(v\phi)$ and $\sin(v\phi)$ replaced by $\cos(v\phi)$.

In practice, maximum importance will be given to the linearly polarized modes. Specifically for x-polarized modes, the fields are

$$\vec{E}_{\mu,v}(r,\phi,z) = \hat{x}E_{(x)\mu,v}(r,\phi,z)$$

$$= (n_{co}Y_0w_0^2)^{-1/2}\psi^1_{\mu,v}(r)\cos(v\phi)\exp(-i\beta^1_{\mu,v}z), \tag{2.12}$$

$$\hat{H}_{\mu,v}(r,\phi,z) = \hat{y}n_{co}Y_0E_{(x)\mu,v}\ . \tag{2.13}$$

As the scalar modes mentioned above are expressed in terms of Gaussian-Laguerre functions, such modes are named as Gaussian-Laguerre modes (HE modes). Fig. 2.2 shows the general HE mode patterns [59]

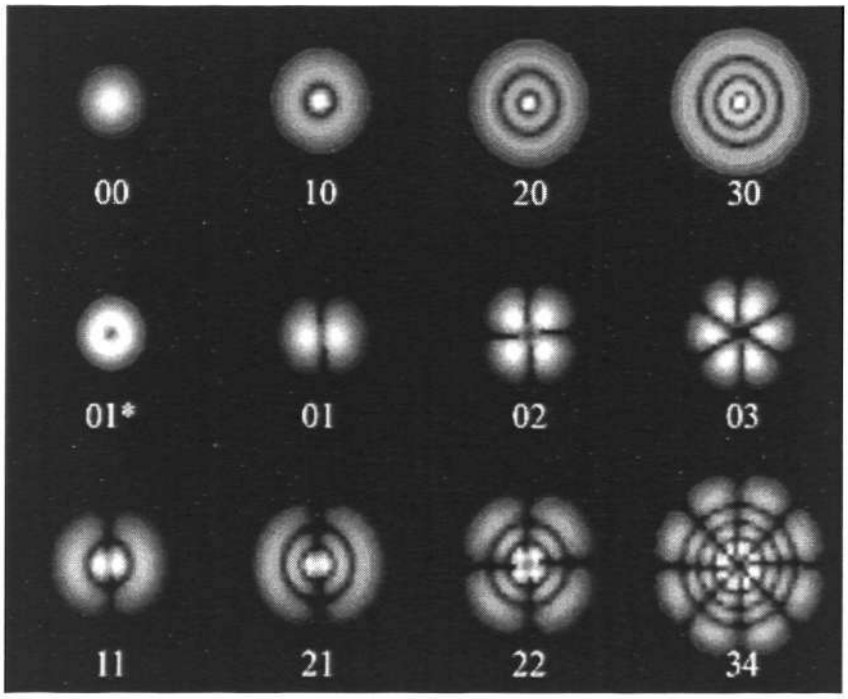

Fig. 2.2 General HE mode patterns [59]

In the Cartesian coordinates, usually the Gaussian-Hermite function are used to express the scalar modes, and therefore one may get the scalar modal fields of Gaussian-Hermite modes (HG modes) as follows [57, 60, 61]

$$\psi_{pq}(x,y,z) = [w_0{}^2 \pi 2^{(p+q-1)} p!q!]^{-1/2} H_p\left(\frac{\sqrt{2}x}{w_0}\right) H_q\left(\frac{\sqrt{2}y}{w_0}\right)$$

$$\cdot \exp[-(x^2+y^2)/w_0{}^2] \exp(-i\beta_{p,q} z), \qquad (2.14)$$

with a propagation constant

$$\begin{cases} \beta_{p,q} = \{n_{co}^2 k_0^2 - 2(2p+2q+2)/w_0^2\}^{1/2} \\ p,q = 0,1,2,... \end{cases}, \qquad (2.15)$$

where $H_n(x)$ denotes the n^{th} Hermite polynomial.

Fig. 2.3 shows the general patterns of HG modes [59]

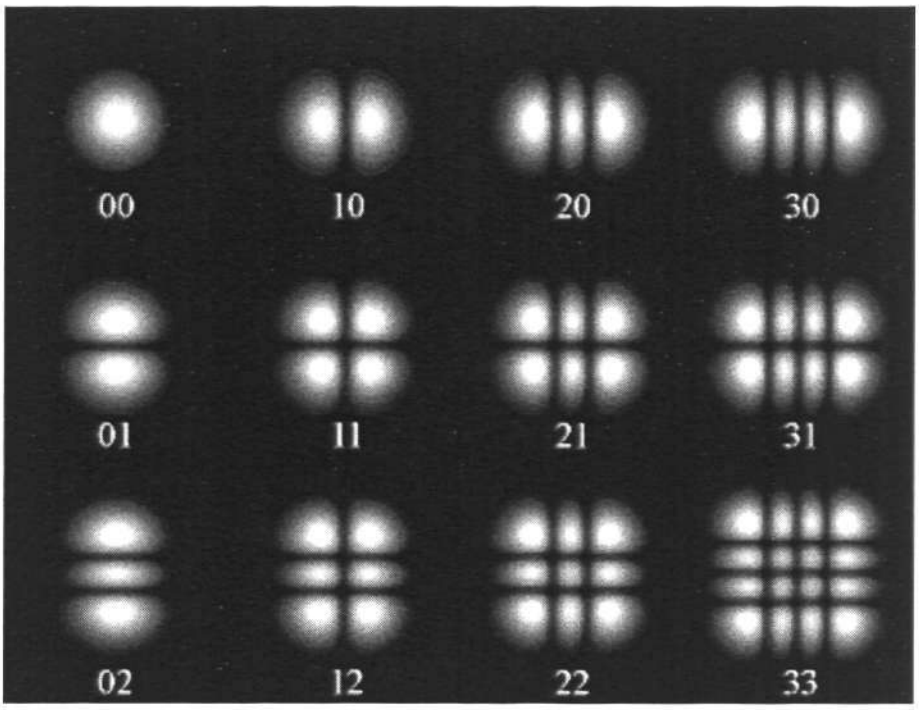

Fig. 2.3 General patterns of HG modes [59]

From the WKB analysis [53], the total number of modes N for a parabolic GRIN MMF is given as

$$N = \frac{1}{2} a^2 k_0{}^2 n_{co}^2 \Delta , \tag{2.16}$$

and k_0 is the propagation vector in free space, having the form

$$k_0 = \frac{2\pi}{\lambda} . \tag{2.1 7}$$

Each mode can be also specified by a pair of numbers (μ, v) for HE modes or (p, q) for HG modes, which are obtained by counting the number of radial and azimuthal

(x-axis and y-axis for HG modes) nodal surfaces in the field intensities of that mode, respectively. The important definition of the principal mode is obtained here. An approximate set of degeneracies exists among the propagation constants of the guided modes, and in such case, β depends only on a principal mode number m [42].

If the interest is restricted to mode groups that are sets of mode functions having the same axial propagation constant β, each Gaussian-Hermite mode function of a mode group m can be expressed as a linear combination of the Gaussian-Laguerre mode functions of the same group m (having the same propagation constant). This means that the power distribution among different mode groups is the same whether Gaussian-Hermite or Gaussian-Laguerre mode functions are used.

Therefore, for HE modes

$$m = 2\mu + v - 2, \tag{2.18}$$

and for HG modes

$$m = p + q + 1. \tag{2.19}$$

The m^{th} mode group of approximately degenerate modes consists of the $2(m+1)$ modes. The total number of principal mode groups M is found as

$$M = \sqrt{N} = \frac{\sqrt{2\Delta}}{2} akn_{co}. \tag{2.20}$$

Based on WKB anlysis, the spectrum of the propagation constant β_m of principal

mode group m can be approximated by

$$\beta_n = n_{co} k \{1 - 2\Delta[m/M]\}^{1/2}. \tag{2.21}$$

2.4 Review of coupled-mode theory

The theory of mode coupling in light waveguides had been studied extensively in the late 60s and early 70s [42, 46, 62, 63]. The coupled mode theory governing the mode coupling in optical waveguides, in particular GRIN MMFs, is reviewed here.

Assuming that the magnetic properties of the material are those of vacuum, the Maxwell's equations (Appendix A) for a dielectric medium with an arbitrary index distribution

$$n = n(x, y, z), \tag{2.22}$$

are

$$\nabla \times \vec{H} = i\omega\varepsilon_0 n^2 \vec{E}, \tag{2.23}$$

$$\nabla \times \vec{E} = -i\omega\mu_0 \vec{H}. \tag{2.24}$$

The operator ∇ and the fields can be decomposed into its transverse and longitudinal components:

$$\nabla = \nabla_t + \vec{e}_z \frac{\partial}{\partial z}, \tag{2.25}$$

$$\vec{E} = \vec{E}_t + \vec{E}_z, \tag{2.26}$$

$$\vec{H} = \vec{H}_t + \vec{H}_z. \tag{2.27}$$

Bearing in mind that

$$\vec{e}_z \times \frac{\partial \vec{E}_z}{\partial z} = 0, \tag{2.28}$$

$$\vec{e}_z \times \frac{\partial \vec{H}_z}{\partial z} = 0. \tag{2.29}$$

Therefore, the curl of the field vectors can now be expressed by its transverse and longitudinal parts:

$$(\nabla \times \vec{E})_t = \nabla_t \times \vec{E}_z + \vec{e}_z \times \frac{\partial \vec{E}_t}{\partial z}, \tag{2.30}$$

$$(\nabla \times \vec{E})_z = \nabla_t \times \vec{E}_t, \tag{2.31}$$

and

$$(\nabla \times \vec{H})_t = \nabla_t \times \vec{H}_z + \vec{e}_z \times \frac{\partial \vec{H}_t}{\partial z}, \tag{2.32}$$

$$(\nabla \times \vec{H})_z = \nabla_t \times \vec{H}_t. \tag{2.33}$$

Eqs. (2.31) and (2.33) can be applied into Eqs. (2.23) and (2.24) to obtain the z components of Maxwell's equations, which are written as

$$\vec{E}_z = (1/i\omega\varepsilon_0 n^2)\nabla_t \times \vec{H}_t, \tag{2.34}$$

$$\vec{H}_z = -(1/i\omega\mu_0)\nabla_t \times \vec{E}_t. \tag{2.35}$$

By using Eqs. (2.23), (2.24), (2.30) and (2.31) and replacing $\vec{E}_z$ and $\vec{H}_z$ with the help of Eqs. (2.34) and (2.35), the transverse parts of Maxwell's equations can be regrouped and expressed as

$$-\left(1/i\omega\mu_0\right)\nabla_t\times\vec{E}_t\left(\nabla_t\times\vec{E}_t\right)+\left(\vec{e}_z\times\frac{\partial\vec{H}_t}{\partial z}\right)=i\omega\varepsilon_0 n^2\vec{E}_t\,, \tag{2.36}$$

$$\left(1/i\omega\varepsilon_0\right)\nabla_t\times\left[\left(1/n^2\right)\nabla_t\times\vec{H}_t\right]+\left(\vec{e}_z\times\frac{\partial\vec{E}_t}{\partial z}\right)=-i\omega\mu_0\vec{H}_t\,. \tag{2.37}$$

As mentioned before, modes are characterized by their z dependence of

$$f(z)=e^{-i\beta z}\,. \tag{2.38}$$

The ideal waveguide is defined by a refractive index distribution that is independent of z

$$n_0=n_0(x,y)\,. \tag{2.39}$$

The modes must also satisfy Maxwell's equations with n replaced by n_0. Therefore, from Eqs. (2.36) and (2.37), the following equations are obtained for the transverse electric and magnetic field vectors of the ideal normal modes:

$$-\left(1/i\omega\mu_0\right)\nabla_t\times\left(\nabla_t\times\bar{\bar{E}}_{\rho t}\right)-i\beta_\rho\left(\vec{e}_z\times\bar{\bar{H}}_{\rho t}\right)=i\omega\varepsilon_0 n_0^2\bar{\bar{E}}_{\rho t}\,, \tag{2.40}$$

and

$$\left(1/i\omega\varepsilon_0\right)\nabla_t\times\left[\left(1/n_0^2\right)\nabla_t\times\bar{\bar{H}}_{\rho t}\right]-i\beta_\rho\left(\vec{e}_z\times\bar{\bar{E}}_{\rho t}\right)=-i\omega\mu_0\bar{\bar{H}}_{\rho t}\,, \tag{2.41}$$

where subscript ρ is a shorthand notation for the total number of subscripts used to label all the modes, which include guided modes and radiation modes, and $\tilde{\bar{E}}_{\rho t}$ or $\tilde{\bar{H}}_{\rho t}$ are the transverse electric or magnetic field vectors for mode ρ.

By considering that the guided and radiation modes of an ideal waveguide form a complete orthogonal set, the solutions to Eqs. (2.36) and (2.37) in terms of mode field solutions of Eqs. (2.40) and (2.41) can be expanded as follows:

$$\vec{E}_t = \sum_{\rho} a_\rho \tilde{\bar{E}}_{\rho t}, \tag{2.42}$$

$$\vec{H}_t = \sum_{\rho} b_\rho \tilde{\bar{H}}_{\rho t}, \tag{2.43}$$

where a_ρ and b_ρ are the amplitude coefficients. It should be noted that the summation symbol indicates both the sum over guided modes that are discrete and the sum and integral over radiation modes that have a combination of discrete and continuous propagation constants spectrum. The factor ($e^{-i\beta z}$) is not included in mode field expressions $\tilde{\bar{E}}_{\rho t}$ and $\tilde{\bar{H}}_{\rho t}$. Also worth mentioning is the fact that the same amplitude coefficient is used for both the x and y components of the field vector expansion. This is justified by the fact that each mode must behave as an entity, and all field components of each mode must change at the same rate. Indeed, the amplitude coefficients for the electric and magnetic fields of the same mode are the same. By substituting the field expansions Eqs.(2.42) and (2.43) into the Maxwell's Eqs. (2.36) and (2.37) and using the mode Eqs. (2.40) and (2.41), it yields

$$\sum_{\rho}\left[\left(db_\rho / dz + i\beta_\rho a_\rho\right)\left(\vec{e}_z \times \tilde{\bar{H}}_{\rho t}\right) - i\omega_0\varepsilon_0(n^2 - n_0^2)a_\rho \tilde{\bar{E}}_{\rho t}\right] = 0, \tag{2.44}$$

$$\sum_{\rho}\left\{\left(da_{\rho}/dz+i\beta_{\rho}b_{\rho}\right)\left(\vec{e}_{z}\times\tilde{\vec{E}}_{\rho t}\right)+\left(1/i\omega_{0}\varepsilon_{0}\right)b_{\rho}\nabla_{t}\times\left[\left(n^{-2}-n_{0}^{-2}\right)\left(\nabla_{t}\times\tilde{\vec{H}}_{\rho t}\right)\right]\right\}=0 \quad (2.45)$$

The scalar product of Eq. (2.44) with $\tilde{\vec{E}}_{\rho t}$ and Eq. (2.45) with $\tilde{\vec{H}}_{\rho t}$ can be obtained, by using the orthogonality relation

$$\int_{-\infty}^{\infty}\int_{-\infty}^{\infty}\vec{e}_{z}\cdot\left(\tilde{\vec{E}}_{\rho t}\times\tilde{\vec{H}}_{\sigma t}\right)dxdy=2s_{\sigma}\beta_{\sigma}^{*}P\delta_{\rho\sigma}/\left|\beta_{\rho}\right|. \quad (2.46)$$

It is important to note that the longitudinal parts of the vectors do not contribute to the left-hand side of the above expression. The symbol $\delta_{\rho\sigma}$ indicates Kronecker's delta expression for discrete indices ρ and σ. It stands for Dirac's delta function if both ρ and σ are labels of continuum modes and is zero if one of the labels indicates a guided mode while the other indicates a mode of the continuum. P is a real and positive quantity. The factor s_{ρ} is always 1 for guided modes and radiation modes with real propagation constants. But for evanescent continuum modes with imaginary value of propagation constants, in order to keep P positive, s_{ρ} = 1 is required. After integration over the infinite cross section, with the help of Eq. (2.46), it yields

$$\left(db_{\sigma}/dz\right)+i\beta_{\sigma}a_{\sigma}=2\sum_{\rho}\bar{K}_{\sigma\rho}a_{\rho}, \quad (2.47)$$

$$\left(da_{\sigma}dz\right)+i\beta_{\sigma}b_{\sigma}=2\sum_{\rho}\bar{k}_{\sigma\rho}b_{\rho}, \quad (2.48)$$

where

$$\bar{K}_{\sigma\rho}=\frac{\omega\varepsilon_{0}}{4is_{\sigma}P}\frac{\left|\beta_{\sigma}\right|}{\beta_{\sigma}}\int_{-\infty}^{\infty}\int_{-\infty}^{\infty}\left(n^{2}-n_{0}^{2}\right)\tilde{\vec{E}}_{\sigma t}^{*}\cdot\tilde{\vec{E}}_{\rho t}dxdy, \quad (2.49)$$

$$\bar{k}_{\sigma\rho}=\frac{-1}{4s_{\sigma}i\omega\varepsilon_{0}P}\frac{\left|\beta_{\sigma}\right|}{\beta_{\sigma}^{*}}\int_{-\infty}^{\infty}\int_{-\infty}^{\infty}\tilde{\vec{H}}_{\sigma t}^{*}\cdot\nabla_{t}\times\left[\left(n^{-2}-n_{0}^{-2}\right)\nabla_{t}\times\tilde{\vec{H}}_{\rho t}\right]dxdy. \quad (2.50)$$

By substituting Eq. (2.34) into Eq. (2.50), we get the transformation

$$\bar{k}_{\sigma\rho} = \frac{\omega\varepsilon_0}{4 s_\sigma i P} \frac{|\beta_\sigma|}{\beta_\sigma^*} \int_{-\infty}^{\infty} \int_{-\infty}^{\infty} \frac{n_0^2}{n^2} \left(n^2 - n_0^2\right) \bar{\bar{E}}_{\sigma z}^* \cdot \bar{\bar{E}}_{\rho z} dx dy \,. \tag{2.51}$$

Because in terms of z dependence, the wave travels either in positive or in negative z direction, one can introduce the transformation

$$a_\sigma = a_\sigma^{(+)} + a_\sigma^{(-)}, \tag{2.52}$$

and

$$b_\sigma = a_\sigma^{(+)} - a_\sigma^{(-)}, \tag{2.53}$$

where

$$a_\sigma^{(+)} = c_\sigma^{(+)} \exp(-i\beta_\sigma z) \tag{2.54}$$

represents a wave traveling in positive z direction, and

$$a_\sigma^{(-)} = c_\sigma^{(-)} \exp(i\beta_\sigma z) \tag{2.55}$$

is a wave traveling in negative z direction. Substitution of Eqs. (2.52) and (2.53) into Eqs. (2.47) and (2.48) results in

$$\left(da_\sigma^{(+)}/dz\right) + i\beta_\sigma a_\sigma^{(+)} - \left[\left(da_\sigma^{(-)}/dz\right) - i\beta_\sigma a_\sigma^{(-)}\right] = 2\sum_\rho \bar{K}_{\sigma\rho}\left(a_\rho^{(+)} + a_\rho^{(-)}\right), \tag{2.56}$$

$$\left(da_\sigma^{(+)}/dz\right) + i\beta_\sigma a_\sigma^{(+)} - \left[\left(da_\sigma^{(-)}/dz\right) - i\beta_\sigma a_\sigma^{(-)}\right] = 2\sum_\rho \bar{k}_{\sigma\rho}\left(a_\rho^{(+)} - a_\rho^{(-)}\right). \tag{2.57}$$

Addition and subtraction of these two equations finally yields the following system of coupled wave equations:

$$da_\sigma^{(+)}/dz = -i\beta_\sigma a_\sigma^{(+)} + \sum_\rho \left(\bar{K}_{\sigma\rho}^{(+,+)} a_\rho^{(+)} + \bar{K}_{\sigma\rho}^{(+,-)} a_\rho^{(-)}\right), \tag{2.58}$$

$$da_\sigma^{(-)}/dz = i\beta_\sigma a_\sigma^{(-)} + \sum_\rho \left(\bar{K}_{\sigma\rho}^{(-,+)} a_\rho^{(+)} + \bar{K}_{\sigma\rho}^{(-,-)} a_\rho^{(-)}\right), \tag{2.59}$$

with the coupling coefficients

$$K_{\sigma\rho}^{(p,q)} = p\bar{K}_{\sigma\rho} + q\bar{k}_{\sigma\rho}$$

$$= \frac{\omega\varepsilon_0}{4is_\sigma P}\int_{-\infty}^{\infty}\int_{-\infty}^{\infty}\left(n^2 - n_0^2\right)\left[\frac{|\beta_\sigma|}{\beta_\sigma^{(p)}}\bar{\bar{E}}_{\sigma t}^{(p)*}\cdot\bar{\bar{E}}_{\rho t}^{(q)} + \frac{n_0^2}{n^2}\frac{|\beta_\sigma|}{\beta_\sigma^{(p)*}}\bar{\bar{E}}_{\sigma z}^{(p)*}\cdot\bar{\bar{E}}_{\sigma z}^{(q)}\right]dxdy\,, \quad (2.60)$$

p and q are (+) or (-) if they appear as superscripts or +1 and -1 as factors. In Eq. (2.60), the following definitions are used

$$\beta_\sigma^{(+)} = \beta_\sigma\,, \quad (2.61)$$

$$\beta_\sigma^{(-)} = -\beta_\sigma\,, \quad (2.62)$$

$$\bar{\bar{E}}_{\sigma t}^{(-)} = \bar{\bar{E}}_{\sigma t}^{(+)} = \bar{\bar{E}}_{\sigma t}\,, \quad (2.63)$$

$$\bar{\bar{E}}_{\sigma z}^{(-)} = -\bar{\bar{E}}_{\sigma z}^{(+)} = -\bar{\bar{E}}_{\sigma z}\,. \quad (2.64)$$

Usually, for perturbation solutions of the coupled wave equations, it is more convenient to introduce slowly varying mode amplitudes. In the absence of coupling, the amplitude coefficients $c_\sigma^{(+)}$ and $c_\sigma^{(-)}$ in Eqs. (2.54) and (2.55) are actually constants. Therefore, the final form of coupled wave equations is

$$dc_\sigma^{(+)}/dz = \sum_\rho\left\{K_{\sigma\rho}^{(+,+)}c_\rho^{(+)}\exp\left[i\left(\beta_\sigma - \beta_\rho\right)z\right] + K_{\sigma\rho}^{(+,-)}c_\rho^{(-)}\exp\left[i\left(\beta_\sigma + \beta_\rho\right)z\right]\right\}, \quad (2.65)$$

$$dc_\sigma^{(-)}/dz = \sum_\rho\left\{K_{\sigma\rho}^{(-,+)}c_\rho^{(+)}\exp\left[i\left(\beta_\sigma + \beta_\rho\right)z\right] + K_{\sigma\rho}^{(-,-)}c_\rho^{(-)}\exp\left[-i\left(\beta_\sigma - \beta_\rho\right)z\right]\right\}. \quad (2.66)$$

2.5 Phase matching of mode coupling

Based on the coupled-mode theory reviewed in Section 2.4, the generalized concept of phase matching of mode coupling for periodic structures in GRIN MMF are to be determined in this section.

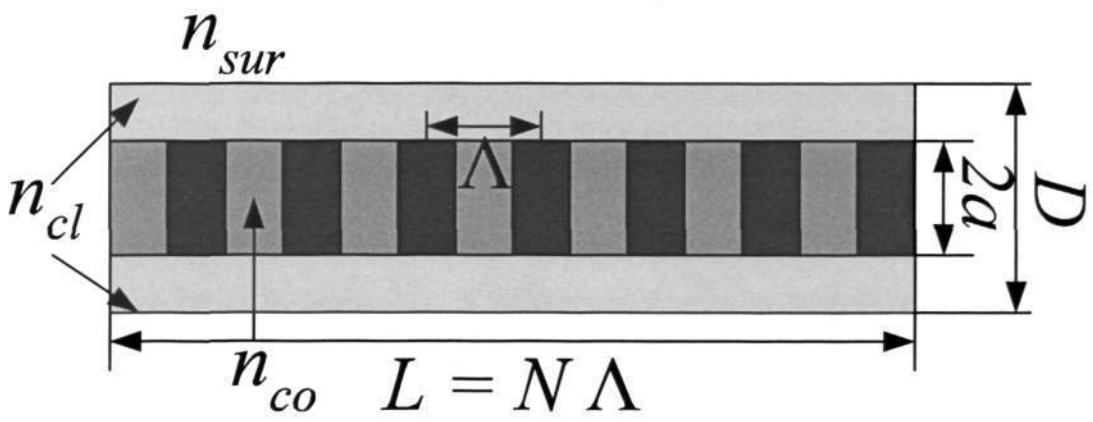

Fig. 2.4 Model for a periodic structure in a GRIN MMF

Fig. 2.4 shows a model of an arbitrary periodic structure in a GRIN MMF, where Λ is the period, L denotes the length of perturbation, N defines the total number of periods, D is the diameter of the fiber (excluding jacket), and n_{sur} is the surrounding refractive index. The periodic structure is assumed to be formed by either index modulation or geometric perturbation, appearing as the alternation of different color sections in the fiber core in Fig. 2.4.

Two assumptions are made in the model. Firstly, the departure of the waveguide from perfect geometry is either slight or at least low, so that the change of the slowly varying field amplitudes, which is caused by the perturbations, is very slow compared to the wavelength or the correlation length. Secondly, the coefficient $c_j^{(+)}$ of the incident mode is large compared to all other amplitudes, which yields

$$\left|c_j^{(+)}\right| >> \left|c_\rho^{(\pm)}\right| \tag{2.67}$$

with $\rho \neq j$.

The second assumption allows one to neglect all amplitude coefficients on the right-hand side of Eqs. (2.65) and (2.66). The first assumption allows one to treat $c_j^{(+)}$ as approximately constant over a relatively short distance. By integrating Eqs. (2.65) and (2.66), the approximate solutions are obtained

$$c_\sigma^{(+)}(z) = c_j^{(+)}(0) \int_0^z K_{\sigma j}^{(+,+)}(u) \exp\left[i\left(\beta_\sigma - \beta_j\right)u \right] du, \tag{2.68}$$

and

$$c_\sigma^{(-)}(z) = c_j^{(+)}(L) \int_L^z K_{\sigma j}^{(-,+)}(u) \exp\left[-i\left(\beta_\sigma + \beta_j\right)u \right] du, \tag{2.69}$$

with the initial conditions

$$c_\sigma^{(+)} = 0, \quad (z = 0) \quad \sigma \neq j, \tag{2.70}$$

and

$$c_\sigma^{(-)} = 0, \quad (z = l). \tag{2.71}$$

A general feature of the coupling coefficient (2.60) is that it can always be expressed as [62]

$$K_{\sigma\rho}^{(p,q)}(z) = \hat{K}_{\sigma\rho} \cdot f(z), \tag{2.72}$$

with constant $\hat{K}_{\sigma\rho}$ determined by the mode field vectors and the parameters of the waveguide including geometrical parameters and the refractive indices. The function $f(z)$ describes the actual z dependence of the index perturbation or a deformed circular fiber core boundary. Therefore, Eqs (2.68) and (2.69) can be written in the form

$$c_\sigma^{(+)}(0) = \sqrt{L} c_j^{(+)}(0) F\left(\beta_j - \beta_\sigma\right) \hat{K}_{\sigma j}, \tag{2.73}$$

and

$$c_\sigma^{(+)}(0) = -\sqrt{L} c_j^{(+)}(0) F\left(\beta_j + \beta_\sigma\right) \hat{K}_{\sigma j}, \tag{2.74}$$

where the Fourier transform of the deformation function $f(z)$ can be given as

$$F\left(\beta_j-\beta_\sigma\right)=\sqrt{L}^{-1}\int_0^L f(z)\exp\left[-i(\beta_j-\beta_\sigma)z\right]dz\,. \tag{2.75}$$

This form of the perturbation solution brings out an important point. The mode amplitudes, $c_\sigma^{(\pm)}$, are proportional to the Fourier transform of the deformation function $f(z)$ taken at the difference in the propagation constants of the incident and the excited modes.

Note that, although this result is derived with the weak perturbation assumption, the guided mode coupling in a GRIN MMF dose not rely on the assumption that the amplitude of the incident wave remains unchanged [64]. A very important conclusion can be drawn from Eqs. (2.73) to (2.75): for a GRIN MMF's distortion of length L, two modes p and q are strongly coupled when $F(\Delta\beta_{pq})$ is maximized.

The condition at which two modes p and q are most strongly coupled is the phase matching of mode coupling between these two modes. Considering $f(z)$ is periodically deformed with the period Λ, based on Eqs. (2.73) to (2.75) we obtain the phase matching conditions for co-propagation modes as

$$\beta_p^{(+)}-\beta_q^{(+)}=\beta_p-\beta_q=\frac{2\pi}{\Lambda}, \tag{2.76}$$

and counter-propagation modes as

$$\beta_p^{(+)}-\beta_q^{(-)}=\beta_p+\beta_q=\frac{2\pi}{\Lambda}. \tag{2.77}$$

2.6 Formation of periodic structures in GRIN MMF

The periodic structure in a GRIN MMF can be formed by either of index modulation or the geometrical deformation, both of which are capable of realizing the phase matching of mode coupling. The state-of-art techniques to form the periodic structures in fibers include ultraviolet (UV) irradiation, CO_2 laser irradiation, and microbending. Based on the photosensitivity of the optical fiber, sufficient UV irradiation is able to induce permanent index change in the fiber to form a periodic index modulation. The UV methods are capable of forming the FBG and LPG in fibers. It has been recently proposed to use a CO_2 laser for fabricating LPGs, where the grating structure is formed by either index changes or geometrical deformations. Periodic microbending is achieved with the microbend deformer that can be tuned to different mode coupling states. In this section, the fabrication techniques for periodic structures in the fiber are reviewed.

2.6.1 Photosensitivity and photo-induced grating

The initial observation of photosensitivity in germanium doped fibers was made in 1978 by Hills *et. al* [65], showing a refractive-index change in the core was induced to produce a permanent grating. Photosensitivity refers to a permanent change in refractive index or opacity induced by exposure to light radiation with the internal field playing an insignificant role [66].

There are two basic methods for creating the photo-induced gratings in optical fibers. One is the internal writing of the grating, which is a holographic process using launched coherent bound modes that couple and modify the refractive index of the waveguide core. Proposed by Lam and Garside in 1981, the first grating was produced by launching the 488 nm wavelength of an argon-ion laser into the fiber [67]. The second method is the external writing technique that uses a transverse exposure of an interference pattern formed from two UV light beams on the side of the fiber [31]. The external technique that has been widely used today is flexible enough so that one can choose the resonant reflection wavelength.

The external holographic setup adopted in [31] is shown in Fig. 2.5. The ultra-violet (UV) laser beam is split into two paths and then reflected using two mirrors where the angle between the two converging beams can be controlled.

Great care must be taken in this experiment setup, which is true for many kind of interferometric setup, because of the short coherence length of many UV sources. For example, excimer lasers, the most widely used source for writing the fiber gratings, typically have a coherence length of the order of 1 mm. Therefore, the beam path difference has to be carefully adjusted. In addition, the interference pattern can be affected by the airflow and mechanical vibrations in the environments. Thus the fringe pattern may change over time.

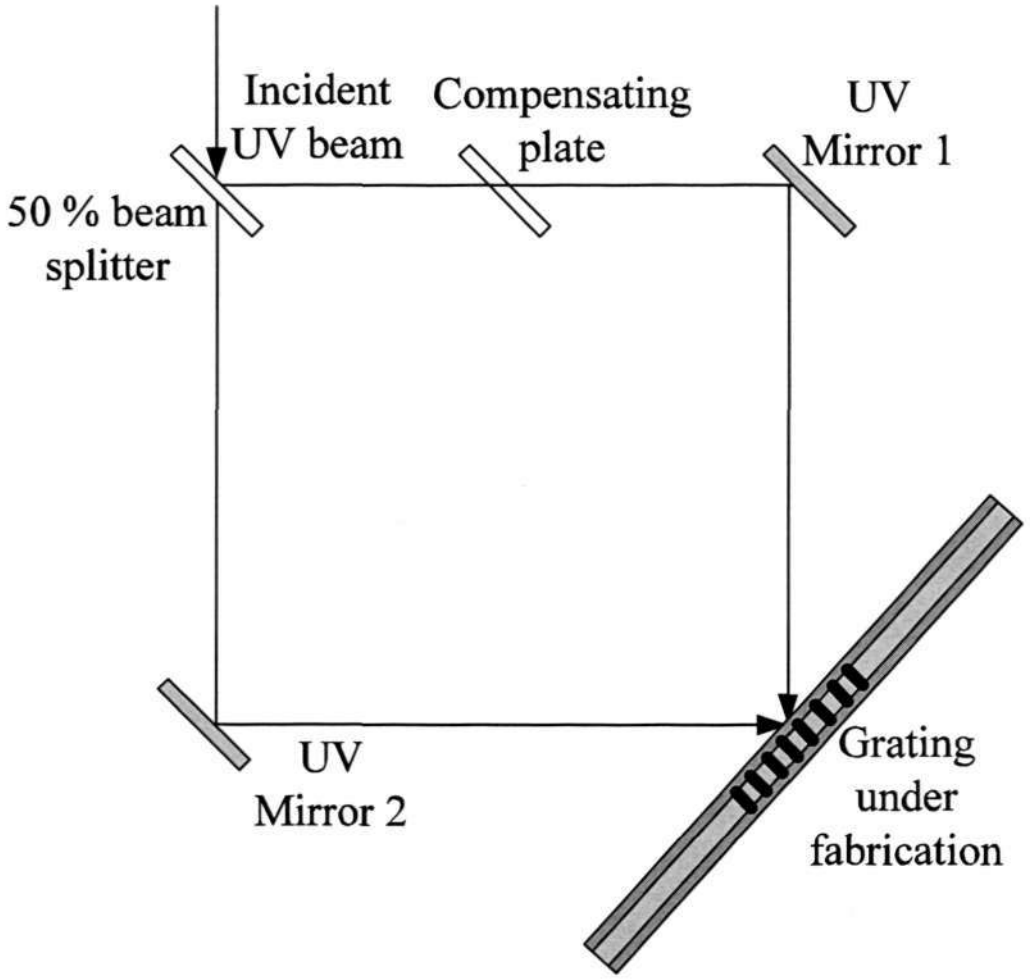

Fig. 2.5 Meltz's holographic fiber grating fabrication setup

Sacrificing the flexibility of the wavelength selection, the external phase mask technique, relaxes these stringent setup requirements, which exposes a spatially modulated phase mask at normal incidence with a KrF excimer laser at 249 nm. The diffracted light from the mask, forms a pattern that photoimprints a modulated refractive index into the core of a photosensitive fiber that is parallel to the mask [68].

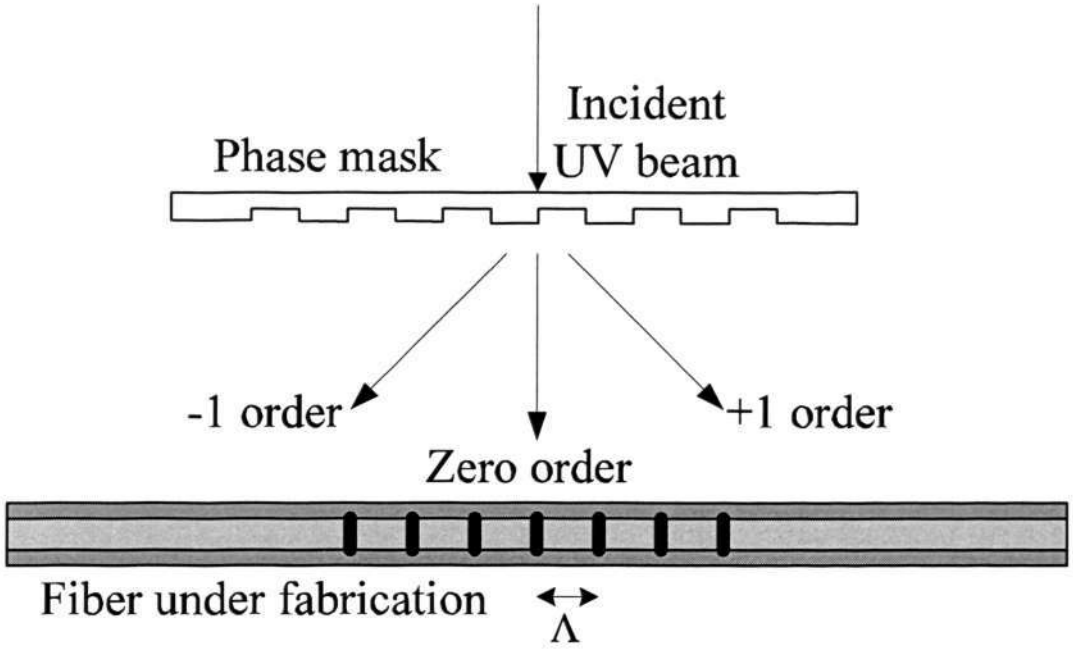

Fig. 2.6 Schematic diagram of the phase mask method

Fig. 2.6 shows the external phase mask technique for photo-imprinting the Bragg grating. The profile of the phase mask is chosen to produce a near-field fringe pattern that suppresses the zero order diffracted beam (< 3 %) and maximizes the diffracted plus and minus first-order beams [66].

Besides, standard optical fiber for FBG fabrication has to be hydrogen loaded prior to UV irradiation, and also to be thermal annealed post to UV irradiation. Usually the core of the standard optical fiber is doped with germanium in order to raise the index above that of pure silica in the cladding region. The germanium also creates a quantity of GeO (germanium monoxide) which creates oxygen deficient centers when exposed to UV radiation. These defects cause a rise in the refractive index. In general, this process is slow and depends on the intensity of the UV source.

By loading the optical fiber with hydrogen, the process can be speeded up by inducing a second photosensitive effect. The introduction of hydrogen into the core allows the UV radiation to create Si-OH which increases the refractive index of the core. These two effects together ensure the periodic variation of the refractive index in the core region. The reason that annealing is necessary is that due to the influx of hydrogen, the average refractive index of the Bragg grating is slightly elevated. The residual hydrogen in the fiber will leak out eventually, and therefore the refractive index will decrease causing a shift in the Bragg wavelength. To prevent this from happening during testing, the gratings require thermal annealing after fabrication. Usually, the annealing process is capable of stabilizing the Bragg wavelength for many years.

The UV method based on photosensitivity can be used for the fabrications of both short-period gratings (FBGs) and LPGs.

2.6.2 CO_2 laser method

Davis *et. al.* in 1998 first proposed the use of CO_2 laser (10.64 μm) to form LPG in optical fiber [37]. Their approach used the concept that refractive index changes can be introduced by simple thermal treatment. The CO_2 laser system to fabricate long-period gratings using thermal exposure is shown in Fig. 2.7, where the beam from a low power CO_2 laser was focused on a plane containing an optical fiber.

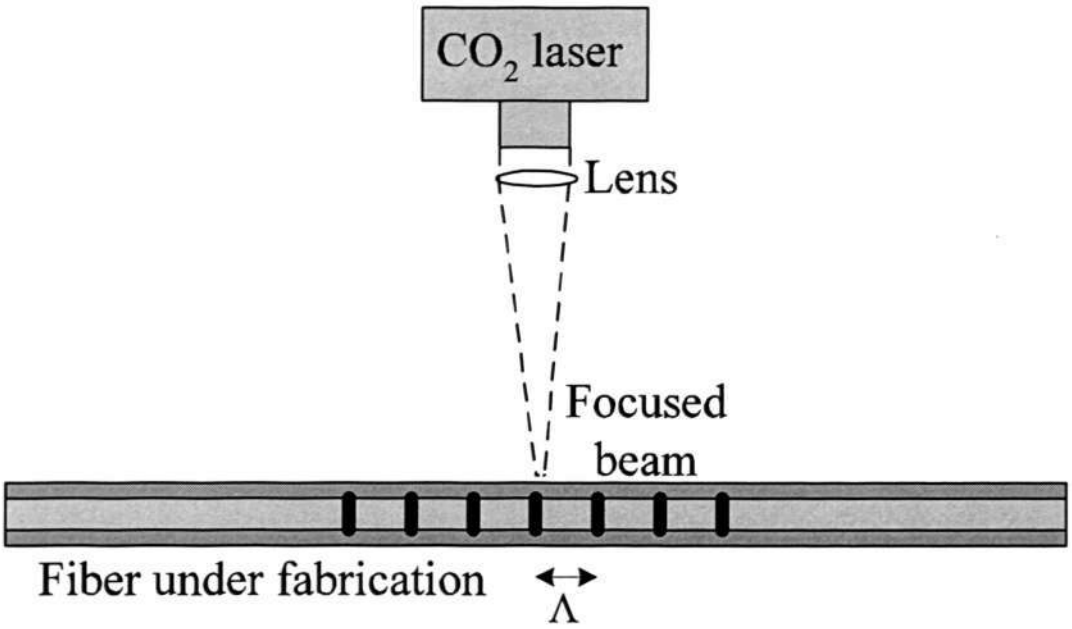

Fig. 2.7 CO_2 laser based grating fabrication system

The CO_2 output simply serves to increase the temperature of the fiber and hence index changes are produced due to residual stress relaxation in the core of the optical fiber [37, 69]. The mechanical stress can be fully relaxed by CO_2 laser irradiation and the remaining stress in the core is the thermal stress that is due to a mismatch of the thermal expansion coefficients of the fiber core and cladding [69].

The above mentioned residual stress relaxation induced refractive index change is achieved when the CO_2 laser operates at a low power level. By heating the fiber with higher power and longer duration using the CO_2 laser irradiation, the focused beam, however, will lead to the taper structure in the fiber. Kakarantzas *et. al* reported the LPG formed with periodic tapering structures using CO_2 laser method [70]. For the

grating consisting of periodic tapers, the mode coupling along the grating region is mainly caused by the geometrical deformation rather than index modulation.

Although CO_2 laser grating fabrication systems in the current stage is only suitable for gratings with longer periods, the use of cheap CO_2 lasers without resorting to UV-based lasers and amplitude masks is expected to drastically reduce the cost of manufacturing gratings. The process can also be used to manufacture a number of gratings on many fibers simultaneously by scanning the focused CO_2 laser beam across the fibers.

2.6.3 Periodic microbending

Unlike refractive index modulations or geometrical changes induced by UV or CO_2 laser irradiations in the optical fiber, periodic microbending formed in the optical fiber is designed with tunable mode coupling efficiency. Microbending, in the simplest term, is the mechanical perturbation of a multimode fiber waveguide and causes a redistribution of light power among the many modes in the fiber. The periodic microbending can be formed by a number of microbends.

The most widely used method to enhance periodic microbending effect is to squeeze the fiber between a set of corrugated plates called deformer plates or tooth blocks [71]. The configuration is shown in Fig. 2.8. The varying of applied force leads

to the separation between the tooth blocks changes, and therefore the sinusoidal amplitude of the clamped fiber changes accordingly. This allows the flexible tuning of the coupling coefficient.

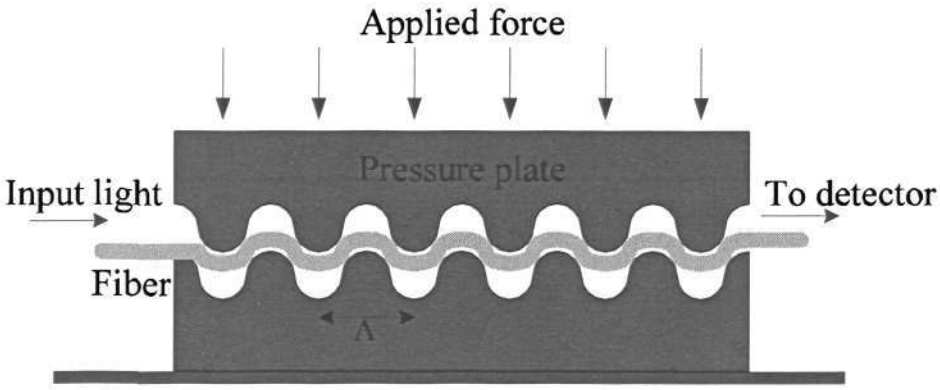

Fig. 2.8 Periodic microbending of the optical fiber achieved with deformer plates

In 1987, Oscroft described a microbend structure that is illustrated in Fig. 2.9 [72]. The periodic microbending is realized by a spiral deformer such as a stiff spring, where the period of the spiral is Λ. Such spiral deformer based periodic microbend was the first microbend deformer used commercially [40].

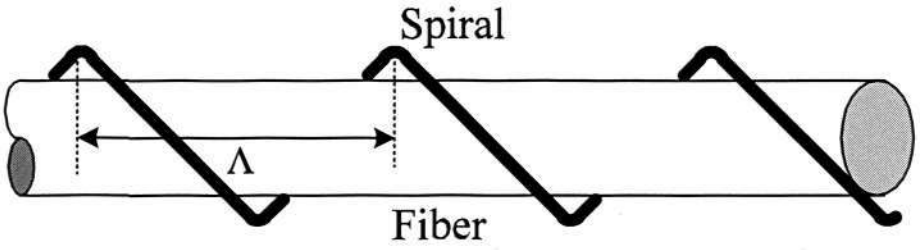

Fig. 2.9 Diagram of the periodic microbending achieved with spiral deformer

Electric arcs have also been proposed to produce periodic microbends. Such techniques have been reported in the fabrications of LPGs by Hwang *et. al.* in 1999 [3]. According to their report, the fabrication method is very simple and can be applied to any type of optical fiber including conventional SMFs. The principle of the electric arc technique is that when a local section of the fiber is heated by application of an electric arc, the fiber is slightly deformed owing to the lateral stress, creating a microbend. The amplitude of the microbend can be controlled by the duration of the arc and is typically less than 1 μm. The successive microbends in the optical fiber can be created without the requirement of the microbend deformer, i. e. by translating the electrodes according to the grating period and applying electric arcs. The periodic microbends generated by electric arcs, however, are permanent, which are different from those produced with the techniques using either tooth blocks or a spiral deformer.

The techniques to form periodic structures in the optical fiber, including periodic microbending, UV and CO_2 laser irradiation methods, have been reviewed (see, a comparison among these three techniques in Table 2.1). These techniques are those employed in this thesis. Other techniques for forming period structures in optical fibers should also include the femtosecond laser inscription [73-75], the high-energy ion implantation [35, 76], HF etching [77, 78]. Besides optical fibers, plastic optical fiber (POF) has found applications in optical sensing. But its application is limited due to the material properties [79].

Table 2.1: A comparison among major periodic structure formation techniques

	UV Technique	CO_2 Laser Method	Periodic Microbend
Fabrication	Using high power ultra-violet laser irradiation	Using high power CO_2 laser irradiation	Using deformers to Generate periodic microbending
Mechanism	Based on photosensitivity to induce periodic index modulation	Based on thermal effects, to induce either index change or geometrical deformation	Based on geometrical deformation
Applications	Capable of fabricating FBG and LPG	Only for LPG	Capable of fabricating LPG and periodic microbending with tunable coupling efficiency
Complexity	High	Medium	Low
Cost Effectiveness	Normal	Good	Good

2.7 Review of periodic structures in GRIN MMF

We have introduced fundamental theories and basic fabrication techniques for periodic structures in GRIN MMF. In this section, the development and current applications of the periodic structures in MMFs (namely, MMFBGs, MMF LPGs, and MMF with periodic microbending) are reviewed.

2.7.1 Multimode fiber Bragg grating

The FBG (also known as short period grating) in the SMF, induced by UV laser irradiation, has been extensively investigated since its first demonstration in 1980s

[31], and its applications have been widely recognized in various fields of optical communications and optoelectronics devices, including spectral filtering, dispersion compensation, wavelength tuning, and optical fiber sensing [1].

FBG in the MMF, in fact, has been reported in the paper where the holographic UV induced single-mode FBG was first presented [31]. The spectrum associated with the Bragg grating in an MMF shows multiple reflection peaks or transmission dips. In the early stages, no detailed analyses had been carried out for multimode fiber Bragg grating (MMFBG). The reason is that such MMFBGs do not produce a single wavelength reflection with the high reflectivity, and it can not be used as reflectors or filters in the optical communication systems consisting of SMF. Later in 1994, Wanser *et. al.* simulated the spectrum of an MMFBG and proposed its application as a bending sensor [80]. In 2000, a more detailed work on the MMFBG was reported by T. Mizunami *et. al.* [32]. They reported in detail the spectral characteristics of an FBG written in a GRIN MMF, including the temperature and polarization characteristics, where a theory of reflection of Bragg gratings in MMF was presented, and the mechanism of Bragg reflection was discussed. Their work further confirmed the multiple reflection peaks or transmission dips in an MMFBG spectrum, showing that the mechanism of the multiple reflections arises due to the grating reflections to different fiber modes.

MMFBG has already found applications in optical communications. The present

problem remaining in the single-mode FBG based laser system is the low coupling efficiency between the SMF and the laser diode. Obviously the MMFBG is advantageous in coupling with the laser diode owing to large core size of the MMF. In the FBG-tuned diode lasers, MMFBG were used to replace the single-mode FBG [81, 82]. The applications of the MMFBG in the vertical-cavity surface-emitting lasers (VCSEL) and external-cavity semiconductor lasers (ECSL) have been demonstrated experimentally [81, 82].

The use of MMFBG as optical sensors was first proposed by Wanser *et. al.* [80], where a distributed sensor network to measure the fiber bend was demonstrated. MMFBG was also described in measuring strain and temperature [83], by considering that the MMF has the advantage of easy coupling. These applications, however, are similar to the sensing applications of single-mode FBGs, so that it does not have practical advantages over the FBGs in SMFs.

2.7.2 LPG in GRIN MMF

The interest on LPG in the SMFs, normally with the period of hundreds of microns, have grown rapidly since it was first reported [18]. The applications of SMF LPGs, have been exploited fruitfully in a number of fields, from optical communications to optical fiber sensors [19, 20, 84].

While single-mode LPG attracts enormous interest, LPG in MMF has not been thoroughly investigated. Only few studies had been carried out in literature for its sensing applications [33, 34]. Lee *et. al.* presented a chemical sensor based on the transmission characteristics of a multimode fiber LPG to measure the Methylene Blue (MB) dye concentration of the MB solutions [33]. The transmitted intensity of the MMF LPG was found to decrease linearly with the increase of the logarithmic concentration of the MB solution. The LPG in MMF was proposed to measure the refractive index changes [34]. Their experimental results showed that the transmitted power reduced when the surrounding liquid refractive index increased. Their results, however, was only in the preliminary stage, and their results did not prove the MMF LPG's application as a satisfactory refractive-index sensor.

2.7.3 GRIN MMF with Periodic Microbend

Fibers can be subject to two types of bends: (a) Macrobends: macroscopic bends having radius that are large compared with the fiber diameter. An example for such macrobends is the fiber turning at a corner. And (b) Microbends: microscopic bends having small-scale fluctuations in the radius of curvature of the fiber axis. According to its forming mechanism, microbends can be classified into random microbends and periodic microbends. Since bends will lead to radiation loss or bending loss, random microbends need to be avoided during manufacturing of the fiber and cabling of the fiber. Periodic microbends, however, can introduce strong mode coupling in an MMF

as well as significant radiation loss, so that it was proposed and implemented as a kind of effective optical fiber sensors to measure a number of environment parameters. In a series of periodic microbends, the radiation loss (bending loss) is dominated.

The principle of microbend sensors is similar to the physical mechanism that makes an LPG to work, as both devices depend on the co-propagation mode coupling. This similarity has been employed to produce the LPG in an SMF using the periodic microbend structure [3]. The amount of power coupled from the core modes to the cladding modes can be detected as a transmission power loss. By monitoring the variation of transmission power, the sensed parameters can be effectively obtained.

Periodic microbend in an MMF has been used as an optical fiber sensor since the 1980's [38, 71, 85]. Microbend sensor, as one of the earliest optical sensors, originated from microbend loss, the very phenomenon that needs to be avoided in the optical communications [40]. Sensors based on microbend loss in optical fiber was first proposed and demonstrated in 1980 [85]. Then the early interest in this kind of sensors was for hydrophone applications [38]. Since that time, with hundreds of studies appeared in this topic, the microbend sensors have been widely used in the measurements of different kind of environment parameters. In 1987, Lagakos *et. al.* have published an excellent analysis of microbend fiber sensors, presenting very useful formulas for microbend modeling and design [39].

Microbend sensor is one kind of the most cost-effective fiber sensor owing to the intensity based measurement, which can be easily adapted without the requirement of expensive and elaborate system design. The intensity measurement, however, in a way limits the resolution and sensitivity of the sensor system. Therefore, the microbend sensor is not suitable for high sensitivity applications. Another disadvantage of the microbend sensor is the requirement of the microbend deformer, which in most cases affects the compact packaging of such devices.

Interestingly, in 1997, a microbend fiber sensor structure using SMF leads was proposed by Donlagic *et. al.* [48, 86]. Such sensors were configured in SMF-MMF-SMF (SMS) as shown in Fig. 2.10. It has many advantages over conventional microbend sensors, such as high sensitivity and good modal stability [86]. Therefore such SMS structures allow the use of shorter microbend deformer to achieve the same sensitivity as the conventional microbend sensors. The disadvantage of the SMS sensor structure is the extra power loss at the MMF to SMF splicing point.

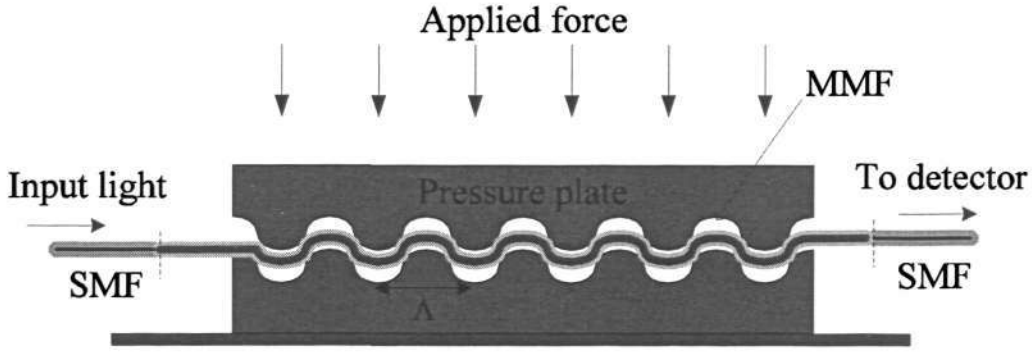

Fig. 2.10 SMS microbend sensor structure

Other applications using the periodic microbend in MMF have also been proposed. The use of a permanently microbent MMF as a chemical sensor was reported by Lee *et. al.* [87], demonstrating the usefulness of a permanently microbent fiber in measuring the properties of surrounding materials. Apart from good intensity based sensors, microbent fibers have found applications as mode converters and mode scramblers [28], appearing as commercialized products widely available in the market.

Obviously, the study on periodic structures in GRIN MMF still remains in early stages, especially for FBG and LPG in GRIN MMF. In Table 2.2, the estimated number of current available publications for this particular area is given to our knowledge, while that for periodic structures in SMF is also presented for comparison.

Table 2.2: Total number of publications for different areas

	FBG	LPG	Periodic Microbend
In SMF	Hundreds of	Hundreds of	< 20
In MMF	< 15	< 5	> 100

CHAPTER 3

BRAGG GRATING IN GRADED-INDEX MULTIMODE FIBER

3.1 Overview

FBGs or short-period fiber gratings written in SMFs have been extensively studied since 1990s with fruitful applications in optical communications and optical fiber sensors, FBG in multimode fiber (MMF) began to attract attention only in recent years.

This chapter is dedicated to the discussions on fabrication, analysis and characterization of FBG in GRIN MMF. The fabrication and characteristics of the MMFBG are described. In the experiment, MMFBG is produced by UV laser irradiation using the phase mask technique. The MMFBG spectrum and the spectral evolution at different mode excitation condition are examined theoretically and experimentally. Besides, the response of an MMFBG to temperature and strain are demonstrated.

3.2 Fabrication

The phase mask technique is used to fabricate the MMFBGs. The setup for the FBG fabrication system is shown in Fig. 3.1. The high power UV light is generated by a frequency doubled Argon laser at the wavelength of 244 nm, which is directed to the grating under fabrication via an acoustic optic modulator (AOM) and a series of UV mirrors. The function of the AOM is to modulate the UV light into a series of pulses. Each of the pulses corresponds to one exposure of UV light on the fiber, and leads to the formation of hundreds of pitches in the fiber under fabrication. Focused beam reaching the phase mask generates fringe patterns that lead to grating structure in the fiber. The grating under fabrication is fixed on a motion-controlled stage having the resolution of 2 nm, and thus can be controlled to motion along its z-axis. The slowly moving fiber is translated along the pulsed interface fringes in synchrony with pulses. The technique with a moving fiber and a fixed phase mask during the fabrication is known as scanning fiber technique, which allows a flexible grating length by moving the fiber along its axis. The phase mask can be tilted with a small angle to form the tilted fiber grating by tuning a goniometer with the resolution of 0.1°. Therefore the grating length is not limited by the length of phase mask. During fabrication, the transmission spectrum of the grating is monitored by a C + L broadband ASE source (Photonik) and an optical spectrum analyzer (OSA) (ANDO AQ6317B), which provides the real time information for the FBG under fabrication.

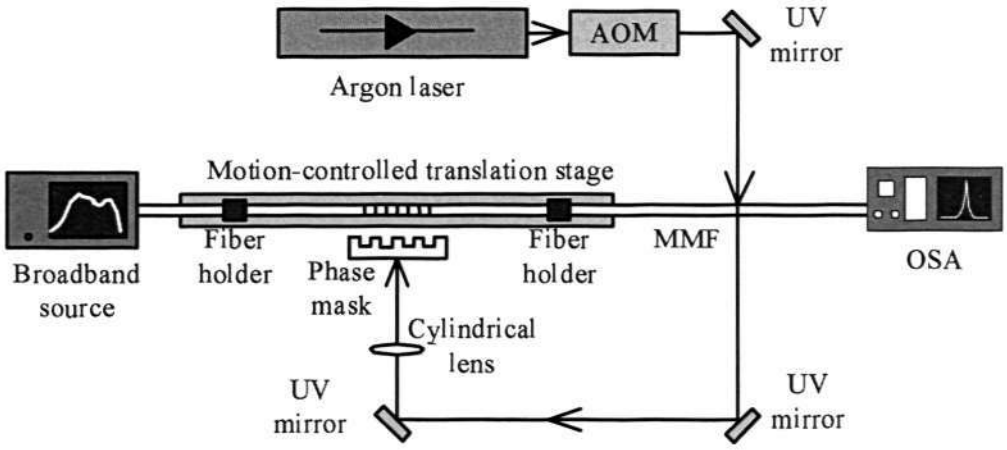

Fig. 3.1 Phase mask technique based FBG fabrication system [66]

A standard GRIN MMF with a parabolic profile was used to fabricate the FBG, which has the following parameters: overall core diameter $d = 62.5\ \mu m$, core index $n_{co} = 1.477$, and cladding index $n_{cl} = 1.447$. The operating wavelength is fixed at $\lambda = 1550$ nm. This fiber supports 19 principal modes, which is calculated with Eq. (2.20). Prior to the grating fabrication, the MMF had been hydrogen-loaded under a pressure of 110 bar and a temperature of 80 °C for 7 days. A phase mask with the period of 1058.04nm was used for fabricating the 20mm long MMFBG. A fter the grating fabrication, annealing at a temperature of 100 °C for 24 hours was performed, which stabilized the grating performance.

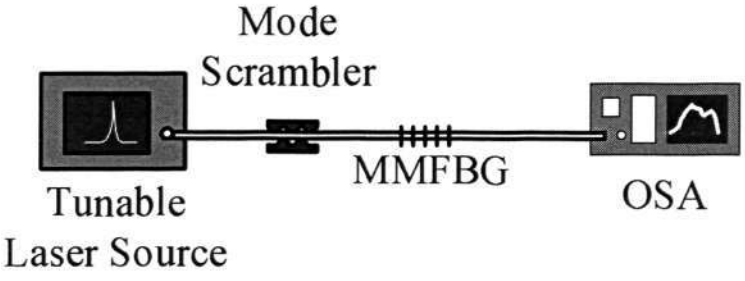

Fig. 3.2 Experimental setup for measuring the spectral responses of an MMFBG

The MMFBG transmission spectra at different modal power distributions were measured using a tunable laser source (ANDO AQ4321D) and an OSA (ANDO AQ6317B), as shown in Fig. 3.2. The modal power distribution was modified by tuning a mode scrambler (Newport) at the input of the MMF. Fig. 3.3 shows the transmission spectra of the MMFBG measured at different mode excitation conditions.

The results presented in Fig. 3.3 confirmed that the MMFBG spectrum relies on the modal power distribution in the MMF. In Fig. 3.3 (a), the tunable laser source has been launched into the MMF via a center-connected SMF pigtail. With the mode scrambler remaining in a few-mode excitation state, only few lower order modes were preferentially excited at the input of the MMF, which correspond to those transmission dips at longer wavelengths. In the result shown in Fig. 3.3 (b) and (c), the mode scrambler applied to the MMF was tuned to a medium and a highly mode excitation states, respectively, resulting in different mode excitations. It can be seen that, compared to Fig. 3.2 (a), there are many transmission dips associated with different fiber modes with considerable transmission loss.

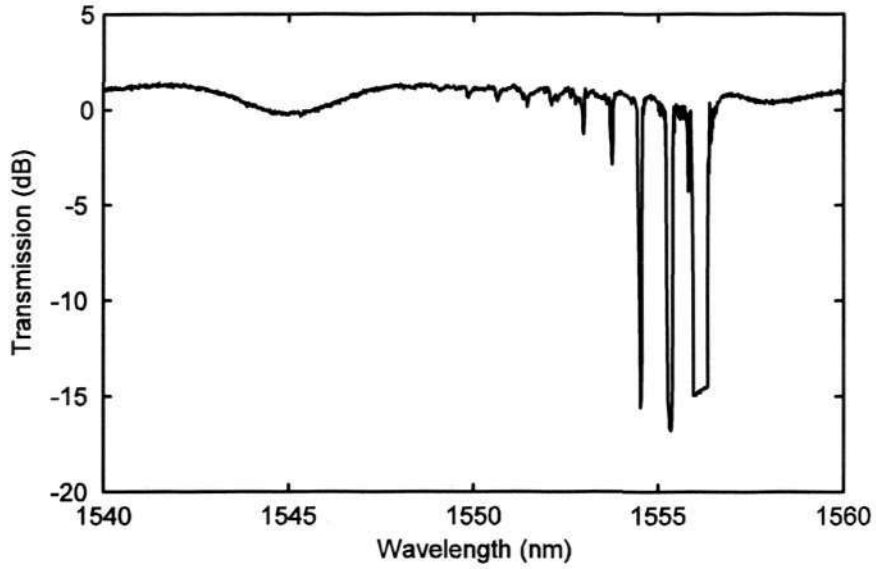

(a)

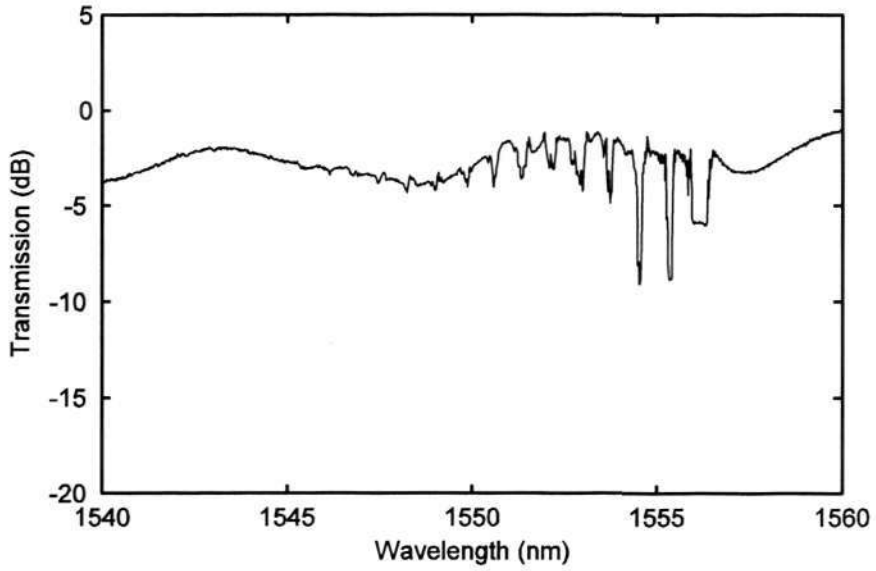

(b)

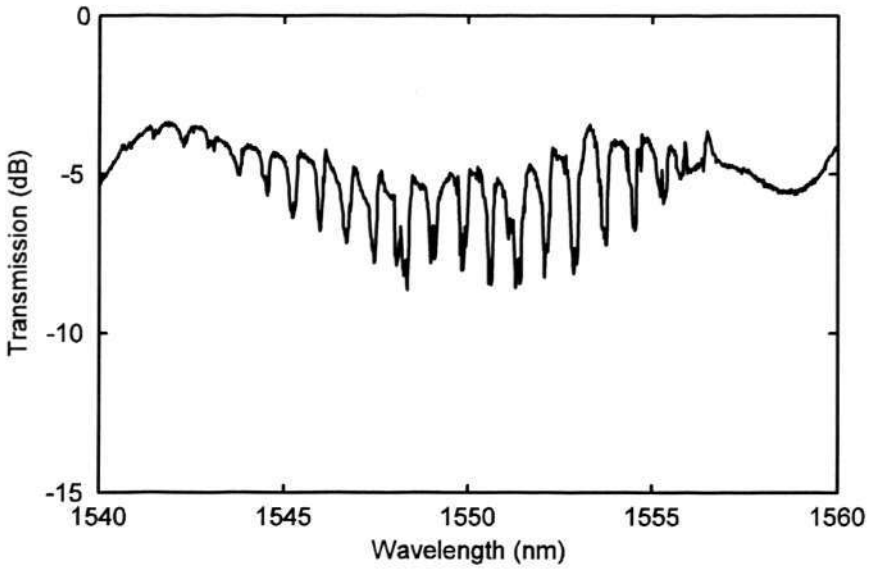

(c)

Fig. 3.3 Transmission spectra of a uniform MMFBG for (a) few-mode excitation, (b) medium-mode excitation, and (c) highly-mode excitation

3.3 Spectral analysis

From the coupled mode theory [62] and the analyses in Section 2.5, it is known that counter-propagating mode coupling dominates in the presence of short period grating structures. For a uniform MMFBG, counter-propagating mode coupling takes place not only between the forward and the reverse waves of an identical core mode but also between the forward and the reverse waves of core modes in different orders, where the phase matching condition is given as

$$\beta_n^{(+)} - \beta_m^{(-)} = \beta_n + \beta_m = \frac{2\pi}{\Lambda}, \tag{3.1}$$

β is the propagation constant; superscripts (+) and (–) denote the mode traveling in the (+) and (–) directions along the fiber z-axis; and subscripts n and m refer to mode

orders, which could be in either the same or distinct values, describing the forward and reversed mode coupling between an identical mode or modes in different orders.

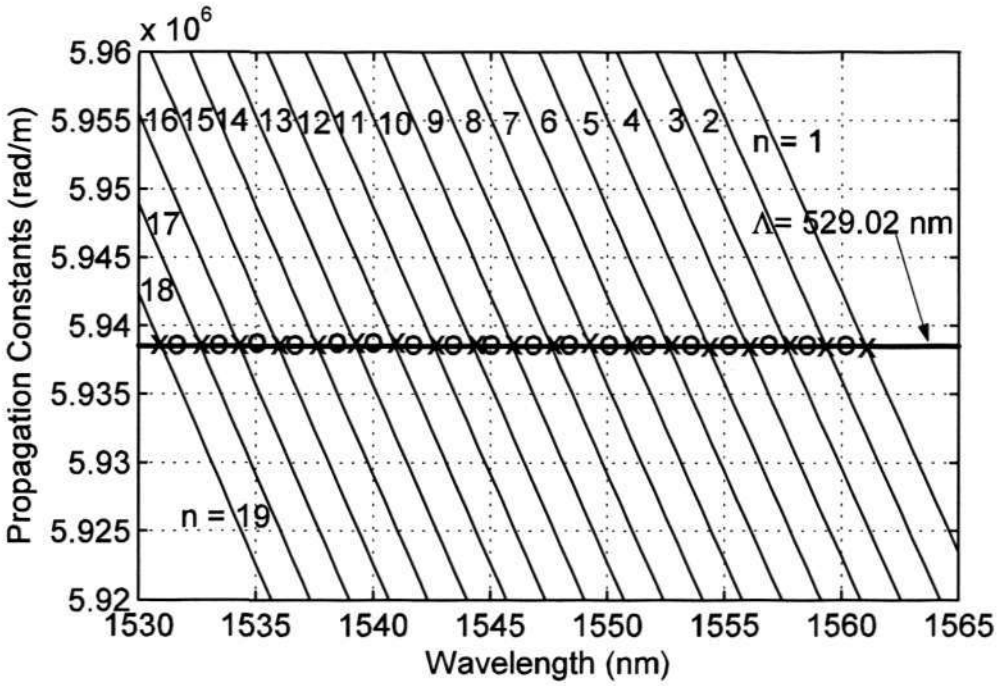

Fig. 3.4 Phase matching of mode coupling in terms of principal modes for a uniform MMFBG.

According to Section 2.4, the core modes guided in the MMF fall into the category of the principal mode groups corresponding to their respective propagation constants. Thus in Eq. (3.1), β is indeed the propagation constant for the principal mode groups, and therefore is calculated using Eq. (2.21). Fig. 3.4 shows the propagation constants as a function of the wavelength from 1530 nm to 1565 nm, which explains spectral response of an MMFBG. Tilted lines are the variations of the propagation constants with wavelength for principal mode groups that have a discrete distribution from n = 1 to 19. The horizontal line denotes the grating with the period

529.02 nm (formed using the 1058.04 nm phase mask). Crosses indicate the wavelengths where the phase matching conditions are satisfied for the coupling between the forward and reverse waves of the identical principal mode groups, while the circles denote the wavelengths where the phase matching conditions are satisfied for the coupling between the principal mode groups with different orders. Since the grating period is fixed at 529.02 nm (the horizontal line), all the reflections are confined in the horizontal line in the figure. The GRIN MMF supports 19 principal modes at the wavelengths around 1550-nm. Therefore the crosses in the figure show the wavelengths for phase matching at which the reflections to the identical mode occur. In the meantime, the reflections of the mode groups in different orders are also considered, since counter-propagating modes in distinct orders can satisfy the phase matching condition (Eq. (3.1)) as well. Those reflections of the mode groups with different orders can be recognized easily in Fig. 3.4, given by open circles. For simplicity, the reflection wavelengths are expressed in terms of n from the long wavelength to short wavelength as λ_n (n can be one of the numbers from 1 to 37).

Therefore, by considering the reflections taking place for the identical mode and the modes in different orders separately, the phase matching conditions in an MMFBG can be given in the form

$$2\beta_n(\lambda_{2n-1}) = \frac{2\pi}{\Lambda}, \tag{3.2}$$

$$\beta_n(\lambda_{n+m-1}) + \beta_m(\lambda_{n+m-1}) = \frac{2\pi}{\Lambda}. \tag{3.3}$$

Now Eqs. (3.2) and (3.3) are obtained, and they are very important conclusions showing every possible phase matching in an MMFBG. Eq. (3.2) is the phase matching condition for the coupling between the forward and reverse waves of an arbitrary identical mode, while Eq. (3.3) expresses the phase matching condition for the mode coupling between the forward and reverse waves of the principal modes with different orders, where β is given as a function of λ_n. Given two principal modes with orders n and m, the wavelength λ, where the coupling takes place between these two modes, can be identified easily with the help of Eq. (3.3). And the wavelength where the mode coupling occurs within an identical mode can be predicted using Eq. (3.2).

It can be noted that in Fig. 3.4 the excited lowest order mode is much broader than other modes. The reason is considered as below. Each transmission dip in the figure corresponds to a principal mode group, which consists of several modes. These modes in a principal mode group have similar but slightly different propagation constants. The propagation constants involved in the lowest order principal mode may have a relatively larger difference than other principal mode groups. Therefore, when the modes in the lowest principal mode group are excited sufficiently, a relatively broad spectrum is observed for the first transmission dip.

The spectra analyses carried out in this section, in particular Eqs. (3.2) and (3.3), find good agreement with the measured transmission spectra shown in Fig. 3.3. In Fig. 3.3 (c), it can be seen that the reflections spread over a wide wavelength range in the highly mode excitation condition. This is as what was predicted by the theoretical analyses. It should be also noted that, the wavelengths, where the particular reflections take place in the measurement, are not exactly the wavelengths that are shown by the theoretical calculations. The reason is that the reflection wavelength might be affected by the strain applied on the fiber and environment temperature, and furthermore the refractive index profile used in the calculation might slightly differ from the actual profile of the MMF used in the experiment. In Fig. 3.3 (b), the reflection to the higher-order modes can hardly be observed, as the higher order modes near cut off will easily transfer their power to cladding modes.

The above analysis is carried out in the 1550nm wavelength region, because such a region is most commonly used for data transmission. The phase matching of mode coupling given in Eqs. (3.2) and (3.3), however, should be applicable to other wavelength regions. In order to verify this, the calculated propagation constants, as a function of wavelength at 850-nm region and 1310-nm region, are shown in Fig. 3.5. The fiber parameters used in the calculations are assumed to be the same as those at 1550-nm region. There are 34 and 22 principal modes for the propagation constants at 850-nm and 1310-nm respectively, which would lead to the 67 and 43 reflections in the MMFBG spectra including the coupling of forward and reverse waves of an

identical mode and forward and reverse waves of adjacent modes. It can be seen that the propagation constants of different principal mode groups are like parallel lines over a wide wavelength range. The results shown in Fig. 3.5 are similar to the propagation constants calculated by others [32, 88]. It is because that when the WKB method is used to calculate mode propagation constants of a GRIN MMF the effect of material dispersion is neglected and the particular interest is in the intermodal dispersion. This approximation is valid as the material dispersion is negligible compared with the intermodal dispersion.

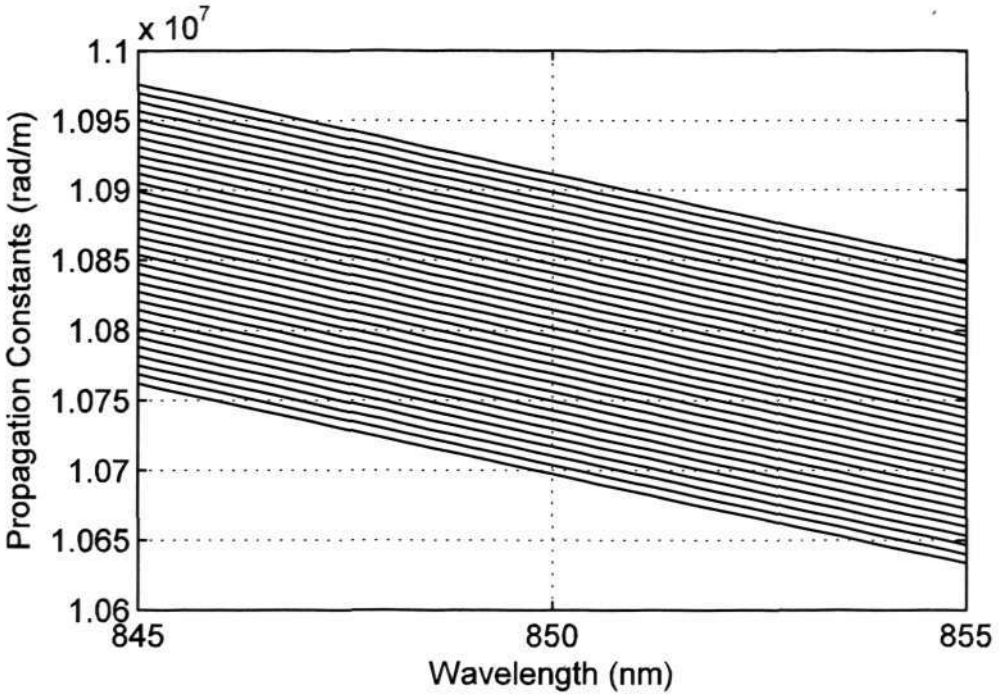

(a)

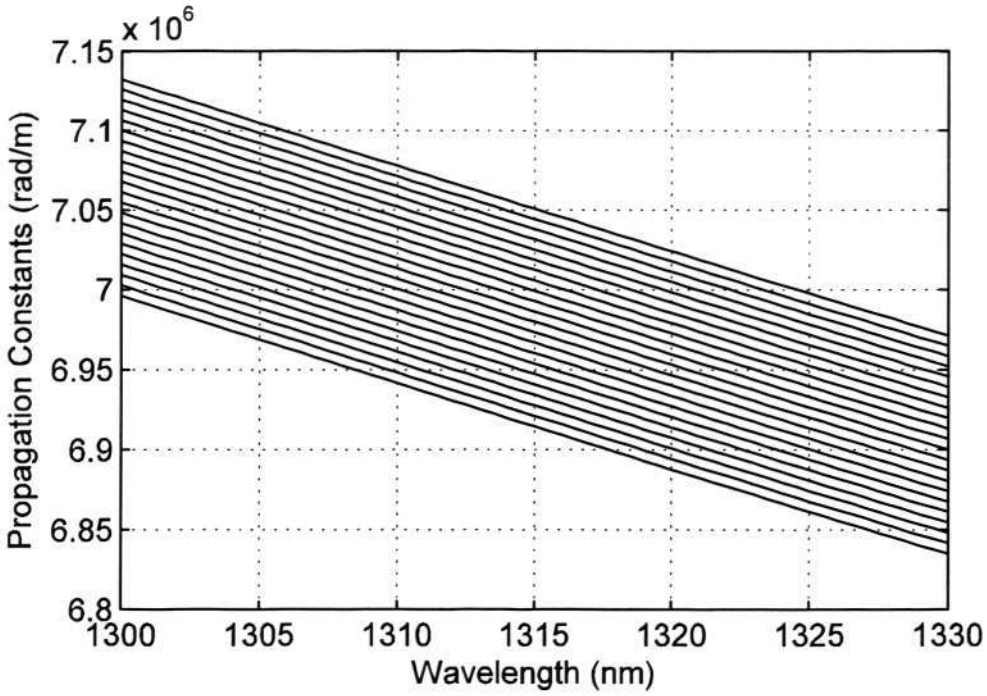

(b)

Fig. 3.5 Calculated propagation constants of principal modes as a function of wavelength at (a) 850nm region (n = 1 to 34), and (b) 1310nm region (n = 1 to 22).

The wavelength separation between two adjacent reflections can also be estimated based on the WKB analysis mentioned in Chapter 2, as the reflections are determined by the propagation constants of the principal mode groups. The wavelength separation between the reflections of two adjacent principal mode groups can be given as

$$\Delta\lambda_{n-n} = 2 \cdot \Delta n_{eff} \cdot \Lambda , \tag{3.4}$$

and the wavelength separation of adjacent reflections is estimated as

$$\Delta\lambda = \frac{\Delta\lambda_{n-n}}{2} = \Delta n_{eff} \cdot \Lambda , \tag{3.5}$$

where Δn_{eff} is the difference in effective indices between two adjacent principal mode groups and is given by

$$\Delta n_{eff} \approx \frac{\Delta\beta \cdot \lambda}{2\pi}. \tag{3.6}$$

$\Delta\beta$ is known as the difference between propagation constants of two adjacent principal modes, with the analytical expression:

$$\Delta\beta = \frac{\sqrt{2\Delta}}{a}. \tag{3.7}$$

With the help of Eqs. (3.5)- (3.7), the wavelength separation of two adjacent reflections is calculated as ~0.84 nm using the GRIN MMF parameters at λ = 1550 nm, overall core diameter d = 62.5 μm, core index n_{co} = 1.477 and cladding index n_{cl} = 1.447. The calculated figure fits the experimental results very well, which is very close to the wavelength separation observed in Fig. 3.3.

3.4 Mode Coupling in an MMFBG

To identify the reflection strength in the MMFBG spectrum is a far more complicated mission than to locate wavelengths for those reflections, as the calculation requires the understanding of the exact refractive index profile along the MMFBG. Nevertheless, it is possible to propose a method to analyze the mode coupling in an

MMFBG, and this section is focused on the derivation of equations for mode coupling and coupling coefficients in an MMFBG.

From the coupled mode theory reviewed in Chapter 2, the coupling coefficient for two modes n and m can be given as [89, 90]

$$K_{nm}^{t}(z)=\frac{\omega}{4}\int_{0}^{2\pi}\mathrm{d}\varphi\int_{0}^{\infty}r\mathrm{d}r\Delta\varepsilon(r,z)\bar{E}_{n}^{t}(r,\varphi)\bar{E}_{m}^{t*}(r,\varphi), \tag{3.8}$$

where the superscript t denotes the transverse vector components only, $\Delta\varepsilon(r,z)$ describes the UV-induced index perturbation, which is assumed to be independent of φ, $\bar{E}$ is the transverse component of the mode field, ω is the angular frequency of light, and symbol * denotes the conjugation operation. The longitudinal coupling coefficient K_{mn}^{z} is neglected here, since it is generally 2-4 orders of magnitude smaller than K_{mn}^{t}.

Eq. (3.8) suggests that the calculation of coupling coefficient K requires the understanding of the index profiles of the fiber after UV irradiation. It is reasonable to assume that the UV-induced grating only exists in the fiber core, changing the core index to $n_{co}(r, z)$ but leaving the cladding index unchanged.

Unlike the SMF subjected to UV irradiation, the UV-induced index change in an MMF includes two major perturbations, namely the index change along fiber axis and the index change in fiber radial direction. The latter one is usually neglected in the case when SMF is considered.

A. Axial perturbation

In the analysis here, it is assumed that when an FBG is induced in MMF, it exists only in the fiber core, changing the core index to $n_{co}(r,z)$, and leaving the cladding index unchanged. The axial index perturbation of an MMFBG, which is similar to the FBG in SMF, can be given as follows [89, 90]:

$$n_{co}(r,z) = n_{co}(r)\{1+\sigma(z)[1+m\cos(\frac{2\pi}{\Lambda}z)]\}. \tag{3.9}$$

Here $n_{co}(r)$ is the unperturbed core index, Λ is the grating period, m is the induced-index fringe modulation, where $0 \leq m \leq 1$, and $\sigma(z)$ is the slowly varying envelope of the grating. Thus the peak induced index change is $\sigma(z)n_{co}(r)(1+m)$, while the minimum index change is $\sigma(z)n_{co}(r)(1-m)$. The product $\sigma(z)n_{co}(r)$ describes the profile of dc induced index change, averaged over a grating period. Essentially, $\sigma(z)n_{co}(r)$ can be arbitrarily shaped, such as the uniform distribution or the Gaussian distribution. For the Gaussian grating,

$$\sigma(z) = \sigma\exp\left(-4\ln 2\left(z^2/w^2\right)\right), \tag{3.10}$$

where w is the full width a half-maximum (FWHM) of the grating profile.

Fig. 3.6 is an illustration of the axial index perturbation (Gaussian distribution) for an MMFBG at $r = 0$, where the grating period relative to the length w has been exaggerated for clarity.

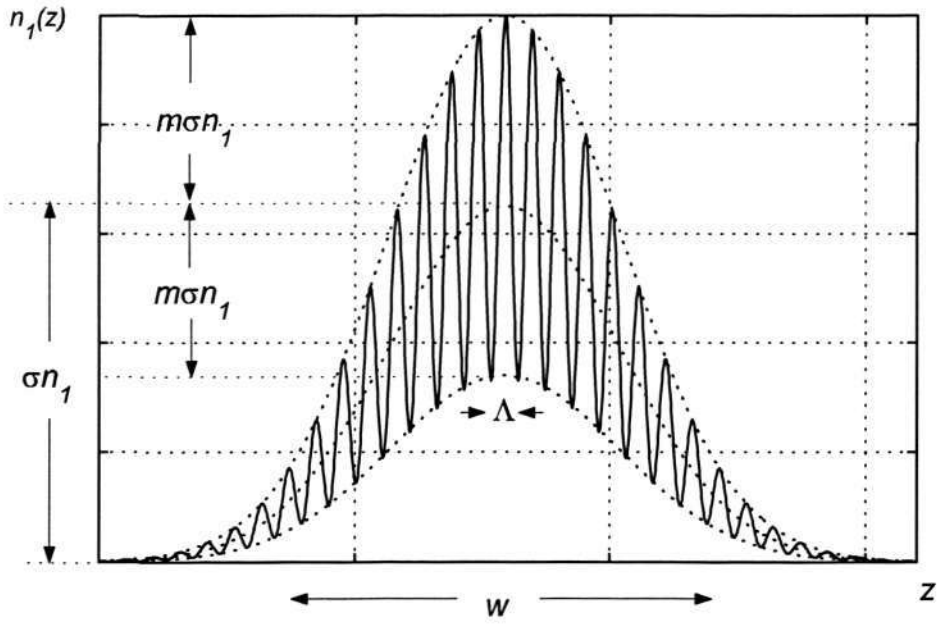

Fig. 3.6 Axial index perturbation at (r = 0) with a Gaussian distribution for the MMFBG (The grating period (Λ) relative to the grating width (w) has been exaggerated for clarity)

B. Radial perturbation

In an optical fiber, the guided modes form an orthogonal set and any overlapping integral between two modes has zero value. Hence the radial perturbation is essential for the mode coupling taking place between modes in different orders.

The existence of radial perturbation along the grating region (which is whether the refractive-index index change of the MMFBG along the cross section of the MMF is homogeneous or inhomogeneous) was confirmed by experimental results, since the mode coupling between the counter-propagating modes with different orders was observable and had significant efficiency in the reflection spectra shown in Fig. 3.3. This should be the results of varying Germanium concentrations on the radial

direction of GRIN MMF. The radial index perturbation, however, is a much more complicated problem than the axial perturbation, as it is distributed non-uniformly and always depends on both fiber properties and grating fabrication technique. Therefore, to find the exact radial perturbed index profile can be recommended for future work of this thesis.

The general coupled-mode equations that describe changes in the forward and reverse amplitudes of a mode m that results from the presence of other modes have been given in Chapter 2. As the FBG only induces the counter-propagating mode coupling, the coupled mode equations are simplified as follows [89, 90]:

$$dc_{\mu}^{(+)} / dz = \sum_{\nu} K_{\mu\nu} c_{\nu}^{(-)} \exp[i(\beta_{\mu} + \beta_{\nu})z], \tag{3.11}$$

$$dc_{\mu}^{(-)} / dz = \sum_{\nu} K_{\mu\nu} c_{\nu}^{(+)} \exp[-i(\beta_{\mu} + \beta_{\nu})z]. \tag{3.12}$$

where two approximations have already been made to Eq. (3.11) and Eq. (3.12). The first approximation is to neglect the longitudinal coupling coefficients, because they are substantially smaller than the transverse coefficients, as is mentioned before. A second approximation is to ignore the coupling among cladding modes, including the coupling between the core mode and the cladding mode, and the coupling among the cladding modes.

In order to calculate the spectral response of an MMFBG, further simplification can be made for the mode coupling, by taking into account the phase matching

conditions shown in Eqs. (3.2) and Eq. (3.3). Therefore, in practice, only the nearly phase matched or phase matched coupling are kept for further calculations.

3.5 Sensitivity characteristics of an MMFBG

From the spectral analyses carried out in Section 3.4, one knows that the MMFBG effectively encodes the light in a particular mode by the Bragg wavelength condition for that mode. This is a unique and novel property which could lead to a range of new sensing concepts. The sensing application of an MMFBG was first proposed by Wanser [80], where the mode interference is proposed to monitor many environment parameters. This section is to describe the response of different fiber modes in a uniform MMFBG to temperature and strain.

Most of the work on FBG sensors has focused on the use of these devices to provide effective sensing of temperature and strain [2, 15]. The temperature response arises due to the inherent thermal expansion of the fiber material and the temperature dependence of the refractive index, whereas the strain response arises due to both the physical elongation of the sensor, and the change in fiber index due to photoelastic effects. For an SMFBG, the shift in Bragg wavelength with temperature and strain can be expressed using

$$\Delta\lambda_B = 2n\Lambda\left(\left[\alpha+\frac{1}{n}\frac{dn}{dt}\right]\Delta T+\left\{1-\left(\frac{n^2}{2}\right)\left[P_{12}-\nu\left(P_{11}+P_{12}\right)\right]\right\}\varepsilon\right), \tag{3.13}$$

where $\Delta\lambda_B$ is the wavelength shift, ΔT is the temperature change, ε is the applied strain, $P_{i,j}$ coefficients are the Pockel's (piezo) coefficients of the stress-optic tensor, v is the Poisson's ratio, and α is the coefficient of thermal expansion (CTE) of the fiber material.

Although in an MMFBG response to temperature and strain arise due to the same mechanisms as in a single-mode FBG, the response to different reflections has to take into account the properties of different modes. The temperature or strain dependence of reflections of an FBG in GRIN MMF can be evaluated with the help of Eq. (2.21). For simplicity, it is assumed that the second term in the square root of Eq. (2.21) is much smaller than unity and that the numerical aperture is approximated by $NA = n_{co}\sqrt{2\Delta}$, yielding

$$\frac{d\lambda_m}{dx} = \frac{\lambda_m^{\,2}}{2n_{co}\Lambda^2}\frac{d\Lambda}{dx} + \left[\frac{\lambda_m^{\,2}}{2n_{co}^2\Lambda} - \frac{\lambda_m^2 m(3n_{cl}-2n_{co})}{2\pi a n_{co}^2\sqrt{2n_{co}(n_{co}-n_{cl})}}\right]\frac{dn_{co}}{dx}$$

$$+\frac{\lambda_m^2 m}{2\pi a n_{co}\sqrt{2n_{co}(n_{co}-n_{cl})}}\frac{dn_{cl}}{dx}, \qquad (3.14)$$

where λ_m is the Bragg wavelength for the reflection of m^{th} principal mode group, x is either the temperature or strain. Thus $d\lambda_m/dx$ is the variation of Bragg wavelength corresponding to either temperature or strain. The terms dn_{co}/dx and dn_{cl}/dx for silica are almost the same value and are very small [32, 91]. Therefore, for these small values, the increase of m from 1 to maximum (the fiber used here has the maximum m = 19) is insignificant to the total wavelength shift $d\lambda_m/dx$. As a result, theoretically the reflection peaks in the MMFBG spectrum have almost the same temperature or strain

dependence for all m.

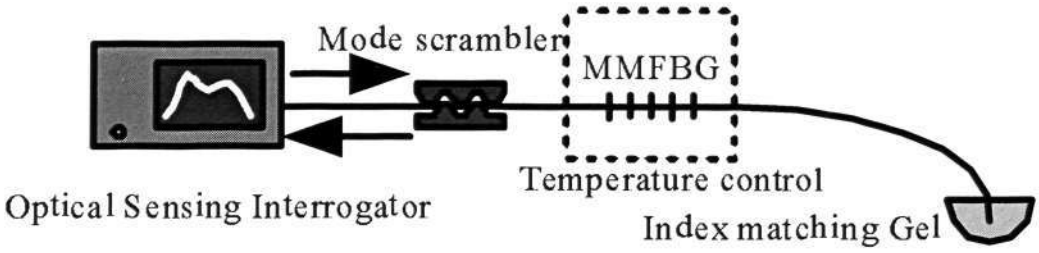

(a)

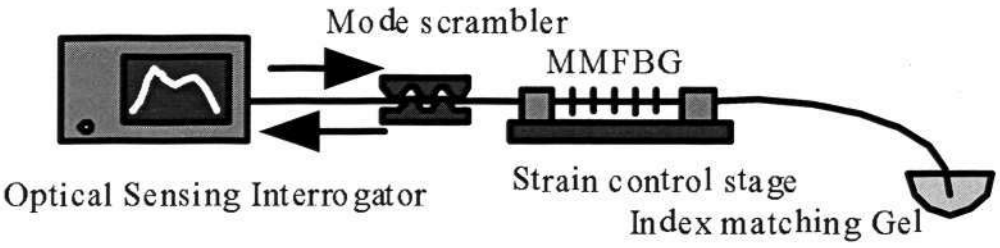

(b)

Fig. 3.7 Experimental setups for measuring (a) temperature, and (b) strain response of a uniform MMFBG

Fig. 3.7 (a) illustrates the experimental configuration for measuring temperature response of a uniform MMFBG. The MMFBG, written using the phase mask technique at the period of 529.02 nm, was placed in a temperature-controlled chamber, where the temperature reading can be taken easily. The Optical Sensing Interrogator (Micron Optics SI425), consisting of a broadband source and demodulation system, served as the light source and the detector to demodulate the wavelength information from the reflected light. A mode scrambler (Newport) was used to excite more high-order modes. Index-matching gel was applied to eliminate unwanted reflection at the other end of the grating. In the strain response measurement, the configuration shown in Fig. 3.7 (b) was employed, which is similar to the temperature measurement,

except that the temperature-controlled chamber was replaced by a strain-controlled stage

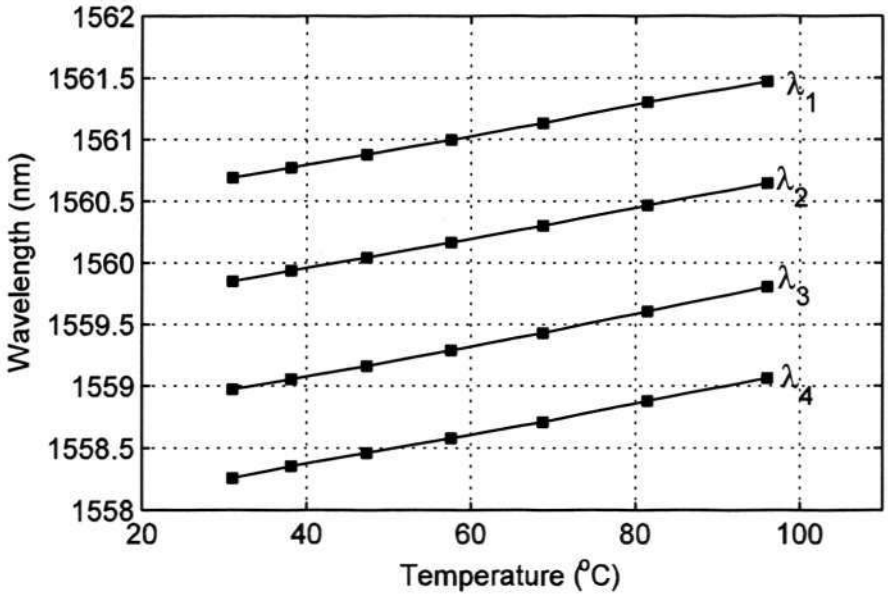

(a)

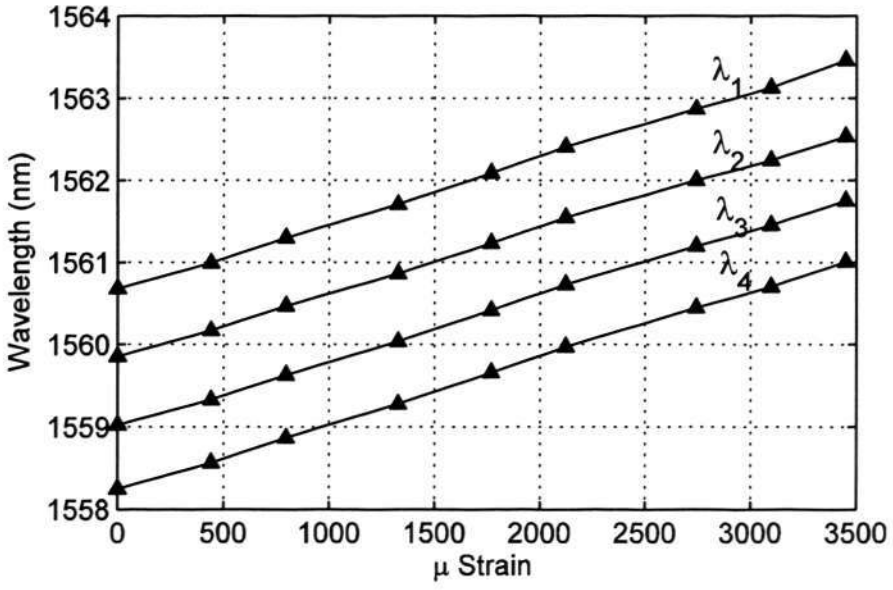

(b)

Fig. 3.8 Response of the first 4 reflections in the MMFBG spectra to (a) temperature, and (b) strain

Fig. 3.8 shows the experimental results of the MMFBG response to temperature and strain for different reflections in the spectrum. λ_n denotes the n^{th} reflection in the MMFBG spectrum (according to Section 3.3). The first 4 reflection peaks had the same response to temperature and strain, and therefore, in Fig. 3.8, are displayed as parallel lines. The discussion made above based on Eq. (3.14) suggests that different reflections of an MMFBG have the similar responses to temperature and strain, and therefore agrees with the experimental results in Fig.3.9. The sensitivities of our MMFBG to temperature and strain are 11.4pm/°C and 0.8pm/μ-strain, respectively, for all reflections. Thus each reflection peak in the MMFBG spectrum can be used as an independent sensing channel for either temperature or strain measurement. The dynamical range of the MMFBG is similar to single-mode FBG.

Usually a limitation of the UV-induced FBGs for high-temperature sensing applications is that operation of sensor at elevated temperature results in the erasure of the UV-induced index modulation of the grating. In order to implement high-temperature FBG sensors, an FBG fabricated in a sapphire fiber is used as the sensing element, achieving a temperature as high as 1500 °C without observed degradation of grating strength [92].

3.6 Conclusions

MMFBG, fabricated using high-power UV exposure, has a tunable spectral response that could lead to interesting applications. A detailed spectral analysis and a mode

coupling study were carried out for the MMFBG, enabling the recognition of reflections to different principal mode groups in the grating spectrum. The response of different reflection peaks at the grating spectrum to the temperature and strain were examined, showing that each peak was capable of strain and temperature sensing applications.

CHAPTER 4

LONG PERIOD GRATING IN GRADED-INDEX MULTIMODE FIBER

4.1 Overview

This chapter studies the LPG in GRIN MMF formed with CO_2 laser irradiation, covering the grating fabrication, mode coupling, properties, and potential in sensing applications.

Long-period gratings (LPGs) formed in single-mode fibers (SMFs) have been studied extensively over the recent years owing to their many applications in optical communications and fiber optical sensors [18, 19]. On the other hand, there has been little work on the study of LPGs fabricated in multimode fibers [33-35]. The reason is that a multimode fiber LPG does not produce a band-rejection filter response, i.e., a transmission spectrum that exhibits distinct rejection or passing bands. In experiment, both UV and CO_2 laser fabrication techniques are used to form multimode fiber LPG with a range of grating periods. However, there is no rejection band observed in their transmission spectra. This explains why only little work on multimode fiber LPG was reported so far. In the meantime, it should be recognized that the large amount of early works on microbend sensors constructed by applying periodic microbending

along multimode fibers (see, for example, [39, 85]). A microbend sensor can be considered as a mechanically induced LPG in a multimode fiber, albeit a temporary one depending on the presence of microbending. Therefore, it is expected that multimode fiber LPGs in general should find applications as intensity-based sensors. However, the strain sensitivity that can be offered by a multimode fiber LPG written by the UV-irradiation method is likely to be low, as the UV irradiation can change only the refractive index of the fiber core [18, 33, 34]. To offer a high strain sensitivity, a periodic change in the geometric structure of the fiber is desired [77, 78].

In this chapter, the long period grating, formed by exposing a GRIN MMF to a CO_2-laser beam point by point along the fiber, is presented. The laser beam is intense enough to deform the fiber locally, so that a periodic variation in the fiber diameter (i.e., a periodic taper) is achieved. Firstly, the mode coupling, in a long period grating written in GRIN MMF, is analyzed, where the coupling equations, coupling coefficients and coupling periodicity are investigated. Then the multimode fiber LPGs fabricated with a CO_2 laser are demonstrated. The effects of the pitch, the degree of deformation, and the number of periods on the transmission of the grating are measured and discussed. To demonstrate the potential of the grating as an effective physical or chemical sensor, the responses of the grating to axial strain and surrounding refractive index are measured.

4.2 Fabrication

As discussed in Chapter 2, the state-of-art techniques for fabricating the long period grating (LPG) include: UV laser or CO_2 laser irradiations. The CO_2 laser fabrication technique is cost-effective and easy to implement.

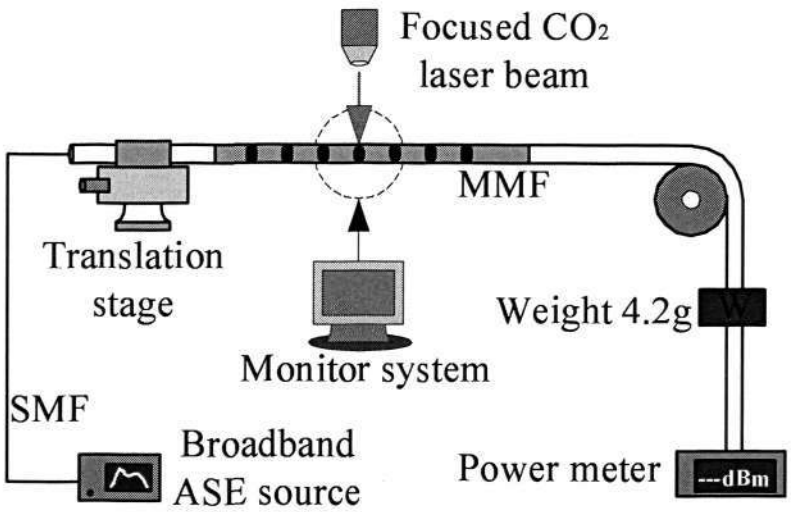

Fig. 4.1 Schematic of CO_2 laser based LPG fabrication system

Fig. 4.1 illustrates the point-by-point CO_2-laser irradiation system implemented for the fabrication of LPGs. The CO_2 laser (Synrad J48-1, 2.5-W full power) incorporated a galvanometer that directed and focused the laser beam to a Gaussian spot of ~180 μm at the focal point on the fiber under laser irradiation. One end of the fiber was fixed on a motion-controlled translation stage and the other end was attached to a ~4.2-g weight so that the fiber was subject to constant tension during laser irradiation. Two CCD cameras were employed to monitor the irradiation process. To form a grating with a pitch Λ, the fiber was made to translate a constant distance Λ in the axial direction after each exposure. The fiber used here was a standard GRIN

MMF with a parabolic index profile having the following nominal parameters: overall diameter 125 μm, core diameter = 62.5 μm, core index 1.477, and cladding index 1.447 (at the wavelength 1550 nm). The jacket of the fiber section under irradiation was removed. As shown in Fig. 4.1, to measure the transmission characteristics of the fabricated LPG, light from a C+L broadband ASE source (Photonik) was launched into the fabricated LPG via a short SMF pigtail and the output power from the grating was measured with a power meter (Agilent 81634B, pigtailed with a ~1-m long MMF).

The physical characteristics of the fabricated grating depend on both the CO_2-laser irradiation power and the exposure duration. A weak CO_2-laser dose can only cause axial residual stress relaxation around the irradiated area and hence a change in the refractive index [69]. When the laser irradiation is sufficiently intense, however, fiber deformation can occur [70]. In the present study, LPGs produced with intense CO_2-laser irradiation are investigated. Fig. 4.2(a) shows an image captured for a single period of a fabricated LPG (CO_2-laser power: 425-mw; exposure duration: 400-ms). And in Fig. 4.1(b), it is the image captured for a single period fabricated using a higher laser power (CO_2-laser power: 500-mw; exposure duration: 400-ms). As shown in Fig. 4.2(a), the fiber deformation results in a biconical taper around the exposed area, which is characterized with a taper angle θ. The fabricated LPG thus consisted of a number of equally separated tapers along the fiber. A large number of

LPGs were fabricated with different taper angles, different pitches, and different numbers of periods by controlling the CO_2-laser irradiation conditions.

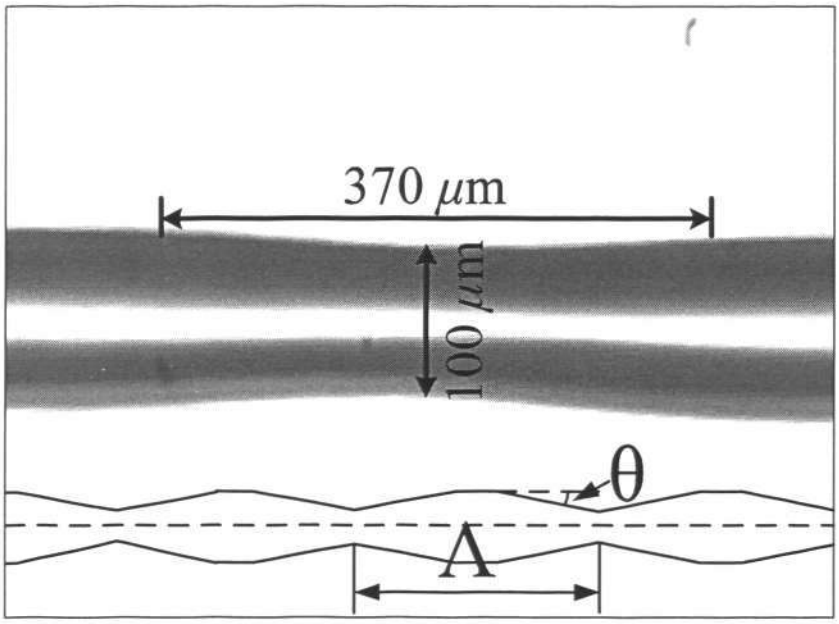

(a)

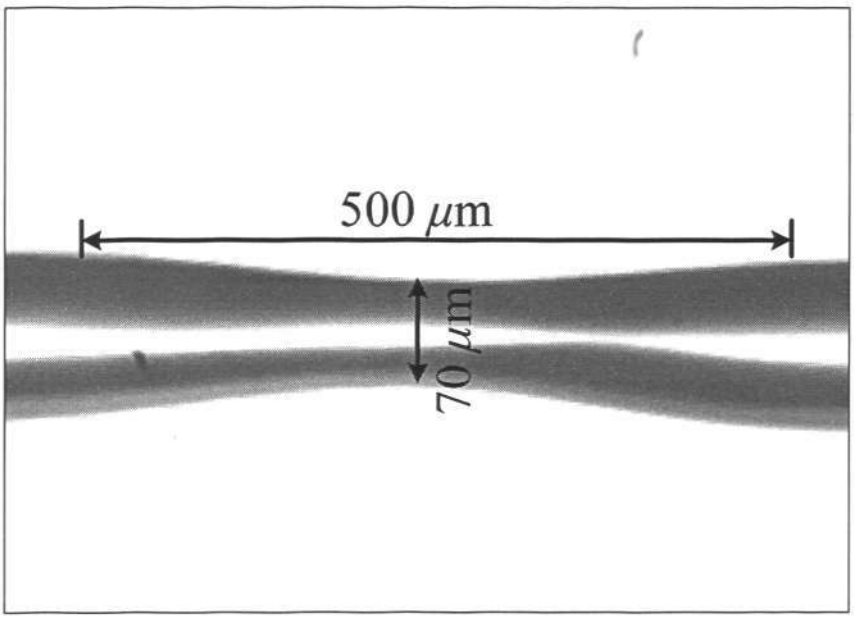

(b)

Fig. 4.2 Images of fiber tapers produced by the CO_2-laser beam and the schematic diagram defining the pitch and the taper angle of the LPG, with (a) CO_2-laser power: 425-mw; exposure duration: 400-ms, and (b) CO_2-laser power: 525-mw; exposure duration: 400-ms

4.3 Mode coupling

This section studies the co-propagating mode coupling in a multimode fiber LPG formed using CO_2 laser irradiation. The analyses presented here, however, should be applicable for an arbitrary LPG in GRIN MMF produced by either geometric deformation or index modulation. Firstly, equations for calculating coupling coefficients of the proposed LPG are derived. Secondly, the critical spatial period for co-propagating core mode coupling is found to be wavelength-independent, and is obtained based on the phase matching condition.

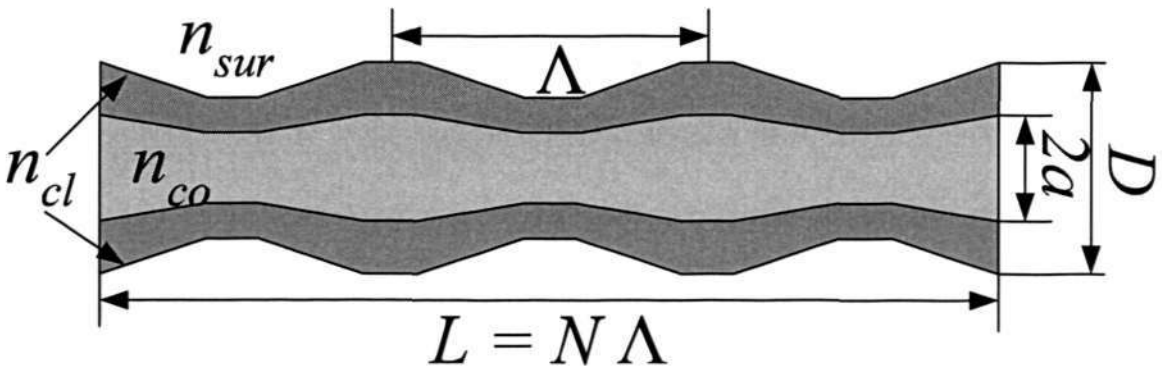

Fig. 4.3 A model for a deformed LPG in a GRIN MMF.

Fig. 4.3 shows a model of a CO_2 laser induced deformed LPG in a GRIN MMF. The MMF used here is the same fiber as that used for fabricating the MMFBG in Section 3.2 with a = 31.25 μm, n_{co} = 1.477 and n_{cl} = 1.447. D = 125 μm is the diameter of the bare fiber. n_{sur} denotes surrounding refractive index. Λ is the period of the LPG. L and N are the length and the total periods, respectively.

From the coupled mode theory [62] and the analysis made in Chapter 2, the long period grating structure (usually the period is in hundreds microns) induces the coupling between the modes propagating in the same direction (usually forward direction), which includes the coupling between core modes and the coupling between core modes and cladding modes. The coupled equation for co-propagating modes is given as

$$dc_{\mu}^{(+)} / dz = \sum_{v} K_{\mu v} c_{v}^{(+)} \exp[i(\beta_{\mu} - \beta_{v})z], \tag{4.1}$$

$$dc_{\mu}^{(-)} / dz = \sum_{v} K_{\mu v} c_{v}^{(-)} \exp[-i(\beta_{\mu} - \beta_{v})z]. \tag{4.2}$$

The coupled equation is simplified by neglecting the longitudinal coupling coefficients that are substantially smaller than the transverse coefficients. In Eqs. (4.1) and (4.2), the subscripts μ,v define the order of different modes. c is the amplitude coefficient. K is the coupling coefficient that can always be expressed as

$$K_{nm}(z) = \frac{\omega}{4} \int_{0}^{2\pi} \mathrm{d}\varphi \int_{0}^{\infty} r\mathrm{d}r \Delta p(r,z) \vec{E}_{n}(r,\varphi) \vec{E}_{m}^{*}(r,\varphi), \tag{4.3}$$

where $\Delta p(r,z)$ describes the perturbation induced by CO_2-laser-irradiation that is assumed to be independent of φ, $\vec{E}$ is the transverse components of mode fields, ω is the angular frequency of light, Symbol * denotes the conjugation operation.

The perturbation function $f(r,z)$ consists of the axial perturbation $f(z)$ and radius perturbation $f'(r)$. Therefore, Eq. (4.3) can be given as

$$K_{nm}(z) = f(z)\frac{\omega}{4}\int_0^{2\pi} \mathrm{d}\varphi \int_0^{\infty} r\mathrm{d}r f'(r) E_n(r,\varphi) E_m^*(r,\varphi)$$

$$= f(z)\cdot k\,. \tag{4.4}$$

Here the derivation follows the analysis in Chapter 2. In the case when the i^{th} mode is dominant among the incident modes to the LPG, other modes, except the i^{th} mode can be neglected on the right-hand side of Eq. (4.1). The amplitude coefficient of an arbitrary mode can be found by integrating Eq. (4.1) along z axis,

$$c_\mu(z) = c_i(0)\int_0^z kf(u)\exp[-i(\beta_i - \beta_\mu)u]du\,. \tag{4.5}$$

For the deformed LPG induced by CO_2 laser irradiation, the axial perturbation is considered to be dominated by the core-cladding deformation of the MMF. Therefore $f(z)$ is regarded as the periodic deformation on the fiber boundary along the z-axis. Then Eq. (4.5) for an L long LPG can be rewritten as

$$A_\mu(L) = LA_i(0)K_{\mu i}F(\Delta\beta_{i\mu})\,, \tag{4.6}$$

$$F(\Delta\beta_{i\mu}) = F(\beta_i - \beta_v) = L^{-1}\int_0^L f(z)\exp[-i(\beta_i - \beta_v)z]dz\,. \tag{4.7}$$

Eqs. (4.5) to (4.7) lead to two important conclusions for the CO_2-laser induced LPGs in MMF.

Firstly, the phase matching condition is derived for an LPG. In Eq. (4.7), $F(\Delta\beta_{i\mu})$ is the Fourier transform of the deformation function $f(z)$ of the LPG, which is periodically distributed along the z-axis with the spatial period Λ. Therefore the mode amplitude A in Eq. (4.7) achieves maximum when it satisfies the phase matching condition below

$$\Delta\beta = \beta_n - \beta_m = \frac{2\pi}{\Lambda}, \tag{4.8}$$

where β is the propagation constant; subscripts refer to mode orders, including both core modes and cladding modes. The phase matching condition for an MMF LPG has the same expression as the phase matching condition for LPG in SMF [18], except in an SMF LPG the coupling among the guided modes is not considered.

Secondly, the existence of the critical spatial period Λ_c is confirmed. The modal characteristics of a GRIN MMF have been reviewed in Chapter 2. For a parabolic profile, an approximation set of degeneracy exists among the propagation constants of the guided modes [42, 62]. A principal mode order m can be defined, so that the propagation constant β depends only on m. All the guided modes can then be designated according to the principal mode order (i.e., the principal modes). The total number of principal modes M is calculated [2]

$$M = \sqrt{\frac{1}{2}a^2k^2{n_{co}}^2\Delta}, \tag{4.9}$$

The propagation constant of the principal mode, β_m, is given by

$$\beta_m = n_{co}k\left[1-2\Delta(m/M)\right]^{1/2}, \tag{4.10}$$

and the propagation constant of the guided mode must lie within the limits

$$n_{cl}k < \beta_g < n_{co}k. \tag{4.11}$$

It is reasonable to assume that the core mode coupling among these principal mode groups follows the rules [42, 62]: i) the major coupling is taking place between the neighboring mode groups; ii) only the highest order core mode is coupled with the cladding modes (leaky modes).

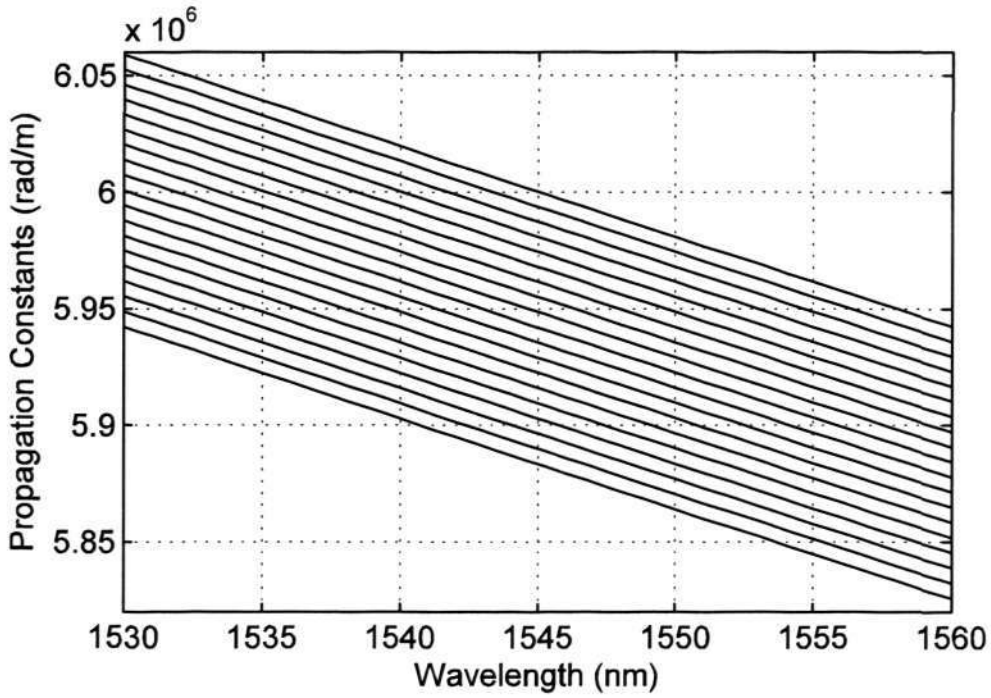

Fig. 4.4 Propagation constants of the principal modes as a function of wavelength (n = 1 to 19)

From WKB analysis [53], it is known that in a GRIN MMF all the principal modes are equally spaced in the β space. There are 19 principal guided modes guided in the applied MMF at the wavelength region of 1550nm. The propagation constants as a function of wavelength (1530nm~1560nm) are shown in Fig. 4.4. It can be seen that the propagation constants for all the guided modes are equally spaced over a wide wavelength range. By considering the phase matching condition given in Eq. (4.8), the equal spacing of all principal mode groups ensures that all principal mode groups are strongly coupled at a wavelength-independent critical grating period Λ_c, at which all the neighboring modes satisfy the phase matching condition. Λ_c can be obtained analytically as,

$$\Lambda_c = \frac{2\pi}{\Delta\beta} = \frac{2\pi a n_{co}}{\mathrm{NA}}. \tag{4.12}$$

The periodicity of the LPG can be examined by considering a sinusoidal deformation function

$$f(z) = B\sin(2\pi z/\Lambda), \tag{4.13}$$

where B is the amplitude of the deformation. Fig. 4.5 shows the normalized absolute value of the coupling coefficient between two guided modes as a function of the grating period Λ. Obviously a larger perturbation or a longer grating leads to stronger mode coupling.

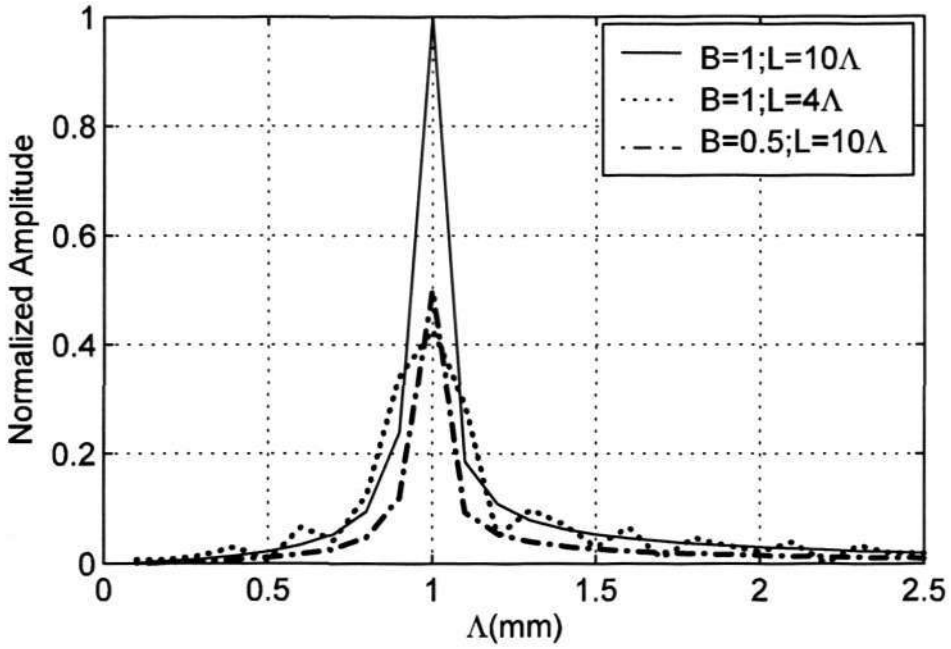

Fig. 4.5 Calculated coupling amplitudes as a function of the spatial period Λ for different deformation functions

4.4 Properties of MMF LPG

Based on the observations made on all the transmission spectra of MMF LPG samples, the theoretical analysis conducted in Section 4.3, and the results in published references, MMF LPGs are considered wavelength-independent. Therefore, all the experiments carried out for the CO_2 laser induced MMF LPGs in this thesis use C+L broadband ASE source (Photonik) owning to the wavelength-independent property.

The normalized transmission characteristics for a number of gratings with different pitches were measured and the results are presented in Fig. 4.6. All the gratings had a taper angle of 3.5° and contained 10 periods. As shown in Fig. 4.6, the

transmitted power of the LPG drops drastically at a grating pitch around 1.0 mm. As discussed in Section 4.3, in a GRIN MMF with a parabolic index profile, the core modes can be categorized as different principal mode groups according to the degeneracy of their propagation constants. Furthermore, the differences in the propagation constants between the neighboring mode groups are practically identical and wavelength-insensitive. This property of the fiber ensures the existence of a wavelength-insensitive grating pitch at which the coupling between any two neighboring mode groups is strongest. In our experiments, because the input end of the MMF was aligned with the SMF pigtail of the light source, mainly the fundamental mode of the GRIN MMF was excited. By keeping the fiber straight and free of external perturbation induced mode coupling, most of power can be guided in the fundamental modes in the fiber without being significantly coupled to other high-order modes. When the grating pitch was close to the critical spatial period of the fiber, light was coupled strongly to the high-order modes and hence the cladding modes through the grating, which represented a significant loss in the transmitted power. On the other hand, when the grating pitch was far away from the critical spatial period of the fiber, not much light was coupled to the high-order modes through the grating and most of the input light was collected at the fiber output. For our fiber with a = 31.25 μm, n_{co} = 1.477, and NA = 0.29, Λ_c is calculated to be 0.99 mm, which agrees well with the experimental value 1.0 mm.

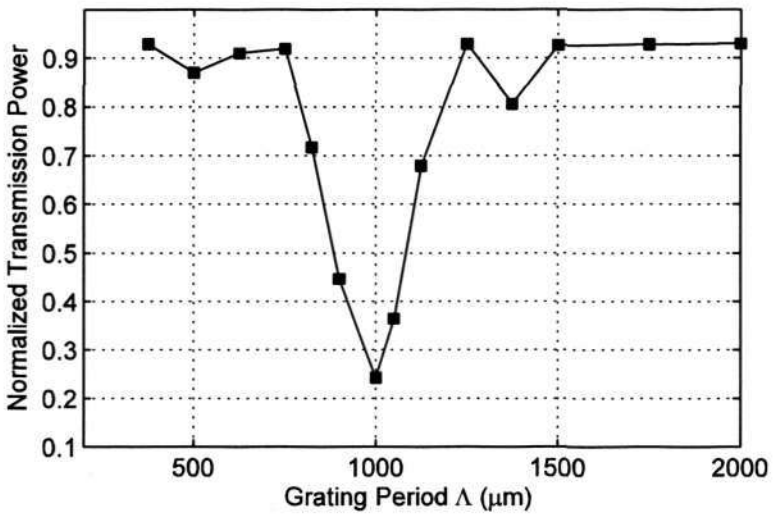

Fig. 4.6 Normalized transmission power as a function of the LPG period Λ

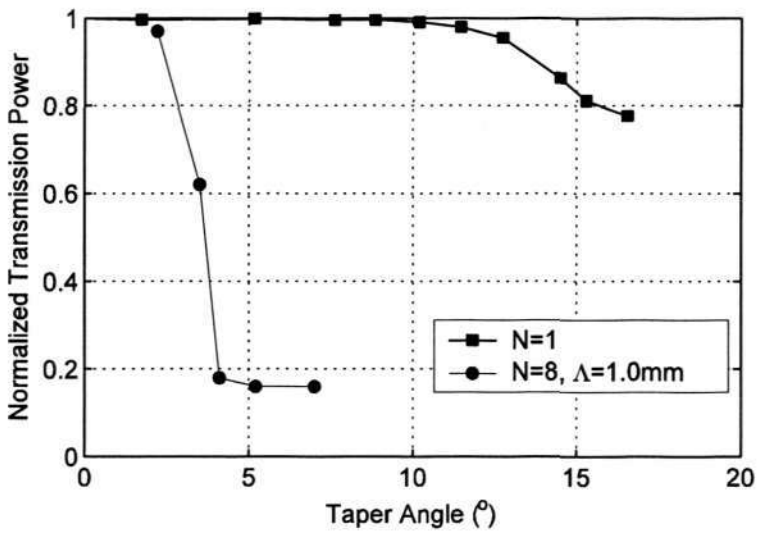

Fig. 4.7 Normalized transmission power as a function of the taper angle θ

The normalized transmission power for a number of 8-period gratings (N = 8) with different taper angles, all having the same pitch of 1.0 mm, is shown in Fig. 4.7, where the results for single tapers (N = 1) are also given for reference. For a single taper, the power loss is negligible only when the taper angle is smaller than about 10°. For the grating, however, a much smaller taper angle is sufficient to produce a significant loss.

The normalized transmission power as a function of the number of periods N is shown in Fig. 4.8. The grating pitch used is 1.0 mm and the results are presented for three taper angles 2.2°, 3.5°, and 4.1°. As shown in Fig. 4.8, when the number of periods is small, the transmission power does not drop significantly, because light is coupled mainly to low-order modes and therefore the output power is not much affected. When the number of periods increases to a certain value, significant power is coupled to the high-order modes and hence the cladding modes and therefore cannot be collected by the power meter. The transmission power thus begins to drop rapidly and finally reaches a minimum value. The rate of power drop is larger with a larger taper angle (i.e., a stronger grating). When the number of periods increases further, some cladding modes begin to couple back to the core modes in the grating and the transmission power increases. The mode coupling effects can actually be visualized from the near-field images of the fiber output depicted in Fig. 4.9. As shown in Fig. 4.9 (a), the output of the grating with $N = 1$ and $\theta = 2.2°$ contains mainly the fundamental mode. When the number of periods is increased to $N = 3$ ($\theta = 2.2°$), a superposition of the fundamental mode and the second-order mode can be seen, as shown in Fig. 4.9 (b). When the taper angle or the number of periods increases further, higher-order modes are clearly observed, as shown in Fig. 4.9 (c) and (d). The fabricated LPGs can be used as mode scramblers or mode converters.

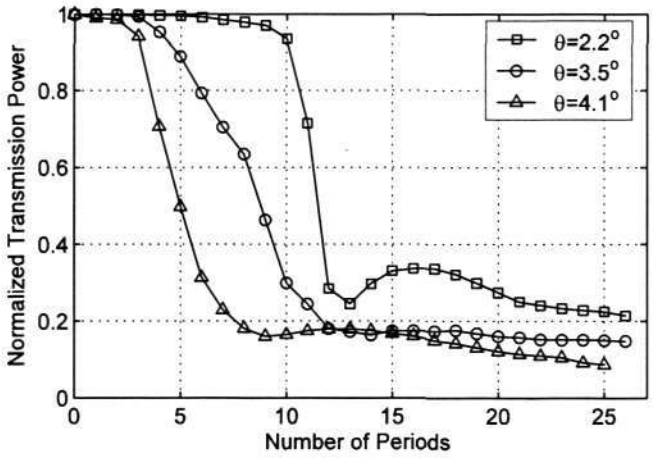

Fig. 4.8 Normalized transmission power as a function of the grating period N

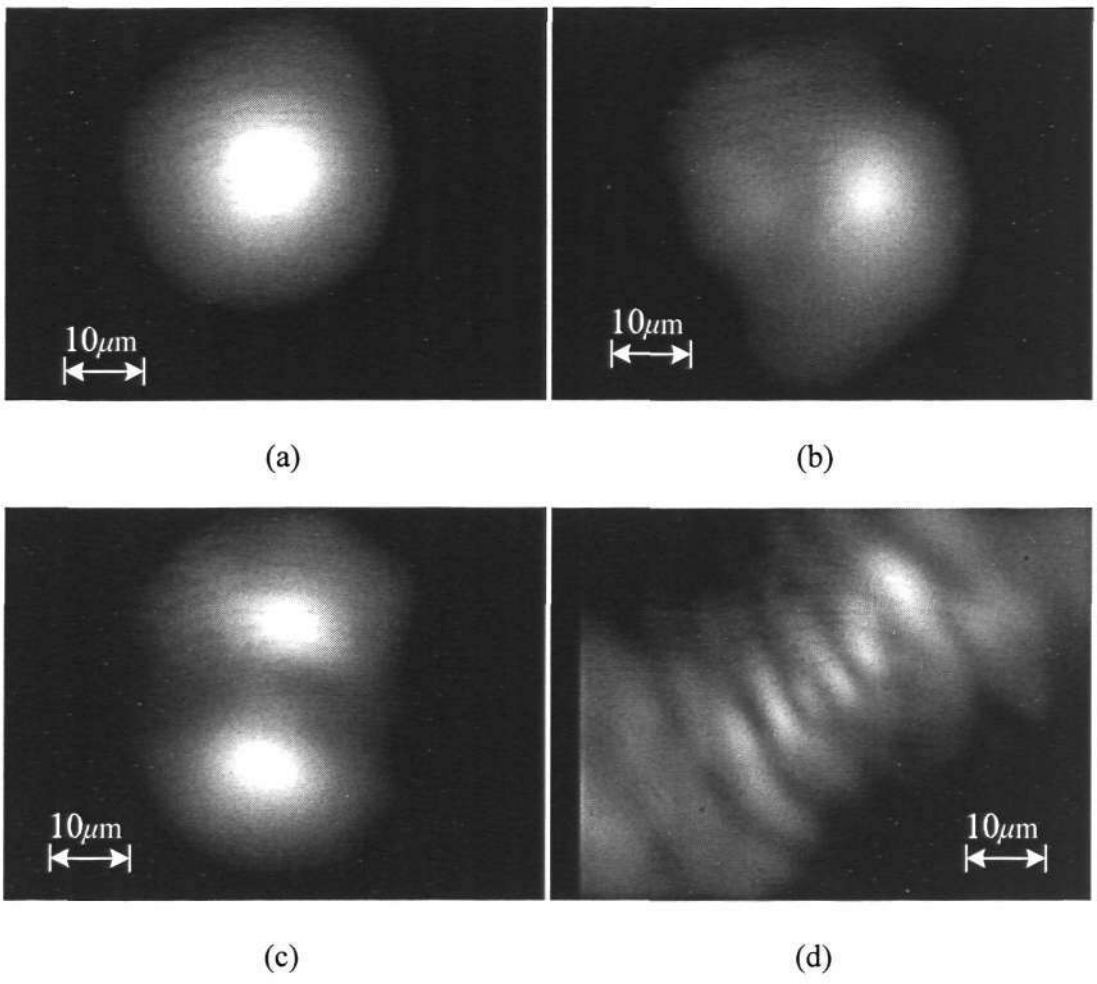

Fig. 4.9 Near field images captured at the output of LPG for: (a) $N = 1$, $\theta = 2.2^{\circ}$; (b) $N = 3$, $\theta = 2.2^{\circ}$; (c) $N = 3$, $\theta = 3.5^{\circ}$; (d) $N = 6$, $\theta = 4.1^{\circ}$.

4.5 Sensing applications of the MMF LPG

The LPG inscribed in a GRIN MMF is studied for sensing applications as: i) a strain sensor; and ii) a chemical sensor.

4.5.1 Strain sensor

4.5.1.1 Strain sensor using a single MMF taper

When a biconical fiber taper is stretched, the taper angle becomes smaller [93]. Martin *et al* proposed the application of the single MMF taper formed by fusion splicer as a strain sensor [93]. As the deformation at core-cladding boundary dominates mode coupling and determines the coupling coefficient, the applied strain on the taper will smooth the variation of core-cladding boundary deformation, which corresponds to the reduced mode coupling along the grating region, and eventually leads to the change in the light transmission characteristics.

Based on ray theory, Martin *et al* analyzed the relationship between power attenuation and strain, using the effect of the taper on the attenuation of light [93]. They assumed: 1) the angular power distribution was even; 2) the relative deformation of the core and the cladding was the same; 3) the taper had a constant angle; and 4) a step-index fiber was used. The constant taper angle θ increases the effective angle of a ray on the core and cladding interface by θ. Therefore, at the taper region, the critical

angle for a ray is given by

$$\theta_{ct} = \theta_c - \theta, \tag{4.14}$$

where θ_c is the critical angle for un-tapered region. The attenuation due to the taper was calculated as

$$A = \frac{\theta_c}{\theta_{ct}}. \tag{4.15}$$

For a taper which is subjected to a strain ε, the taper angle will change and lead to the reduction of the critical angle for the taper region. The attenuation caused by applied strain can be expressed by

$$A_\varepsilon = \frac{(90-\theta_c)-\left[\theta\left(\frac{1-\varepsilon\eta}{1+\varepsilon}\right)\right]}{(90-\theta_c)-\theta}, \tag{4.16}$$

where η is the Poisson ratio for the material.

For the fiber with NA = 0.29, n_1 = 1.477, and μ = 0.3, the responses of the single fiber taper with different taper angles are calculated and shown in Fig. 4.10, where the strain sensitivities increase with a large taper angle with linear responses.

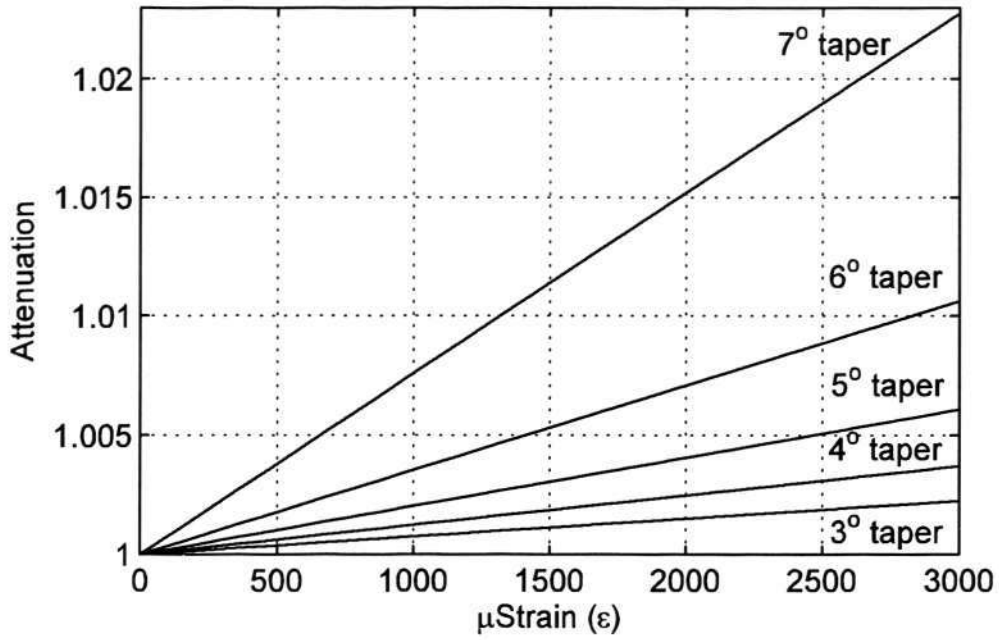

Fig. 4.10 Calculated strain responses of the single taper with different taper angles

4.5.1.2 Strain sensor using the LPG

The LPG consisting of periodic tapers in GRIN MMF is expected to be sensitive to the strain applied by considering the fact that a single taper is sensitive to strain. For a tapered LPG, the applied strain contributes to the change in the dimensions of each taper region. The configuration for measuring strain response of the proposed LPGs was shown in Fig. 4.11, and the tapered LPG was fixed to a strain-controlled stage, where the strain applied to the grating was automatically recorded. The light from a C+L broadband ASE source (Photonik) was launched via a short SMF to the LPG, and the optical power at the LPG output was detected by connecting it to a power meter (Agilent 81634B) using a ~1-m long MMF pigtail.

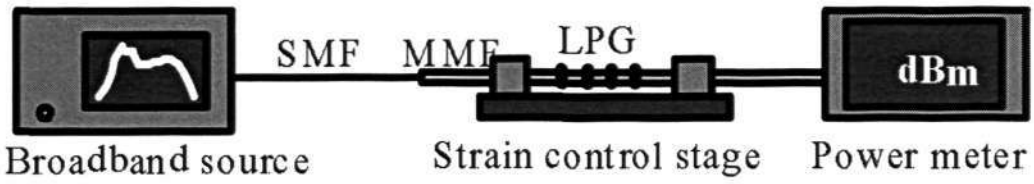

Fig. 4.11 Experimental setup for LPG strain test

Fig. 4.12 shows the measured responses of four LPGs to axial strain. Strain was applied along the grating by mounting the grating on a micro-translator. The LPGs used had the same pitch of 1.0 mm and the same taper angle of 4.1°, but different numbers of periods (N = 5, 8, 12, and 14, respectively). As expected, the transmission power increases with the applied strain and the strain sensitivity increases with the number of periods, as shown in Fig. 4.12. The measured sensitivities for the four samples in terms of the percentage change in the transmitted power can be approximated as: ~0.006%/μ-strain, ~0.014%/μ-strain, ~0.036%/μ-strain, and ~0.052%/μ-strain, respectively, which are much higher than that achieved with a single fiber taper [93]. The percentage change used in the strain sensitivity refers to the power change compared with the initial transmission power without any additional strain applied. The effects of the taper angle on the strain sensitivity are also investigated. The strain sensitivity is found to increase with the taper angle, as in the case of a single taper [93]. The strain sensitivities for the LPGs with N = 12 were measured to be ~0.002%/μ-strain, ~0.007%/μ-strain, and ~0.036%/μ-strain for θ = 2.5°, 3.5° and 4.1°, respectively. In experiments, the maximum strain that could be applied without breaking the fiber was ~3500 μ-strain. In practice, the dynamic range

of the LPG as a strain sensor can be tailored by proper packaging.

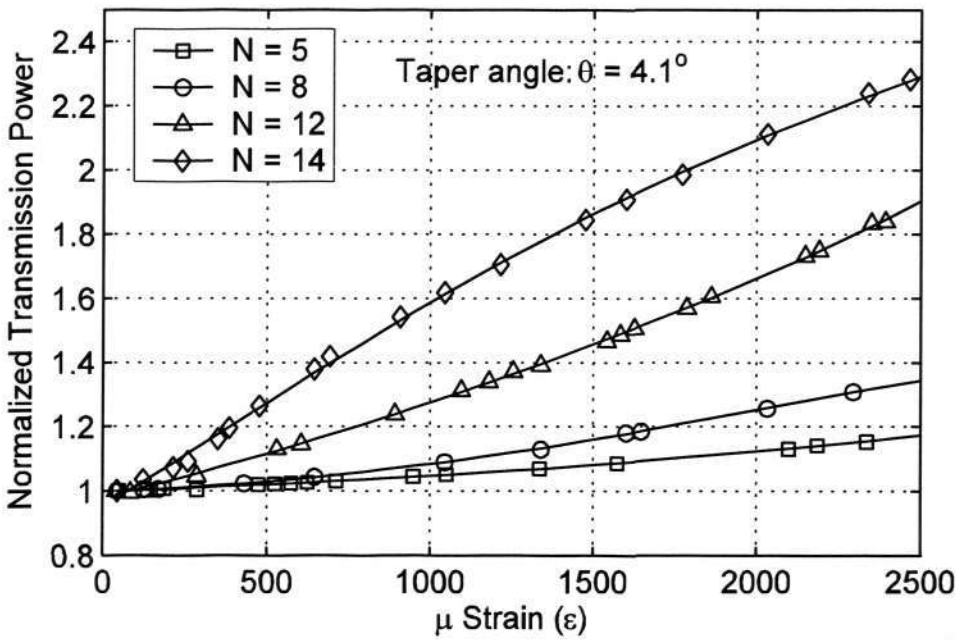

Fig. 4.12 Normalized transmission power as a function of the applied strain on the LPG

Table 4.1: Sensitivity comparison for LPG samples with different N at $\theta = 4.1°$

	N = 1	N = 5	N = 8	N = 12	N = 14
Sensitivity (%/μ-strain)	<0. 0001	~0.006	~0.014	~0.036	~0.052

Table 4.1 show a sensitivity comparison for those LPGs with different number of grating periods N but at the same taper angel 4.1°. Obviously, compared to the sensitivity of a single taper presented in [93], the strain sensitivity of our LPG is highly improved. In addition, the sensitivity increases with a larger grating period.

4.5.2 Chemical Sensor

It is known that the transmission power of an MMF taper decreases with an increase in the refractive index of the surrounding medium and this phenomenon forms the basis of a chemical sensor [94-96]. The tapering of the core in the MMF makes some of the guided modes that do not satisfy the condition of total internal reflection radiate from the core. These radiated modes may still be guided by the cladding because they may satisfy the condition of total internal reflection in the cladding-external medium interface. By enhancing the refractive index of the material that surrounds the taper region, those modes guided in the cladding can be absorbed. Therefore, the transmission characteristics of the fiber taper change.

As the proposed LPG contains many tapers, it can also serve as a chemical sensor. For a single MMF taper to offer a high enough sensitivity as a chemical sensor, the taper angle has to be large [94-96], which results in a fragile device with serious packaging problems. The proposed LPG, on the other hand, relies on resonance mode coupling and can offer a good sensitivity with a small taper angle (say, <5 °). A chemical sensor based on our LPG should be much more robust than a single MMF taper.

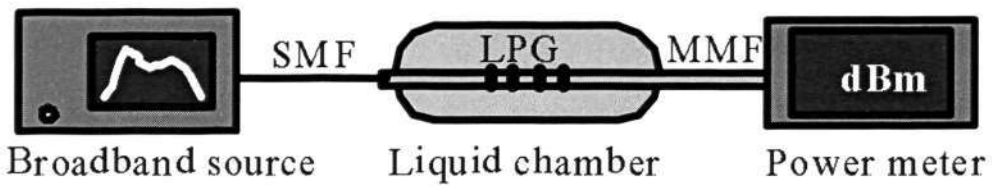

Fig. 4.13 Experimental setup for measuring chemical response of an LPG

The experiment shown in Fig. 4.13 was used to demonstrate the idea. The grating region of the LPG was carefully immersed in a liquid chamber filled with the sugar solution that has variable concentrations, since an arbitrary sugar concentration corresponds to a certain refractive index (RI) value. The light from a broadband ASE source was launched via a short SMF to the LPG, and the optical power at the LPG output was measured by connecting it to a power meter (Agilent 81634B) using a ~1-m long MMF pigtail. Fig. 4.14 shows the responses of four LPGs to a change in the sugar concentration. The gratings used had the same pitch of 1.0 mm and the same taper angle of 4.1°, but different numbers of periods (N = 5, 10, 18, and 26, respectively). As shown in Fig. 4.14, the transmission power drops as the sugar concentration (and hence the refractive index) increases and the sensitivity increases with the number of periods. With a sufficiently large number of periods, the LPG functions as an effective chemical sensor based on index change. The highest sensitivity obtained is about 3 times higher than that of the MMF LPG fabricated with a UV laser [33, 34].

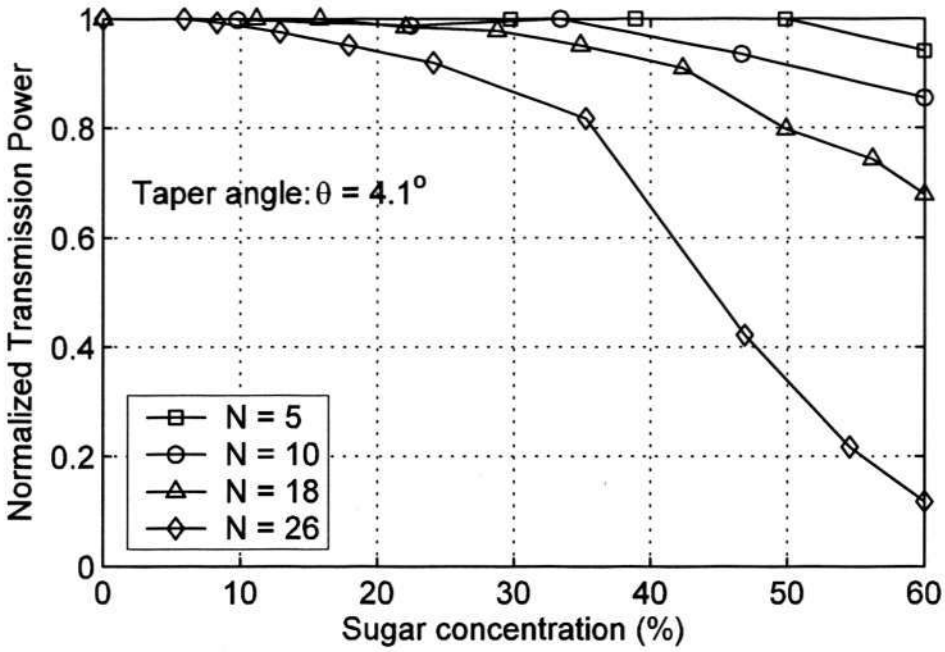

Fig. 4.14 Normalized transmission power of the LPG as a function of surrounding sugar solution concentration

The temperature sensitivities of a number of fabricated LPGs are also measured. It has been found that, for all the samples tested, the transmission power increased by less than 5% when the temperature was increased from 20 °C to 100 °C. The increase of transmission power is mainly a result of the thermal expansion of the effective area of the MMF. The weak temperature dependence of the LPGs is an advantage for the development of strain and refractive-index sensors.

In the experiments mentioned above, the resolutions of the MMF LPG based strain and chemical sensors can be as high as $\pm 25\mu$-strain for the strain measurement and $\pm 3\%$ concentration change of the sugar solution for the refractive index measurement. The resolutions achieved by the CO_2 laser induced MMF LPG sensors are lower than those reported SMF grating sensors (less than 10μ-strain for strain

sensor and less than 1% concentration change of the sugar solution for chemical sensor [84, 97]). The reason is that the CO_2 laser induced MMF LPG sensors mentioned in this chapter are based on the intensity measurement, while the SMF grating sensors monitor the wavelength shift. Nevertheless, The MMF LPG sensor proposed here is much more suitable for those applications without high requirement on resolutions, since as intensity based sensor it can be implemented much more cost-effectively. Moreover, the sensor proposed in this chapter is experimentally proved temperature-insensitive, and its performance could be improved by optimizing grating parameters and experimental conditions.

4.6 Conclusions

The study on LPG in GRIN MMF in this chapter was considered to be an important contribution of this thesis, as LPG in MMF is a new topic and detailed investigations are required on it. The LPG in MMF fabricated using focused CO_2 laser beam was proposed, which is probably the first demonstration of the CO_2-laser-induced multimode LPG. The mode coupling in a multimode LPG was studied in detail, showing the significance of the critical spatial period theoretically and experimentally. In addition, such critical period and the core mode coupling were found to be wavelength-insensitive, as all the principal modes are equally spaced in the β-space. It realized the implementation of intensity based fiber optic sensor using

the multimode fiber LPGs. The experiment explored the successful applications of the proposed LPG in both strain and chemical sensing. The multimode fiber LPG fabricated with focused CO_2 laser beam displayed high sensitivity compared with those MMF LPG induced by UV phase mask methods.

CHAPTER 5

PERIODIC MICROBEND IN GRADED-INDEX MULTIMODE FIBER

5.1 Overview

It is well known that the application of periodic microbending along an MMF can introduce significant radiation loss and mode coupling in the fiber. A number of fiber-optic sensors based on microbending loss have been developed for the measurement of pressure and displacement [38-41, 48]. In this chapter, the periodic microbend in GRIN MMF, produced by microbend deformer with a tunable coupling efficiency, is investigated. Both the microbending theory and the microbending applications are investigated. The major objectives and contributions can be given in the following two aspects.

Firstly, a theory for the microbend induced mode coupling is developed to study both the core mode coupling and the radiation loss of an MMF subjected to microbending. While there are a number of studies on the bending and microbending effects in an optical fiber (see, for example, [42-45]), such studies concern mainly the calculation of the radiation loss, i.e., the amount of power that is coupled from the

guided modes to the radiation modes. On the other hand, the coupling among the core modes induced by microbending has led to many interesting applications. For example, mode scramblers for controlling the modal distributions of MMFs based on microbend-induced mode coupling are commercially available, and a polarization converter based on periodic microbending along a birefringent fiber has also been proposed [28]. There is no any detailed report on the study of microbend-induced coupling among the guided modes, though such a study should be highly useful for the evaluation of many microbend-based devices. In this chapter, a theory to describe the microbend-induced mode coupling in a GRIN MMF is desired. Near-field patterns for a GRIN MMF subjected to microbending are presented to verify the theory. The usefulness of the theory is demonstrated to quantify the function of a mode scrambler in the form of a periodic microbend and to estimate the power response of the microbend incorporated optical fiber senor. The study focuses on a GRIN MMF with a parabolic profile for the reason that such a fiber leads to particularly simple analytical results. Such an approach, however, should apply to an arbitrary profiled MMF.

Secondly, new types of microbend sensors are investigated. As an application of the theory, an FBG incorporated microbend sensor is proposed and demonstrated to simultaneously measure a mechanical parameter and environment temperature. The conventional microbend sensors use a single multimode fiber as both the sensor lead and the sensing element and, therefore, may suffer from instability caused by the

fluctuations in the modal distribution in the fiber lead. The problem is solved by using single-mode fibers as the input and output leads of the sensor [48]. While the use of single-mode fiber leads reduces unavoidably the output power of the sensor, it can provide higher sensitivity [48]. So far all the microbend sensors are designed based on the measurement of mechanical parameters, such as pressure and displacement. Here a simple microbend sensor is presented, allowing simultaneous measurement of both a mechanical parameter and temperature. The proposed sensor consists of a single-mode fiber lead connected to a short multimode fiber. Microbending is applied to the multimode fiber for mechanical-parameter sensing. The novel aspect of the sensor is that the multimode fiber is connected to a single-mode FBG at the other end. The grating turns the microbend sensor into a reflection-type sensor and the shift in the reflected wavelength serves as a measure of the temperature. In practice, the multimode fiber and the FBG can be packaged together to form a compact sensor head. Two configurations to operate the sensor, using a broadband source and a tunable laser respectively, are demonstrated experimentally.

5.2 Periodicity of GRIN MMF

In Chapter 3, the critical spatial period was derived for the long period grating where the co-propagating mode coupling dominates. It is well known that the microbend induces the mode coupling between modes with different orders propagating in the same direction. Therefore the critical spatial period given in Eq. (4.12) is also

applicable to the microbend induced mode coupling. For the GRIN MMF with a = 31.25 μm, n_{co} = 1.477, and NA = 0.29, Λ_c is calculated to be 0.99 mm.

Microbending loss is the very phenomenon that allows the microbend sensors to work. The microbending loss is caused by coupling of guided modes to cladding modes. For small changes in the fiber deformation where neighboring mode coupling is valid, only adjacent modes are coupled. In this case, microbending loss is due to coupling from the highest order guided mode to the cladding modes. The strong coupling is realized with the calculated spatial periodicity of the fiber. Such a periodicity is expected to enhance significantly microbending loss, and therefore the sensitivities of the microbend sensors. The existence of critical spatial period of microbend sensors has been verified in many literatures [39]. In addition, the experiment conducted in Chapter 4 for the multimode fiber LPGs with different period confirmed the spatial periodicity of the GRIN MMF applied.

In this chapter, the period of the microbending deformer is fixed at its critical value (1-mm) in order to achieve the most strongly mode coupling.

5.3 Theory of microbend-induced mode coupling

In this section, a theory is developed to study not only the radiation loss produced by microbending but also the characteristics of the mode coupling at the microbend.

Consider a straight GRIN MMF with a parabolic profile in the x-y transverse plane. Light propagates along the fiber in the z direction. The refractive-index difference between the core and the cladding is assumed small so that the modes in the fiber satisfy the scalar wave equation. The electric field for a given mode in the fiber can be written in Cartesian coordinates as [43-45]

$$U_m(x,y,z) = a_m u_m(x,y)\exp(i\omega t - i\beta_m z), \tag{5.1}$$

where ω is the angular frequency of the light, m is an integer (1, 2, 3, …) labeling the modes (i.e., a mode order), a_m and β_m are the amplitude and the propagation constant of the mode, and $u_m(x,y)$ is the normalized mode field. Mode fields of different orders are orthogonal to each other in the following sense:

$$\int_{-\infty}^{+\infty}\int_{-\infty}^{+\infty} u_k \cdot u_m^* dxdy = \begin{cases} 0, & k \neq m \\ 1, & k = m \end{cases}. \tag{5.2}$$

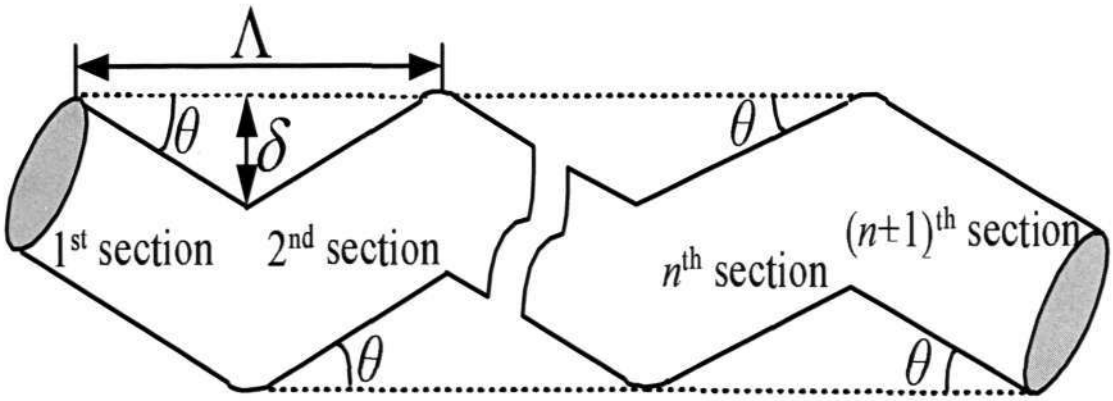

(a)

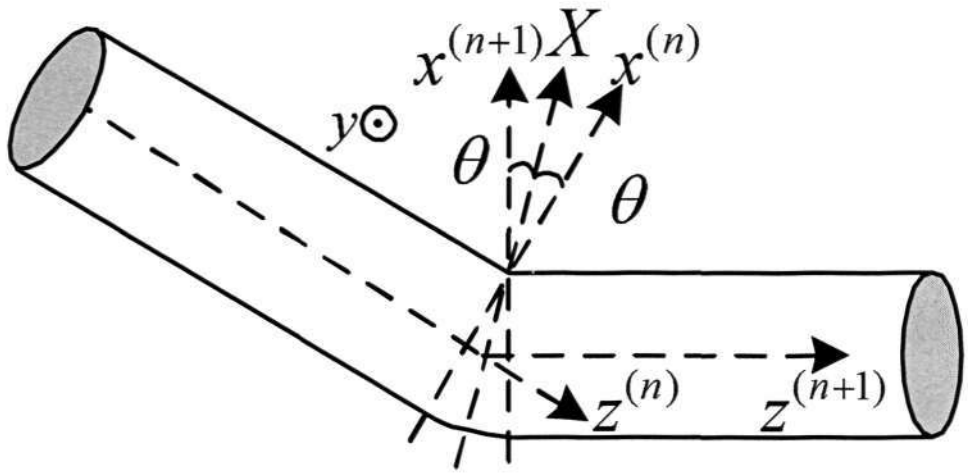

(b)

Fig. 5.1 (a) A periodic microbend with a pitch Λ and a microbending angle θ (b) Model of a single microbend showing the local coordinate systems

Produced by the microbending deformer introduced in Section 2.7.3, the model for a periodic microbend is shown in Fig. 5.1(a), where Λ is the pitch, θ is the bending angle, and δ is the microbending displacement which is given by $\tan\theta = 2\delta/\Lambda$ in the model. The periodic microbend can be divided into $n + 1$ identical microbends arranged in a zigzag manner. The model for a single microbend is shown in Fig. 5.1 (b), which follows that used in [45]. As the microbend-induced change in the

refractive index in the fiber is small, any reflected power at the microbend is neglected. With reference to Fig. 5.1(b), two local coordinate systems, $(x^{(n)}, y, z^{(n)})$ and $(x^{(n+1)}, y, z^{(n+1)})$, are used for the straight sections before the bend and after the bend, respectively (noted that they possess the same y-axis). The coordinates are matched along the X-plane according to the following relations:

$$x^{(n)} = x^{(n+1)} = X\cos\theta\,, \tag{5.3}$$

$$z^{(n)} = -X\sin\theta\,, \tag{5.4}$$

$$z^{(n+1)} = X\sin\theta\,. \tag{5.5}$$

Two types of mode coupling occur at a microbend: the coupling from the guided modes to the cladding modes and the coupling among the guided modes. In the present study, we ignore the coupling to the radiation modes and consider only the coupling among the guided modes, as the latter case has not been studied in detail previously. With reference to Fig. 5.1(b), as the electric field must be continuous across the X-plane, we have

$$U^{(n)}(X\cos\theta, y, -X\sin\theta) = U^{(n+1)}(X\cos\theta, y, X\sin\theta)\,. \tag{5.6}$$

Assuming N guided modes in the fiber, Eq. (5.6) can be written as

$$\sum_{m=1}^{N} a_m^{(n)} u_m(X\cos\theta, y)\exp(i\omega t + i\beta_m X\sin\theta)\,,$$

$$= \sum_{k=1}^{N} a_k^{(n+1)} u_k(X\cos\theta, y)\exp(i\omega t - i\beta_k X\sin\theta)\,. \tag{5.7}$$

The assumption that the radiation modes are negligible affects the accuracy of the analysis only for guided modes of very high orders, since only these modes can couple significantly to the radiation modes. Multiplying both sides of Eq. (5.7) by $u_k^*(X\cos\theta, y)\exp(-i\omega t + i\beta_k X\sin\theta)$ and integrating the resultant equation over the x-y plane, we obtain

$$a_k^{(n+1)} = \sum_{m=1}^{N} a_m^{(n)} \iint u_m(x,y)u_k^*(x,y)\exp(i\gamma_{m,k}x)dxdy\,, \tag{5.8}$$

where

$$\gamma_{m,k} = (\beta_m + \beta_k)\cdot\tan\theta\,. \tag{5.9}$$

According to Eq. (5.8), the coupling coefficient $c_{m,k}$ from the m^{th} mode to the k^{th} mode is given by

$$c_{m,k} = \iint u_m(x,y)u_k^*(x,y)\exp(i\gamma_{m,k}x)dxdy\,. \tag{5.10}$$

A matrix can be defined for the coupling coefficients between all the guided modes as

$$M_{n+1}(\theta) = \begin{bmatrix} c_{00} & c_{01} & \cdots & c_{0,N-1} \\ c_{10} & c_{11} & \cdots & c_{1,N-1} \\ \cdots & \cdots & \cdots & \cdots \\ c_{N-1,0} & c_{N-1,1} & \cdots & c_{N-1,N-1} \end{bmatrix}. \tag{5.11}$$

The amplitudes of all the guided modes in the section after the bend, $A^{(n+1)}$, can thus be calculated from the incident amplitudes of the guided modes before the bend, $A^{(n)}$, through the coupling-coefficient matrix $M_{n+1}(\theta)$:

$$A^{(n+1)} = M_{n+1}(\theta)A^{(n)}, \tag{5.12}$$

where $A^{(j)} = [a_0{}^{(j)}, a_1{}^{(j)}, \ldots, a_{N-1}{}^{(j)}]^T$ with $j = n, n + 1$. For the periodic micorbend shown in Fig. 5.1(a), the output amplitude vector $A^{(n+1)}$ can be obtained from the input amplitude vector $A^{(0)}$ by simply multiplying the coupling-coefficients matrices of all microbends:

$$A^{(n+1)} = M_{n+1}(\theta)M_n(\theta)\cdots M_2(\theta)M_1(\theta)A^{(0)}. \tag{5.13}$$

It should be noted that the coupling-coefficient matrix $M_n(\theta)$ depends on θ only. It can be seen from Eq. (5.10) that $c_{m,k} = c_{k,m}$, so $M_n(\theta)$ is a symmetric matrix. To evaluate $M_n(\theta)$ from Eq. (5.10), It is necessary to know the mode fields in the fiber. As discussed in Chapter 2, the modes in a GRIN MMF can be designated as the Hermite-Gaussian modes, which are a family of solutions of the scalar wave equation in the Cartesian coordinates, expressed in terms of Hermite polynomials multiplied by a Gaussian envelope and categorized by two mode orders p and q ($p, q, = 0, 1, 2, \ldots$)

[57, 60, 61]. The field of the Hermite-Gaussian mode, denoted as the HG_{pq} mode, is given by [57]

$$\psi_{pq}(x,y,z) = [\omega_0^2 \pi 2^{(p+q-1)} p!q!]^{-1/2} H_p\left(\frac{\sqrt{2}x}{\omega_0}\right) H_q\left(\frac{\sqrt{2}y}{\omega_0}\right)$$

$$\cdot \exp[-(x^2+y^2)/\omega_0^2] \exp(-i\beta_{p,q} z), \tag{5.14}$$

where $\beta_{p,q}$ is the propagation constant and $H_p(x)$ is the p^{th}-order Hermite polynomial. ω_0 is the characteristic spot radius of the parabolic profile:

$$\omega_0 = \sqrt{2a/[kn_{co}(2\Delta)^{1/2}]}, \tag{5.15}$$

where $k = 2\pi/\lambda$ is the propagation vector in the free space, a is the core radius of the fiber, Δ is the index difference, and n_{co} is the core index.

Considering the concept of principal mode groups given in Chapter 2, we have the total number of principal mode groups

$$M = \sqrt{N} = \sqrt{\frac{1}{2} a^2 k^2 n_{co}^2 \Delta}. \tag{5.16}$$

and the propagation constant of the principal mode, β_m, is given by

$$\beta_m = n_{co} k [1 - 2\Delta(m/M)]^{1/2}. \tag{5.17}$$

Using the principal mode order, the mode field $u_m(x,y)$ is given by

$$u_m(x,y) = [\omega_0^2 \pi 2^{(p+q-1)} p!q!]^{-1/2} H_p\left(\frac{\sqrt{2}x}{\omega_0}\right) H_q\left(\frac{\sqrt{2}y}{\omega_0}\right) \cdot \exp[-(x^2+y^2)/\omega_0^2]. \tag{5.18}$$

With the help of the Gaussian-Hermite modes, the coupling coefficients and hence the amplitudes of the coupled modes, $A^{(n+1)}$, can be evaluated.

The total power carried by the guided modes in a section of the fiber is given by $P_g^{(n)}$, where

$$P_g^{(n)} = (A^{(n)}) \cdot \left[(A^{(n)})^* \right]^T = \left| a_0^{(n)} \right|^2 + \left| a_1^{(n)} \right|^2 + \ldots + \left| a_{N-1}^{(n)} \right|^2 . \tag{5.19}$$

The power loss at a particular micorbend is thus given by $P_g^{(n)} - P_g^{(n+1)}$ and the total power loss through $n + 1$ microbends, i.e., the periodic microbend, is $P_g^{(0)} - P_g^{(n+1)}$.

The standard GRIN MMF previous mentioned is also employed here, having the following parameters: overall diameter d = 62.5 μm, core index n_{co} = 1.477, and cladding index n_{cl} = 1.447. The operating wavelength is fixed at λ = 1550 nm. This fiber supports 19 principal modes.

Firstly, the simplest case is considered, i.e., mode coupling at a single microbend. It is assumed that light is linearly polarized in the x-direction and the input light

contains only the HG_{00} mode. In other words, the input mode distribution in the fiber is given by

$$A^{(0)} = [1, \quad 0, \quad ..., \quad 0]^{T}. \tag{5.20}$$

The mode distribution after a single microbend is then obtained as

$$A^{(1)} = M(\theta) \cdot A^{(0)} = [c_{0,0} \quad c_{0,1} \quad ... \quad c_{0,M-1}]^{T}, \tag{5.21}$$

where $c_{0,k}$ is the coupling coefficient between the fundamental mode (the HG_{00} mode) and the k^{th}-order mode as given by Eq. (5.10). By substituting the fields of the HG_{00} mode and the HG_{pq} mode into Eq. (5.10), we obtain

$$c_{0,k} = \frac{2}{\omega_0^{\,2}\pi}[2^{(p+q)}\, p!q!]^{-1/2} \int H_p\left(\frac{\sqrt{2}x}{\omega_0}\right)\exp(-\frac{2x^2}{\omega_0^{\,2}} + i\gamma_{0,k}x)dx$$

$$\cdot \int H_q\left(\frac{\sqrt{2}y}{\omega_0}\right)\exp(-\frac{2y^2}{\omega_0^{\,2}})dy, \tag{5.22}$$

where $k = p + q + 1$. It should be noted that the coupling coefficient $c_{0,k}$ has a none-zero value only when $q = 0$, since the microbending has no effect in the y direction. Therefore, when only the HG_{00} mode is launched into the microbend, only the HG_{p0} modes are excited. By solving (5.22) analytically, it yields

$$c_{0,k} = (2^{p} \cdot p!)^{-\frac{1}{2}}(i \cdot \gamma)^{p} \exp(-\frac{\gamma^2}{4}). \tag{5.23}$$

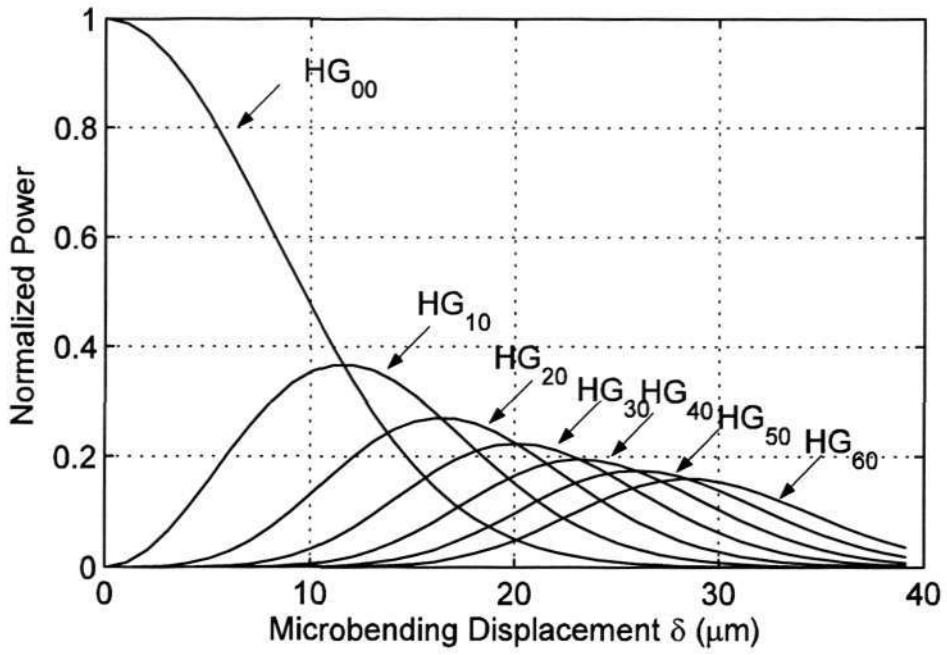

(a)

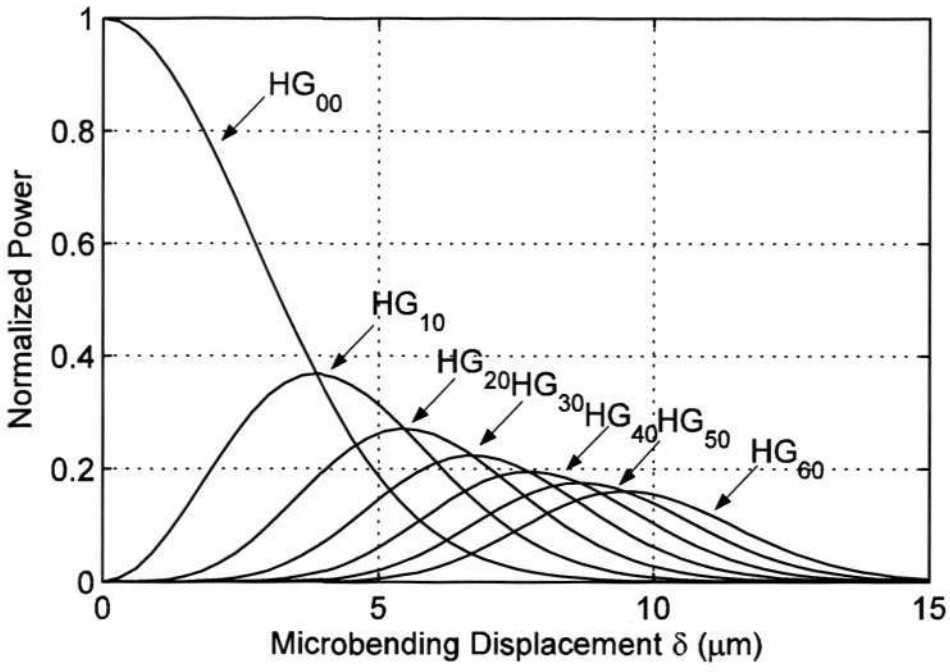

(b)

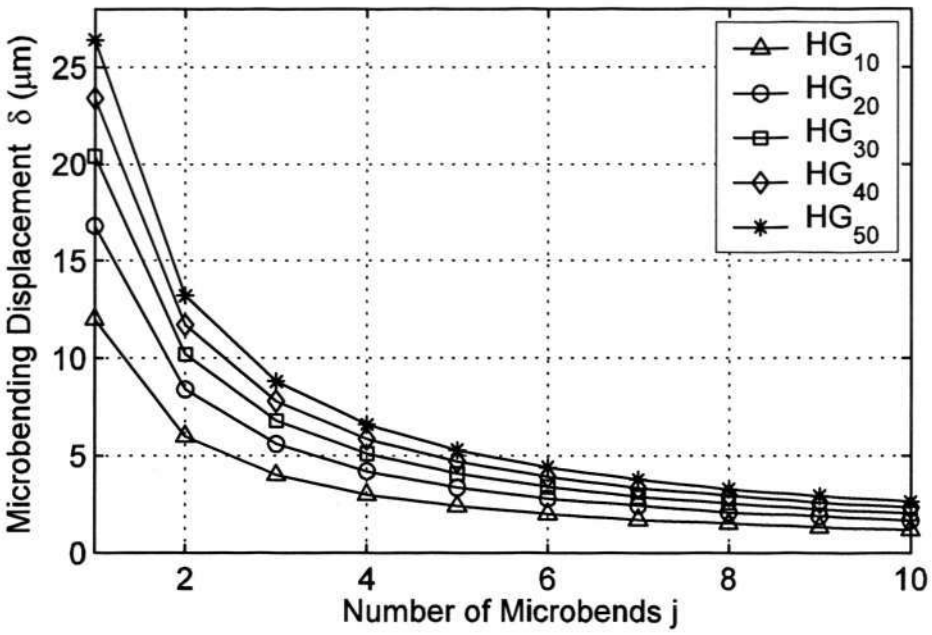

(c)

Fig. 5.2 Dependence of the normalized modal power on the microbending displacement δ for (a) a single microbend and (b) a three-tooth microbend deformer with a pitch of 1 mm, when the input light contains only the HG_{00} mode, and (c) dependence of the microbending displacement δ required for dominantly coupling to a particular mode on the number of microbends

Fig. 5.2(a) shows the mode coupling coefficients versus the microbending displacement δ at a single bend for a number of low-order modes. As the value of δ increases, the coupling to a particular high-order HG_{p0} mode first increases and then decreases after reaching a maximum. This suggests that at a certain microbending angle, the HG_{00} mode is most effectively coupled to a specific high-order mode. In other words, the high-order modes are progressively selected to be coupled strongly as the amount of microbending increases continuously. Fig. 5.2(b) shows the mode coupling situation at the output of a microbending deformer that consists of three microbends with a pitch of 1 mm, where only the HG_{00} mode is launched into the

device. The 1-mm pitch corresponds to the critical spatial period of the MMF for the achievement of strongest mode couplings. The results in (b) are similar to those in Fig. Fig. 5.2(a), except that in the case of three microbends a smaller microbending displacement is required for dominantly coupling to the high-order mode. For example, in the case of a single microbend, the HG_{00} mode is most effectively coupled to the HG_{10} mode at δ = 12 μm as shown in Fig. 5.2 (a), while in the case of three microbends, this occurs at δ = 4 μm, i.e., the value of δ required is three times smaller, as shown in Fig. 5.2 (b). In fact, the value of δ required for dominantly coupling to a particular mode is found to be inversely proportional to the number of microbends, as shown in Fig. 5.2 (c). In other words, the value of δ required with j microbends is equal to the value of δ required with a single microbend divided by j.

The calculation is repeated by assuming that only the HG_{30} mode is launched into a single microbend. The results are shown in Fig. 5.3. It can be seen that the coupling efficiency to the HG_{00} mode in Fig. 5.3 is the same as that to the HG_{30} mode in Fig. 5.2 (a) at the same micobending displacement, as expected from the symmetry property of the coupling coefficients, i.e., $c_{0,3} = c_{3,0}$.

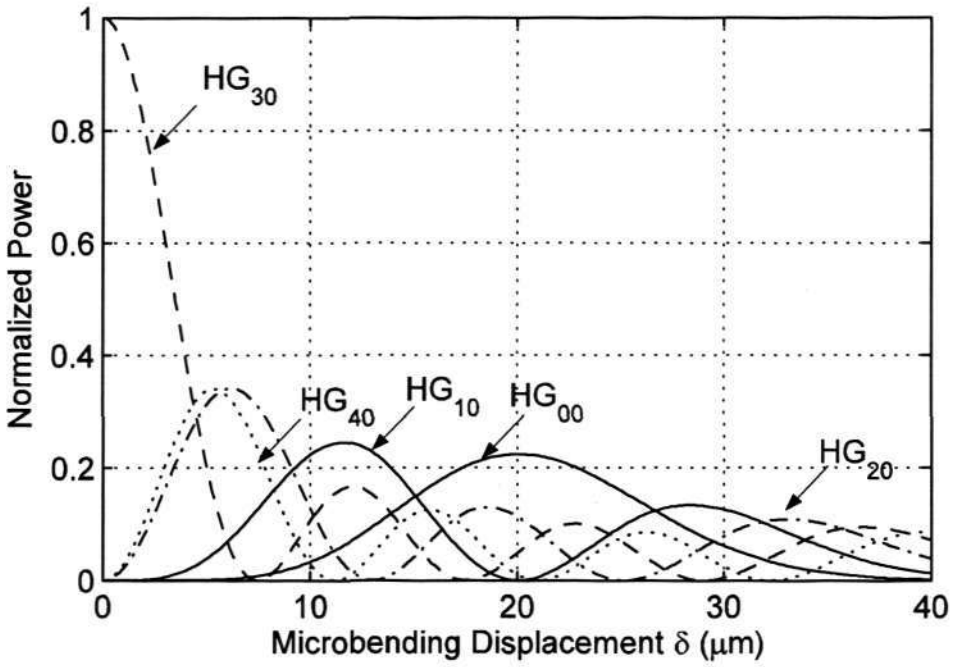

Fig. 5.3 Dependence of the normalized modal power on the microbending displacement δ for a single microbend, when the input light contains only the HG_{30} mode

In Fig. 5.2, when only the fundamental mode is launched to the input of periodic microbend, modes with different orders can be dominant (having the highest power among all the modes) at different microbending displacement values. Fig. 5.4 shows the calculated preferentially excited mode as a function of microbending displacement for different number of bends. It can be seen that the order of preferentially excited mode rises up with the increase of the microbending displacement for the microbend deformer with 1, 2 and 3 bends.

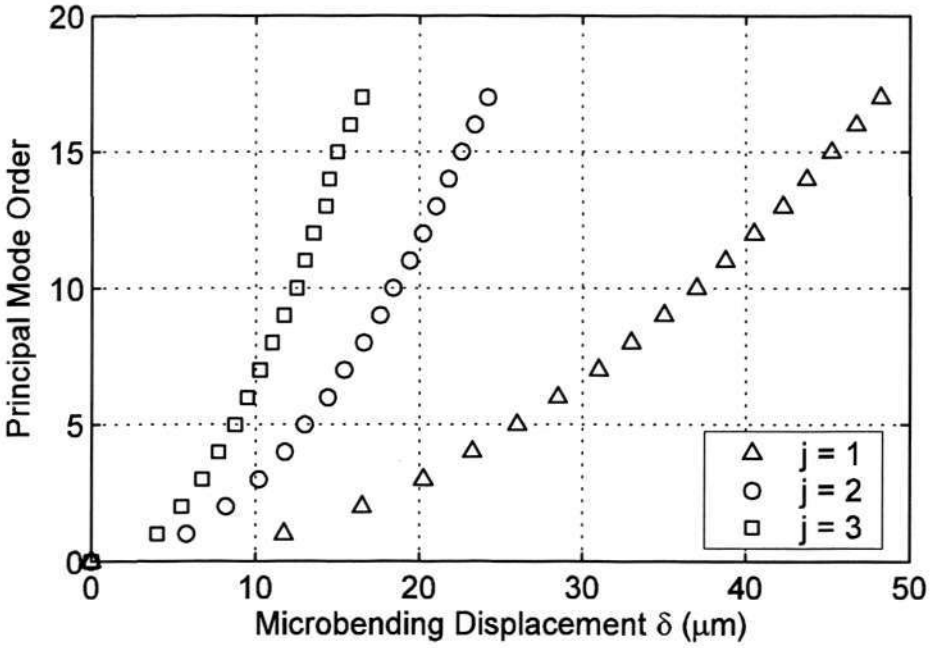

Fig. 5.4 Preferentially excited mode as a function of the microbending displacement at different number of microbends *j*

For simplicity, a bare glass fiber is assumed in calculations. When microbending is applied to a coated fiber, because the coating material is softer than glass, the microbending displacement measured for the coated fiber should be larger than that experienced by the glass fiber. To quantify the effects of the coating, a detailed stress analysis of the coated fiber is required, which is saved as a future work of the present study. It can be simplified, however, that the microbending displacement of the coated fiber is larger than that of the glass fiber by a constant factor that depends on the thickness and the elastic properties of the coating material.

5.4 Mode scrambler based on periodic microbend

As an application of the theory developed in section 5.3, a mode scrambler can be modeled as a periodic microbend. Mode scrambler is the device applied to multimode optical fiber to induce mode coupling and eventually lead to a stable mode power distribution. Periodic microbend has been effectively implemented for the design of the mode scrambler. Such products are commercially available in the market.

Here a periodic microbend with a tooth pitch of Λ = 1 mm considered, as shown in Fig 5.1(a). The input modal distribution $A^{(0)}$ is given by Eq. (5.20), i.e., only the HG_{00} mode is launched into the periodic microbend.

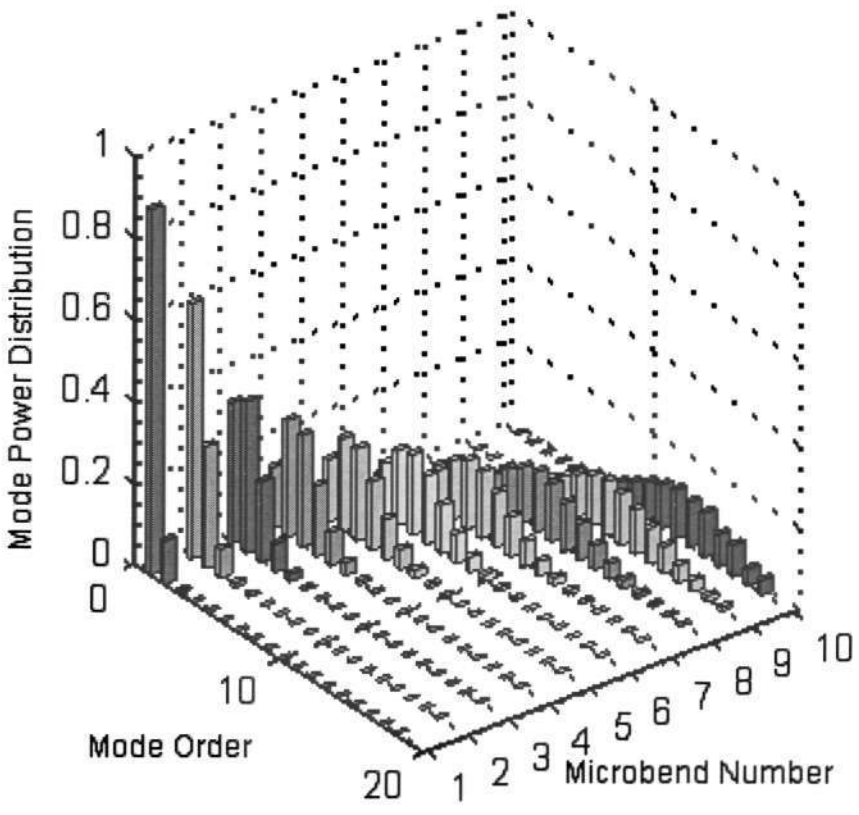

(a)

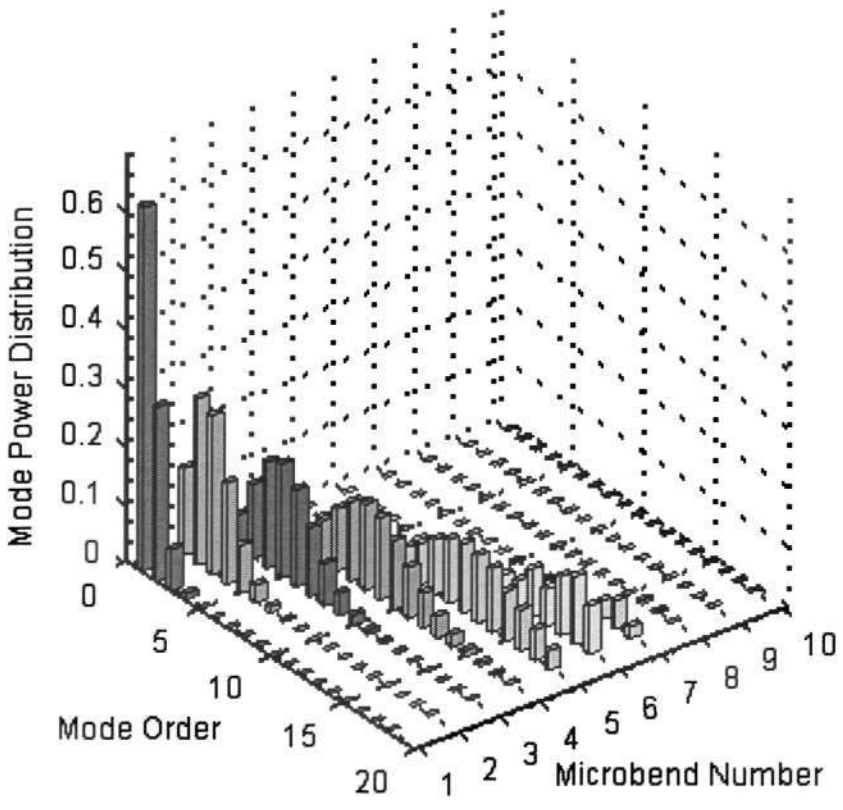

(b)

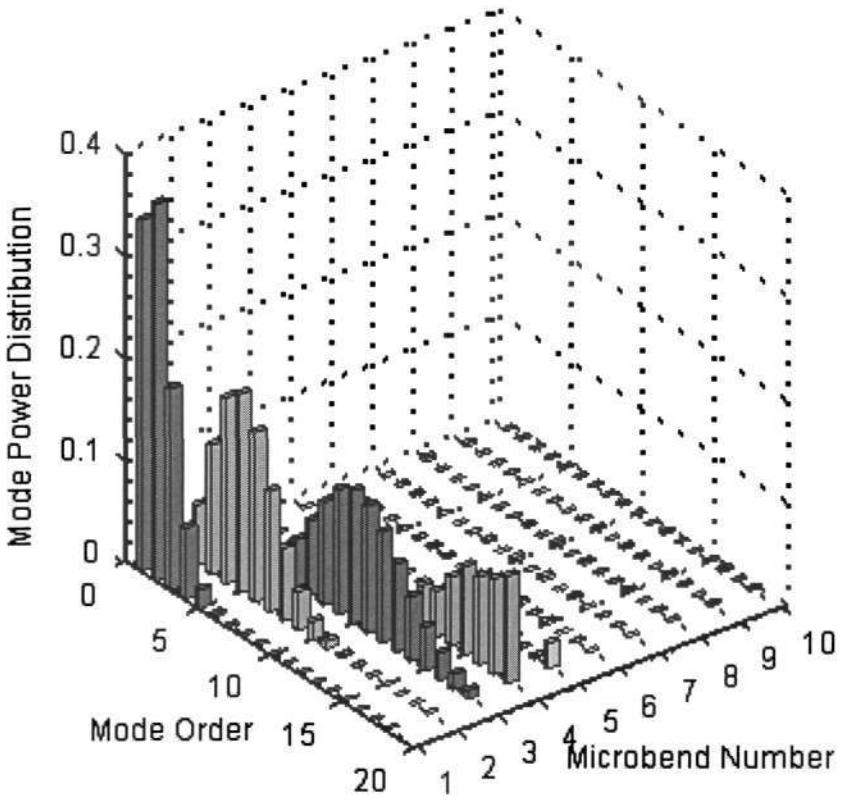

(c)

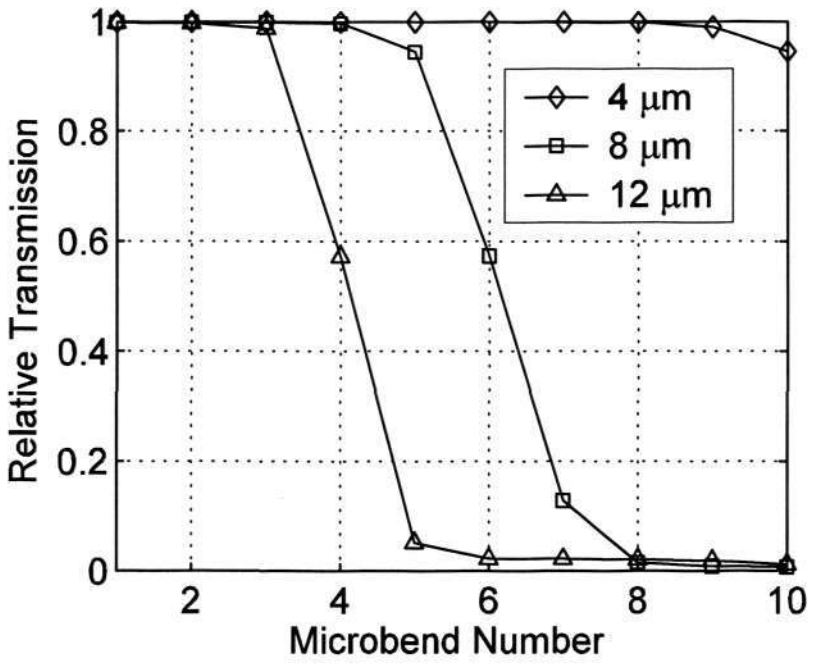

(d)

Fig. 5.5 Variation of the modal power distribution with the number of microbends for (a) $\delta = 4\ \mu$m, (b) $\delta = 8\ \mu$m, and (c) $\delta = 12\ \mu$m, and (d) the corresponding power losses

The modal power distributions after each microbend for the first 10 microbends are shown in Fig. 5.5(a) – (c) for three values of the microbending displacement, 4 μm, 8 μm, and 12 μm. The corresponding power losses are shown in Fig. 5.5(d). Fig. 5.5(a) – (c) show clearly how the optical power is distributed to the high-order modes as the number of microbends increases. When a larger amount of microbending is used, the optical power is distributed effectively to the high-order modes with a less number of microbends, but, as shown in Fig. 5.5(d), the power loss also increases quickly. In any case, as the number of microbends is large enough, the optical power tends to be distributed smoothly among the modes with higher powers in lower-order modes. In other words, the resultant power distribution resembles the equilibrium modal

distribution that would have been produced with a long MMF. This is exactly the function of a mode scrambler. This is believed to be the first quantitative analysis of a microbend-based mode scrambler. The microbend theory developed here should be useful for the design of this type of mode scramblers.

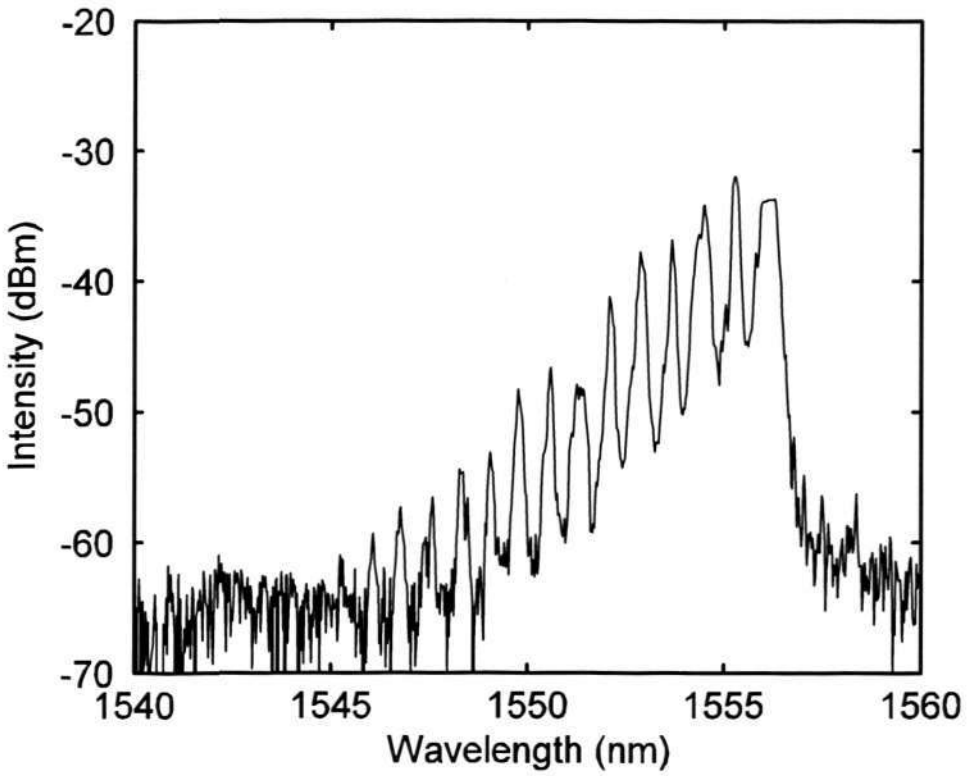

(a)

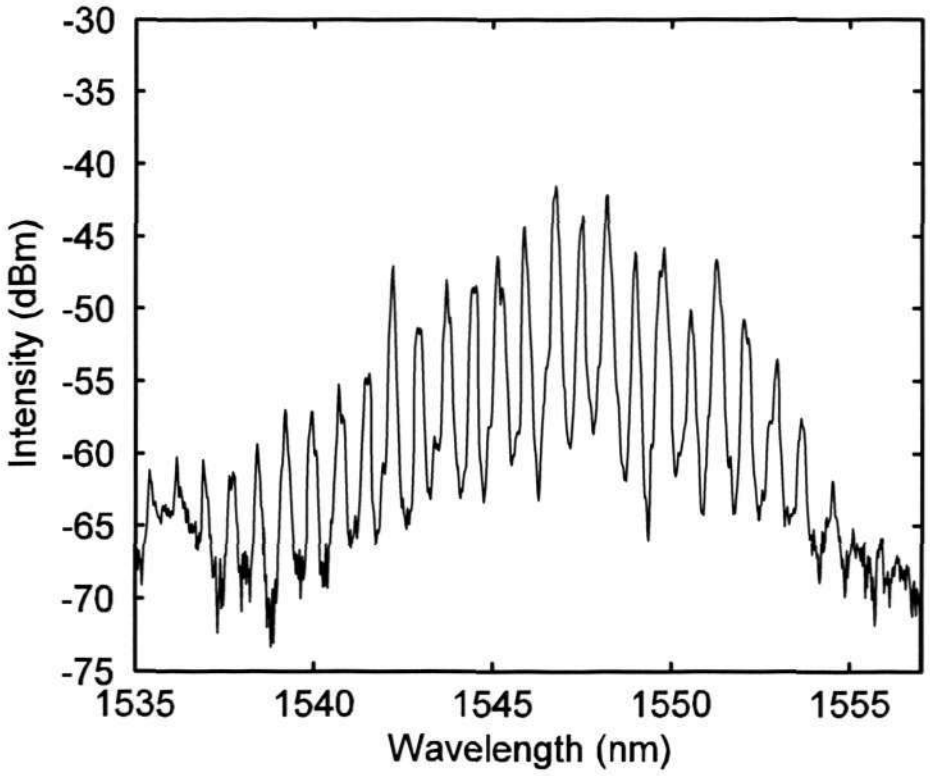

(b)

Fig. 5.6 Observation of the mode coupling induced by a periodic microbending with the assistance of an MMFBG for (a) $\delta = 10\ \mu$m, and (b) $\delta = 26\ \mu$m

To confirm the analysis experimentally, the reflection spectra of a multimode fiber Bragg grating (MMFBG) were employed, as MMFBG spectra are indeed the signatures for the modal power distributions. The light reflected from the GRIN MMF subject to microbending (using the three-bend deformer) was measured by introducing an FBG at the other end of the fiber. Only the fundamental mode was launched into the fiber preferentially. The reflection spectra measured at two microbending displacement values, 10 μm, 26 μm, are given in Fig. 5.6. Distinct peaks corresponding to different principal modes are seen in each reflection spectrum

[32], which is in fact a signature of the modal distribution in the fiber under the given microbending condition. The reflection spectra show clearly how the dominant coupled mode evolves with the microbending displacement. For the two microbending displacement values, the HG_{10} and HG_{60} modes are, respectively, the preferentially coupled modes, in agreement with the near-field measurements and the theoretical predictions. The mode scrambling effect is also seen clearly from the reflection spectra. As the microbending displacement increases, the power distribution among the modes becomes more and more even, just as the simulation results in Fig. 5.5 (a) – (c) predict. The reflection spectrum of a multimode FBG serves as an effective means for characterizing the performance of a mode scrambler.

5.5 Near field images

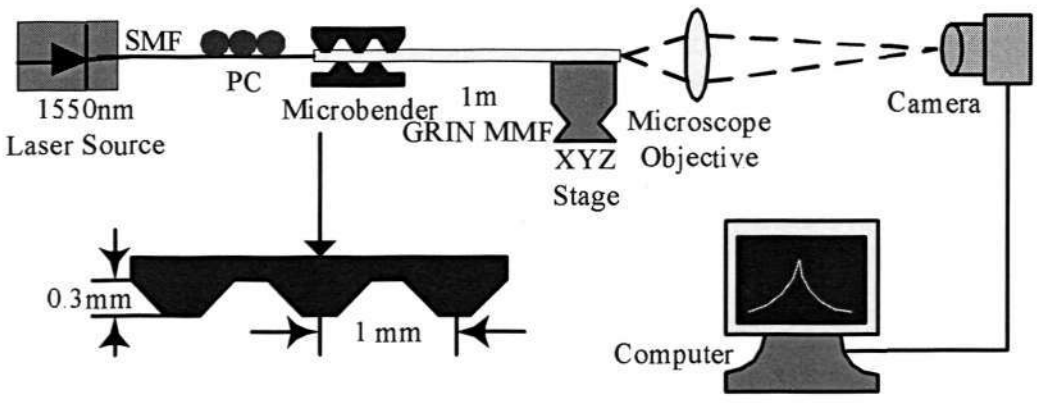

Fig. 5.7 Experimental setup for examining the near-field pattern from a GRIN MMF

Experiments were carried out to verify the theoretical analysis. The experimental setup for examining the near-field pattern of a 62.5-μm core GRIN MMF (with a 125-μm coating) subject to microbending is shown schematically in Fig. 5.7. A three-bend microbending deformer with a pitch of Λ = 1 mm was applied to the MMF which was approximately 1 meter long. The lower plate of the microbend deformer was fixed and the upper part could be displaced in the vertical direction with the resolution of 0.1 μm. Light from a 1550-nm wavelength laser was launched to the MMF through a short length of a single-mode fiber (SMF). The SMF was spliced to the MMF at its center to ensure that only a few low-order modes, in particular, the HG_{00} mode, were preferentially excited in the MMF. A polarization controller (PC) was used to control the polarization state of light to ensure that the input light to the MMF was linearly polarized. The near-field pattern of the GRIN MMF was imaged to a camera with a microscope objective and an XYZ translation stage. The image captured by the camera was digitized and processed by a computer.

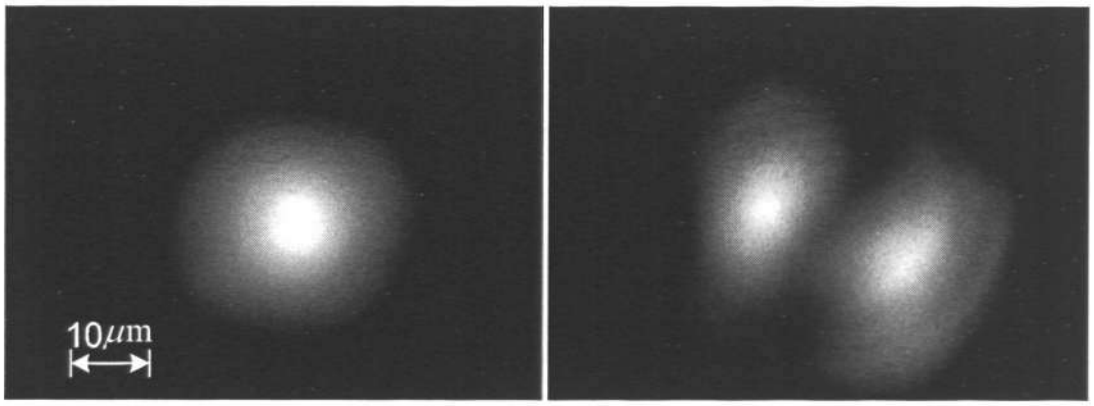

(a) (b)

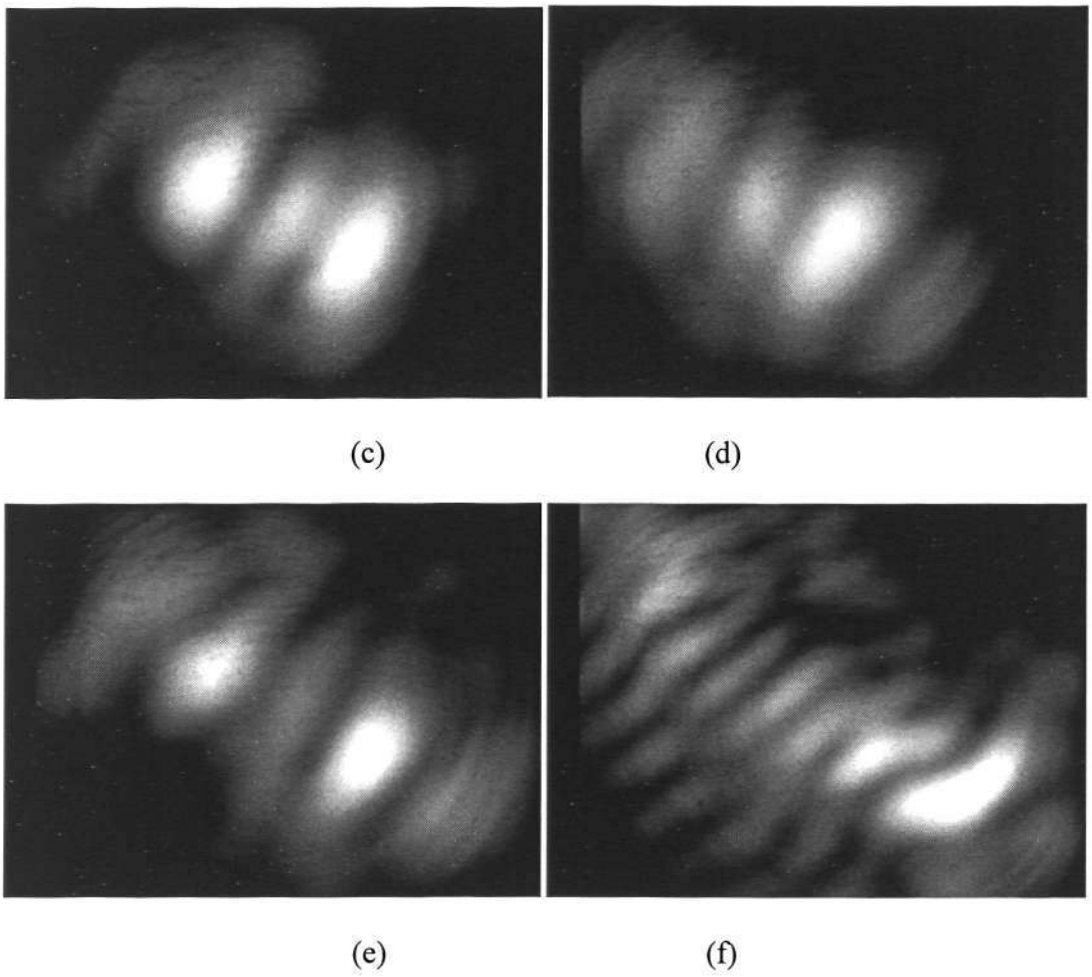

Fig. 5.8 Near-field patterns from the GRIN MMF measured at (a) $\delta = 0$, (b) $\delta = 10\ \mu$m, (c) $\delta = 15\ \mu$m, (d) $\delta = 19\ \mu$m, (e) $\delta = 23\ \mu$m, and (f) $\delta = 30\ \mu$m

The near-field patterns measured for different values of microbending displacement δ are shown in Fig. 5.8. Without any microbending ($\delta = 0$), the near-field pattern, as shown in Fig. 5.8 (a), appears to be dominated by that of the HG_{00} mode. When the value of δ reaches 10 μm, two maxima appear in the near-field pattern, as shown in Fig. 5.8 (b), which can be identified as the pattern for the HG_{10} mode. By increasing δ further and further, more maxima appear in the near-field pattern and the pattern can be identified with that of a dominant high-order mode. For

example, the patterns shown in Fig. 5.8 (c), (d), and (e) can be identified with those of the $HG_{20,}$ $HG_{30,}$ and $HG_{40,}$ modes, respectively. Even when δ reaches 30 μm, the near-field pattern can still be identified vaguely with that of the HG_{60} mode although the pattern actually contains several high-order modes with comparable strengths. The measured values of microbending displacement δ required for selecting the HG_{10}, $HG_{20,}$ $HG_{30,}$ and $HG_{40,}$ modes, respectively, as the dominant coupled mode are 10 μm, 15 μm, 19 μm, and 23 μm, respectively (Fig. 5.8). The corresponding theoretical values for a bare fiber, as shown in Fig. 5.2 (b), are 4 μm, 5.6 μm, 6.8 μm, and 7.8 μm, respectively. The experimental values are ~2.7 times on average larger than the theoretical values, which suggests that the microbending displacement of the coated fiber is approximately 2.7 times larger than that actually experienced by the glass fiber. The experiments were repeated by removing the coating of the fiber and obtained a clean HG_{10} near-field pattern with a microbending displacement of 4 to 5 μm, in good agreement with the theoretical value 4 μm. As a bare glass fiber is very fragile, it cannot be used to verify the theory at large values of microbending displacement. It should also be noted that the input light to the MMF actually contained a small amount of high-order modes, which served to contaminate the measured near-field patterns. Nevertheless, the microbend-induced mode selection effect was clearly demonstrated by the experimental results.

5.6 Fiber microbend sensors

This section studies fiber microbend sensors. The focus is on the design and responses of a fiber Bragg grating incorporated microbend sensor consisting of single mode fiber leads at the input and output.

5.6.1 Generic fiber microbend sensor

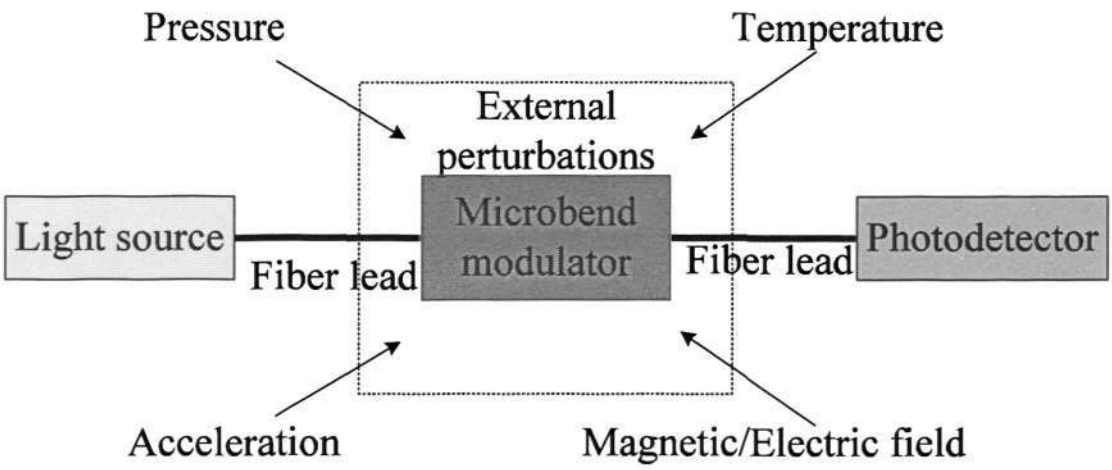

Fig. 5.9 A generic fiber microbend sensor

Here the analyses presented in [39] is followed for a generic fiber microbend sensor. An ideal generic microbend sensor is configured as shown in Fig. 5.8. The microbend fiber part could be in any form that is capable for bending the sensing fiber in regular pattern with the period Λ. The effects of environment change on the light transmission coefficient through the bent fiber can be given as

$$\Delta T = \left(\frac{\Delta T}{\Delta X}\right) D \Delta E , \tag{5.24}$$

where

$$D\Delta E = \Delta X , \tag{5.25}$$

T is the amount of change of transmission coefficient, ΔE is an appropriate environmental change, ΔX amount of change in the fiber deformation X, D is a constant which depends on the environment change ΔE. In terms of the applied force ΔF, Eq. (5.24) becomes

$$\Delta T = \Delta F \left(\frac{\Delta T}{\Delta X} \right) \left(k_f + \frac{A_s Y_s}{l_s} \right)^{-1} . \tag{5.25}$$

where k_f is the bent fiber force constant, A_s, Y_s and l_s are the cross section area, Young's modulus, and the length of the deformer spacers, respectively. $\Delta T/\Delta X$ relates the change in transmission to the change in fiber deformation amplitude. The change in the photodetector output signal is used to detect the original environmental perturbation ΔE.

In principle, various environment parameters can be sensed with the microbend sensor configured in Fig. 5.8, where the deformer converts the environmental parameter ΔE to a force ΔF on the bent fiber as

$$\Delta F = \Delta E \cdot C , \tag{5.26}$$

where C is a simple function of deformer parameters.

Therefore the expressions for many environmental parameters, such as pressure, temperature, acceleration, and magnetic/electrical field, can be obtained.

For pressure

$$\Delta T = \left(\frac{\Delta T}{\Delta X}\right) A_p k_f^{-1} \Delta P , \tag{5.27}$$

where ΔP is the change in pressure.

For temperature

$$\Delta T = \left(\frac{\Delta T}{\Delta X}\right) \alpha_s l_s \Delta\theta , \tag{5.28}$$

where $\Delta\theta$ is the temperature change, and α_s is the thermal expansion coefficient of the spacers.

For uniaxial acceleration

$$\Delta T = \left(\frac{\Delta T}{\Delta X}\right) m_p k_f^{-1} \Delta a , \tag{5.29}$$

where Δa is the acceleration level, and m_p is the mass of the deformer plate.

For magnetic/electric field

$$\Delta T = \left(\frac{\Delta T}{\Delta X}\right) d_{33}^{H,E} l_s \Delta H_F, E_F . \tag{5.30}$$

where $\Delta H_F, E_F$ is the change in magnetic or electric field, and $d_{33}^{H,E}$ is the magnetostrictive strain coefficient of the spacer material in the case of a magnetic field or the piezoelectric strain constant in the case of an electric field.

Under an environmental perturbation ΔE, the photodetector output the signal i_s

$$i_s = \frac{qeW_0}{hv}\left(\frac{\Delta T}{\Delta X}\right) D\Delta E . \tag{5.31}$$

In Eq. (5.31), h is Planck's constant, v is the optical frequency, q is the detector quantum efficiency, and W_0 is the optical power at the input. Provided that the detection system is limited by shot noise, the S/N power ratio is

$$i_s^2 / i_N^2 = \left(\frac{qW_0}{hv}\right)\left(\frac{\Delta T}{\Delta X}\right)^2 D^2 \left(\Delta E\right)^2 \left(2T\Delta f\right)^{-1}, \tag{5.32}$$

with the mean square photodetector noise given as [51]

$$i_N^2 = 2e\left(qeW_0 T / hv\right)\Delta f , \tag{5.33}$$

where the Δf is the detector bandwidth.

The smallest signal that can be detected is given for the condition S/N = 1, which yields

$$\Delta E_{\min} = D^{-1}\left(\frac{\Delta T}{\Delta X}\right)^{-1}\sqrt{\frac{2Thv\Delta f}{qW_0}} . \tag{5.33}$$

In Eq. (5.33), the first factor is specific to the particular design of the environmental sensor; the second two factors are general and apply to all environmental microbend sensors. In terms of ΔX defined by Eq. (5.25), Eq (5.33) is transferred to

$$\Delta X_{\min} = \left(\frac{\Delta T}{\Delta X}\right)^{-1}\sqrt{\frac{2Thv\Delta f}{qW_0}} . \tag{5.34}$$

Eq. (5.34) suggests the response of a specific sensor can be predicted by separately determining D, as long as the performance of the generic microbend fiber sensor is known.

5.6.2 FBG incorporated Microbend sensors

In Chapter 2, the fiber microbend sensor consisting of SMF leads at both the input and output was reviewed. Such a new type SMS microbend sensor has many advantages over the conventional microbend sensor that uses the MMF leads. Here we will propose and demonstrate an SMS microbend sensor that incorporates a single-mode fiber Bragg grating to achieve the simultaneous measurement of a mechanical parameter and the environment temperature.

5.6.2.1 Principle of operation

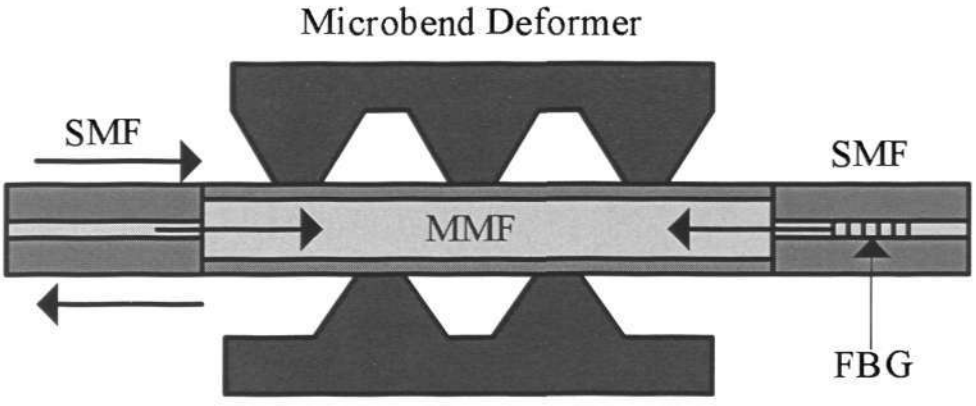

(a)

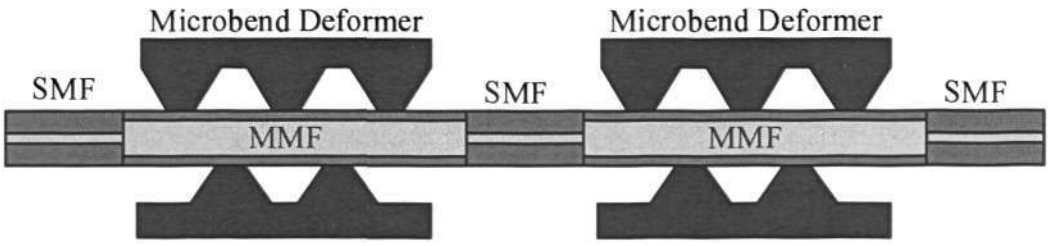

(b)

Fig. 5.10 (a) The proposed microbend sensor that incorporates an FBG; (b) the equivalent model at the Bragg wavelength

The proposed microbend sensor is shown schematically in Fig. 5.9(a), where an MMF of several centimeters long is used as the sensing fiber. Light is launched into the MMF from a single-mode fiber (SMF), which is aligned to the center of the MMF. The other end of the MMF is spliced to a single-mode fiber that contains an FBG. Microbending is applied to the MMF to produce a modulation of the light intensity, which serves as a measure of the microbending displacement. The light that passes through the MMF is reflected by the FBG and the wavelength of the reflected light is determined by the Bragg wavelength of the FBG, which is sensitive to the temperature. Therefore, the intensity of the reflected light collected by the SMF lead is a measure of the mechanical parameter, while its wavelength is a measure of the temperature. Note that the light reflected by the FBG goes through the MMF again, so the output light from the sensor (at the Bragg wavelength) actually goes through the microbend sensor twice, as shown by the equivalent model in Fig. 5.9 (b). In practice, the FBG must be shielded from unwanted tension or pressure. This can be done by designing a suitable sensor head that houses both the MMF and the FBG to ensure that the FBG is stress-free.

The proposed microbend sensor offers many advantages over the conventional microbend sensor. First, it provides simultaneous measurement of both microbending displacement and temperature. Second, it gives higher microbend sensitivity (since the light passes through the microbend sensor twice, equivalently the total number of microbends is doubled). Third, thanks to the use of an SMF lead, the sensor output is more stable. Fourth, the reflection-mode operation allows single-end access. Fifth, wavelength-division multiplexing of a number of parallel sensors is possible.

When the SMF and the MMF are aligned at their centers, only low-order modes of the MMF are excited [57]. The microbending applied to the MMF causes light couplings from low-order modes to high-order modes, which represents a loss when light is collected by the output SMF lead. Therefore, the configuration of using SMFs as both the input and output leads [48] provides higher sensitivity than the conventional configuration that uses the MMF as the sensor lead. The proposed sensor is even more sensitive, as the output light passes through the microbend sensor twice. Using the fiber parameters and the theoretical approaches given in Section 5.3, the responses of the proposed sensor ("Sensor with FBG") and the sensor proposed in [48, 98, 99] ("Sensor without FBG") were calculated, assuming the use of a three-bend microbend deformer and the excitation of only the fundamental mode in the MMF. The simulation involves the calculation of the modal distribution in the microbend MMF and the coupling loss between the MMF and the SMF. The results

are shown in Fig. 5.10, which confirm theoretically that our proposed sensor is indeed more sensitive.

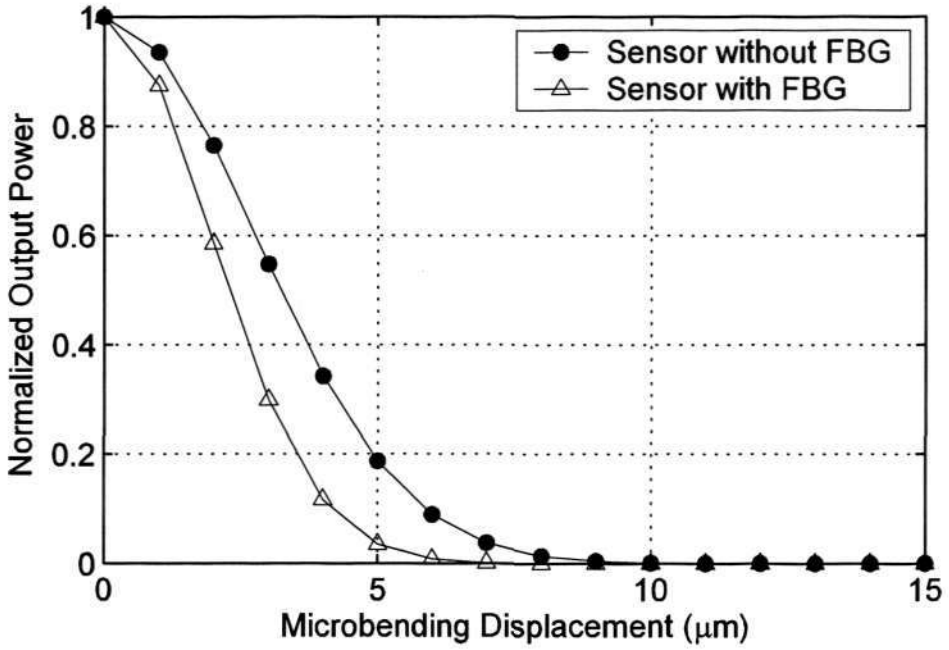

Fig. 5.11 Calculated normalized output power as a function of the microbending displacement for the proposed microbend sensor ("Microbend sensor with FBG") and the sensor proposed in [48] ("Microbend sensor without FBG")

5.6.2.2 Experimental results and discussions

In the implementation of the sensor, a 4-centimeter long standard graded-index (GI) MMF with a parabolic profile (from Fujikura) is used as the sensing fiber (which is employed in the previous sections) and a standard SMF (Corning SM 28) as the lead. The SMF was also used for the writing of the FBG. The MMF had a core diameter of 62.5 μm, a core index of 1.477, and a cladding index of 1.447, and the SMF had a spot size of 10 μm at 1550 nm. The FBG had a Bragg wavelength at 1555.91 nm (measured at 31.9 °C) and a peak reflectivity of 99.999 %. A three-bend microbend

deformer with a pitch of Λ = 1 mm was applied to the MMF, as shown in Fig. 1(a). The value of Λ was chosen to be close to the critical spatial period of the MMF to produce the highest microbending loss [39]. The microbending displacement was the mechanical parameter to be measured. The microbend sensor together with the FBG was placed in a temperature-controlled chamber. As described in the previous section, we need to detect both the intensity and the wavelength of the output light from the sensor to retrieve the signals for displacement and temperature measurements. Two simple schemes to demodulate the output signals were implemented.

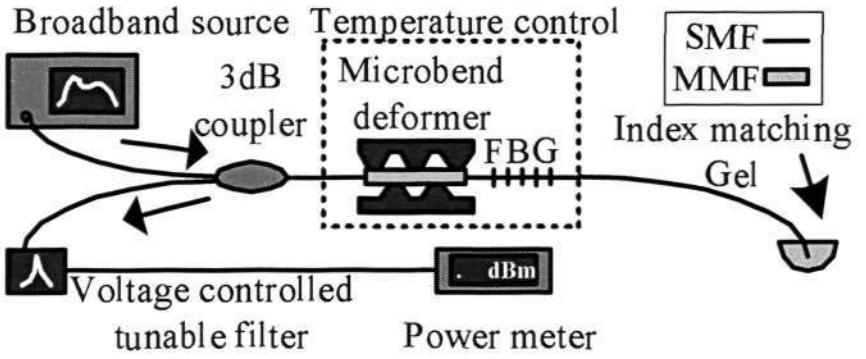

(a)

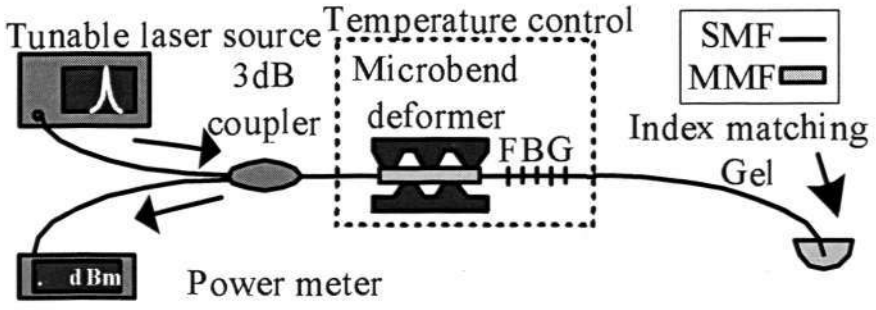

(b)

Fig. 5.12 Experimental setups for signal demodulation: (a) using a broadband source and a tunable filter; (b) using a tunable laser.

The experimental setup for the first scheme is shown in Fig. 5.12(a). The output

light from a broadband source (ASE spectrum of an erbium-doped fiber) was launched into the sensor via a 3 dB directional coupler. The reflected light from the sensor was made to pass through a voltage-controlled tunable fiber Fabry-Perot (FFP) filter (from Micron Optics) and then detected by a power meter (Agilent 81634B). The FFP filter had a tuning range from 1530 nm to 1570 nm. The power meter recorded a maximum power only when the FFP filter was tuned to the Bragg wavelength of the FBG. Therefore, when the power meter recorded a maximum value, the wavelength reading of the FFP filter was a direct measure of the temperature and the corresponding power reading was a measure of the microbending displacement. The experimental setup for the second scheme is shown in Fig. 5.12(b), where a tunable laser (Agilent 81680A) with a tuning range from 1546 nm to 1584 nm was employed to replace the broadband source and the FFP filter. When the emitting wavelength of the laser was tuned to the Bragg wavelength of the FBG, the power meter recorded a maximum value. The wavelength reading of the tunable laser thus measured the temperature, while the corresponding power reading measured the microbending displacement. The resolution of the power meter was –110 dBm. The spectra of the FBG, the tunable FFP filter, and the tunable laser, measured with an optical spectrum analyzer (Advantest Q8384), are shown in Fig. 5.13. The same broadband source was used for measuring the spectra of the FBG and the FFP filter.

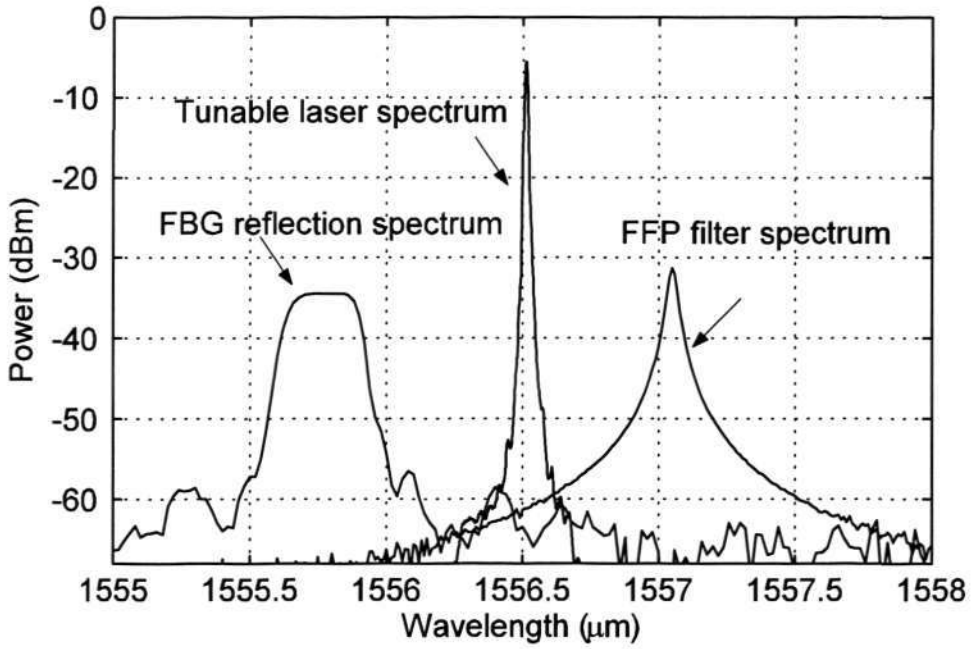

Fig. 5.13 Measured spectra for the FBG, the tunable FFP filter, and the tunable laser

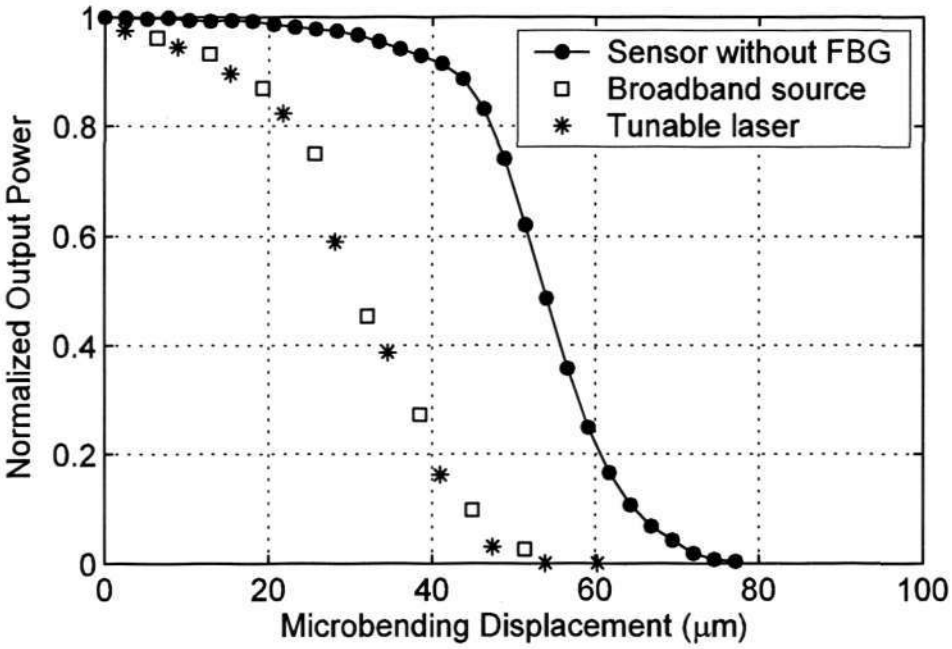

(a)

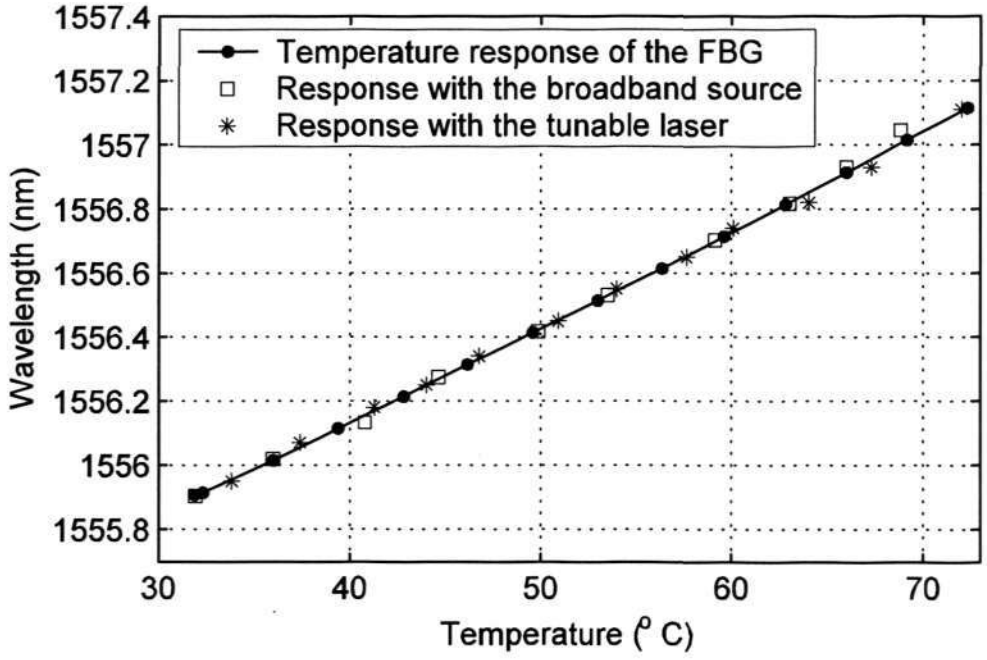

(b)

Fig. 5.14(a) Normalized output power as a function of the microbending displacement; (b) Wavelength measurement as a function of the temperature of the sensor

The normalized output power recorded by the power meter is shown as a function of the microbending displacement in Fig. 5.14(a). The results obtained from both schemes are presented in the same figure and they agree closely with each other. We also did experiments on the microbend sensor with the FBG removed (i.e., the configuration given in [4]) using the same tunable laser and the power meter, and the results are given in Fig. 5.14 (a) for comparison. The experimental results shown in Fig. 5.14 (a) agree qualitatively with the simulation results given in Fig. 5.11. In the simulation a bare MMF was assumed, while an MMF with a thick coating (125 μm in diameter) was actually used in the experiments. The fiber coating needed to be kept as a part of the microbend sensor, since it served as both the material to absorb radiation

power and the jacket to prevent the fiber from being broken by the deformer. Because of the presence of the fiber coating, the microbending displacement needed to generate the same normalized power output in the experiments should be much larger than that predicted by the simulation. In practice, it is desirable to keep the fiber coating, as it can serve to absorb the radiation power and prevent the glass fiber from being damaged by the deformer.

The output power of the broadband source (through the FFP filter) was –22 dBm, while that of the tunable laser was 0 dBm. When no microbending was applied to the MMF, the output powers of the two demodulation schemes were –33 dBm and –9.5 dBm, respectively. The difference from the output power of the corresponding light source accounted for the insertion loss of the SMF coupler (6 dB) and the coupling loss between the MMF and the SMF (5 dB for the broadband source and 3.5 dB for the tunable laser). The data points of Fig. 5.14(a) were within the uncertainty of the scheme. This uncertainty was obtained by repeating the measurement to find the maximum power variation at a certain microbend state. The scheme based on the broadband source showed a power uncertainty within ±2%, which corresponded to an uncertainty in the microbending displacement of ±1 μm. On the other hand, the power uncertainty in the scheme based on the tunable laser was measured to be within ±1%. These uncertainties represented the maximum power variations obtained from repeated measurements at a given microbending displacement.

The output power was found to be insensitive to the temperature. When the temperature in the chamber was increased from 30 °C to 100 °C, the power variations measured at a fixed microbending displacement were found to be less than ±1%, which was within the system uncertainty. In practice, the microbend deformer should be made of a material that has a small thermal expansion coefficient to minimize changes on the dimensions of the deformer due to temperature variations.

The center wavelength of the FBG, which was determined by scanning across the reflection spectrum of the FBG with the tunable FFP filter or the tunable laser, is shown in Fig. 5.14(b) as a function of the temperature. The shift in the Bragg wavelength of the FBG with the temperature was also measured directly with the optical spectrum analyzer and the results are presented in Fig. 5.14(b). The three sets of results agree closely. By repeating the measurement and comparing the results with the directly measured temperature response, the uncertainty was estimated with the maximum variance of our scheme to the actual response. The scheme based on the broadband source gave a wavelength resolution of ±0.05 nm (i.e., a temperature uncertainly of ±1.7 °C), while that based on the tunable laser gave a resolution of ±0.03 nm (i.e., a temperature uncertainty of ±1.0 °C). The wavelength resolution was limited by the tuning device used.

Table 5.1 gives a comparison between these two schemes. Both schemes are effective for signal demodulation. The scheme based on a broadband source can be

much cheaper to implement, if a low-cost tunable filter is used (e.g., a tunable FBG). On the other hand, the scheme based on a tunable laser can provide a much higher output power, which allows multiplexing of many more sensors.

Table 5.1: A comparison between the two schemes

	Output Power	Temperature Resolution	Microbend Resolution	Cost
Tunable Laser Source scheme (0dBm)	-9.5 dBm	±1 °C	± 1 μm	High because of the tunable laser source
Broadband source scheme (-22dBm)	-33 dBm	±1.7 °C	± 0.5 μm	Could be low when using low-cost FBG filters

5.7 Conclusions

Periodic microbend in the MMF has been investigated in this chapter. The novel aspects of this work are concluded as follows.

A theoretical model has been developed for studying the microbend-induced mode coupling in an MMF. In particular, simple analytical results were derived for a parabolic-profile MMF. For such a fiber, the fundamental mode can be coupled preferentially to a specific high-order mode at a microbend and the order of the dominantly coupled mode increases progressively as the amount of microbending increases. The theory was used to study quantitatively the function of a microbend-based mode scrambler. The experimental results from measuring the

near-field patterns of a GRIN MMF subject to microbending as well as its reflection spectra from an MMFBG agree well with the theoretical predictions. Although this theory has been detailed only for a parabolic-profile MMF, such an approach is applicable to any MMF. The theory should be useful for the evaluation and design of microbend-based devices and sensors.

A microbend sensor incorporating an FBG was proposed and demonstrated for simultaneous measurement of microbending displacement and temperature. The output signals can be detected effectively with either a tunable filter in conjunction with a broadband source or a tunable laser. The sensor produces a stable output, shows good sensitivities in both microbending and temperature measurements, provides convenient single-end access, and allows multiplexing of similar sensors based on wavelength-division multiplexing. The proposed sensor is the first of its kind, which combines the advantages of an intensity-based sensor (simple configuration and low cost) and a wavelength-based sensor (absolute measurement and multiplexing capability).

CHAPTER 6

APPLICATIONS OF MMFBG IN ERBIUM-DOPED FIBER LASERS

6.1 Overview

The characteristics of MMFBG have been discussed in detail in Chapter 3. Particularly, the most interesting property of an MMFBG is that its spectral response could be easily tuned by varying the modal power distribution. In this chapter, motivated by wide applications of the single-mode FBGs in the fiber laser systems, potential applications of the MMFBG in SMF laser systems are proposed and demonstrated. The research focus in this chapter is on the wavelength-tuning ability of MMFBG in forming wavelength-switchable erbium-doped fiber lasers.

Fiber lasers, in particular EDFLs, have attracted much research interest because of their potential applications in WDM and optical fiber sensing systems [100-112]. Erbium-doped fiber (EDF), as the gain medium, is advantageous as it is capable of high efficiency pumping in a relatively short length. On the other hand, the large homogenous gain broadening that is unavoidable for EDF, prevents the EDFL from lasing stably in multiple wavelengths. Therefore, many efforts have been made to

improve the stability of the multi-wavelength EDFL at room temperature [113]. Stability of multi-wavelength EDFLs, however, is still a key issue that needs to be fully addressed. Reliable and practical methods are desired to realize the implementation. Recently, an alternative, wavelength-switchable EDFL, has been developed to satisfy those applications where several lasing lines are required [101, 104]. Switching here means that it is possible to select the lasing wavelength among several discrete lasing lines. In such a system, the homogenous gain broadening of the EDF is exploited to stabilize the single-wavelength lasing. Certainly, the number of switchable wavelengths and the system complexity are always important considerations.

From the study in Chapter 3, obviously MMFBG has two key spectral advantages over its single-mode counterpart. Firstly, the spectrum of MMFBG covers a wide wavelength range and consists of equally separated reflection peaks. Secondly, the spectrum of MMFBG can be easily tuned by changing the modal power distribution. Therefore, the tuning ability of MMFBG could be potentially used for implementing wavelength-switchable EDFLs.

In this chapter, two wavelength-switching techniques are described to implement wavelength-switchable EDFLs, both theoretically and experimentally. The first scheme is based on the study in Chapter 4. As it has been proved that the microbending applied to the MMF can effectively change the modal power

distribution, the first wavelength switching scheme is realized through tuning the microbending applied to an MMF. The second scheme follows the principle that the mode with different orders can be preferentially excited at different radial position on the cross section of an MMF through launching with an SMF [57, 114-118]. Since the fiber modes in distinct orders spatially distribute at different radius positions on the cross section of the MMF, the selective mode excitation and filtering are accomplished by varying the axial alignment of the SMF and the MMFBG. In principle, they both change the mode distribution in the MMF and select the mode by the SMF. The theoretical studies on wavelength switching and the experimental results on the performance of the EDFLs are given for both schemes, respectively.

6.2 Erbium-doped fiber laser

The first EDFL was demonstrated by Snitzer and Woodcock in 1965 [119, 120]. The first rare earth doped SMF was developed by using modified chemical vapor deposition (MCVD) method by the researchers of Bell Labs [121], which was followed by advanced MCVD method at the University of Southampton [122]. In 1987, erbium-doped single mode fiber amplifier (EDFA) for traveling wave amplification of 1500-nm signals was developed [123, 124]. In 1989, Nakazawa used a high power 1480-nm laser diode as a pump [125]. These recent achievements in the area of EDFA opened the door for the implementation of EDFLs [126].

In an Erbium-doped fiber laser or amplifier, the pump light excites the rare earth ions to produce a population inversion giving rise to amplification at the signal wavelength by means of stimulated emission. EDFLs have many important advantages, including the tuning ability over a wide wavelength range, efficient and compact pumping with laser diodes, low threshold power level, and improved phase and intensity noise characteristics as compared to semiconductor lasers.

EDFL may be categorized into two types in the time domain according to whether they are continuous wave (CW) [127, 128] or pulsed [129]. In the wavelength domain they may be classified into single wavelength and multiwavelength. In this work, the focus is on the design of CW EDFLs, and the term EDFL will refer to CW EDFL in the rest of this thesis.

EDFL has been applied in WDM system for long distance transmission and optical fiber sensors, where usually multiple lasers operating at different wavelengths [130-133] are required. The multiwavelength EDFL, however, is difficult to be realized compared to other EDFL categories due to the inherent difficulty in achieving stable multiple wavelength laser operation. It is well known that the homogeneous broadening for gain media leads to instability of multiple wavelength lasers. Homogeneous broadening is caused by each individual atom, ion or molecule having the same finite spectral width for a given optical transition. Contributing mechanisms

include dipole interactions with the vacuum field and photon stimulated broadening [51, 113]. Each radiating entity is spectrally identical, hence the name homogeneous.

Although many efforts were made to realize stable multiwavelength EDFL [105, 108, 134-138], practical methods are few and alternatively a wavelength-switchable EDFL has been proposed for those applications that require laser operations at several discrete wavelengths [101, 104, 139]. In this chapter, two schemes are proposed for the use of the MMFBG for implementing wavelength-switchable EDFL.

6.3 Microbending scheme

In this section, a microbending scheme is proposed based on the microbending theory developed in Chapter 5 for the design of the wavelength switchable EDFL.

6.3.1 Principle of operation

First an SMF to MMFBG structure shown in Fig. 6.1 is studied for understanding the mode coupling mechanism at an SMF/MMFBG interface.

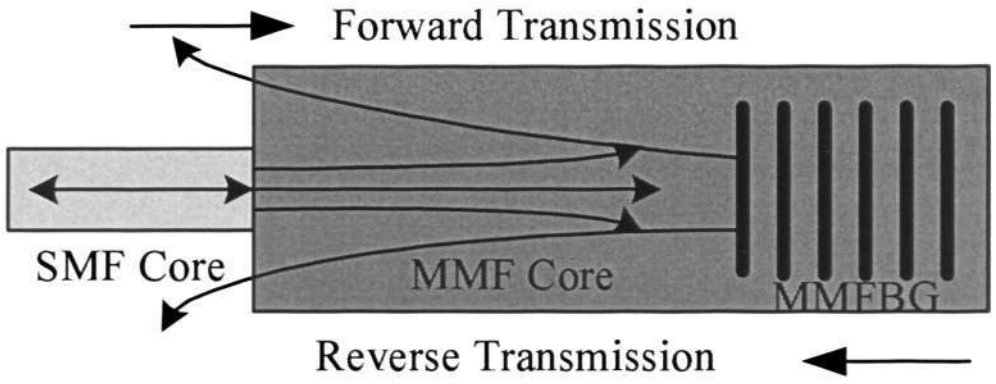

Fig. 6.1 SMF to MMFBG structure

The uniform MMFBG shown in Fig. 6.1 has been fabricated by using a standard 62.5 μm core graded-index MMF. Prior to the grating fabrication, the MMF was hydrogen-loaded under the pressure of 110 bar and the temperature of 80 ˚C for 7 days. A phase mask with a period of 1058.04nm was used to fabricate a 20mm long MMFBG. The grating was then stabilized by thermal annealing at 100˚C for 1 day.

In Fig. 6.1, the SMF is connected to the MMFBG at the center to preferentially excite the lowest order mode, i.e. HG_{00} mode. This mode is reflected by the MMFBG, appearing as a reflection at the wavelength λ_1 in the MMFBG spectrum. By applying the microbending on the MMF at the input of the grating, as was theoretically and experimentally verified in Chapter 4, a high-order mode will be preferentially excited rather than the fundamental mode according to the value of the microbending displacement. Ideally all the modes are reflected by the MMFBG, and the reflection to the preferentially excited mode has maximum amplitude, showing at wavelength λ_n. Certainly, all the modes are coupled again in the reverse direction because of the

presence of microbending. Obviously, the preferentially excited mode is most effectively coupled with the fundamental mode according to the theoretical analysis given in Chapter 3. At the SMF/MMF interface, the fraction of the optical power coupled back to the SMF is determined by the overlapping of the composite electric field between the single-mode and multimode fibers. It can be seen in Fig. 6.1, as it is axially aligned to the MMF, the SMF selects the fundamental mode propagating in the reverse direction, and filters out other modes. Subsequently, the reflection at λ_n (which is for the preferentially coupled mode) is coupled to the SMF with the highest power as compared with the other reflections. It might be noted that both forward and backward propagating modes reflected by the MMFBG go through the microbend MMF. They will not interact because the phase matching condition is not satisfied for the counter-propagating modes in the microbend region.

To confirm the analysis experimentally, the configuration shown in Fig. 6.2 was used to measure the reflection spectra of an MMFBG, which was connected to a segment of MMF undergoing microbending. The light was provided by a Broadband Source (Photonik) and was launched into the MMF that was subjected to tunable microbending. The end of the MMF was connected to an MMFBG that was fabricated under the same conditions as the gratings used in Chapter 3. Then, the light that was reflected back by the MMFBG, went through the MMF with periodic microbends again and was collected by the OSA (Advantest Q8384) via an SMF coupler. The

microbend deformer used in the experiment induced three bends on the MMF with a pitch of 1-mm, which is the critical spatial period of the GRIN MMF.

The reflection spectra measured at four microbending displacement values (0 μm, 15 μm, 22 μm, and 28 μm), are given in Fig. 6.3. Distinct peaks, corresponding to different principal modes, can be seen in each reflection spectrum, which is in fact a signature of the modal distribution in the fiber under the given microbending condition. The reflection spectra show clearly how the dominant coupled mode evolves with the microbending displacement. For the four microbending displacement values, the HG_{00}, HG_{20}, HG_{40}, and HG_{80} modes are, respectively, the preferentially coupled modes, which are in agreement with the near-field measurements and the theoretical predictions conducted in Chapter 5.

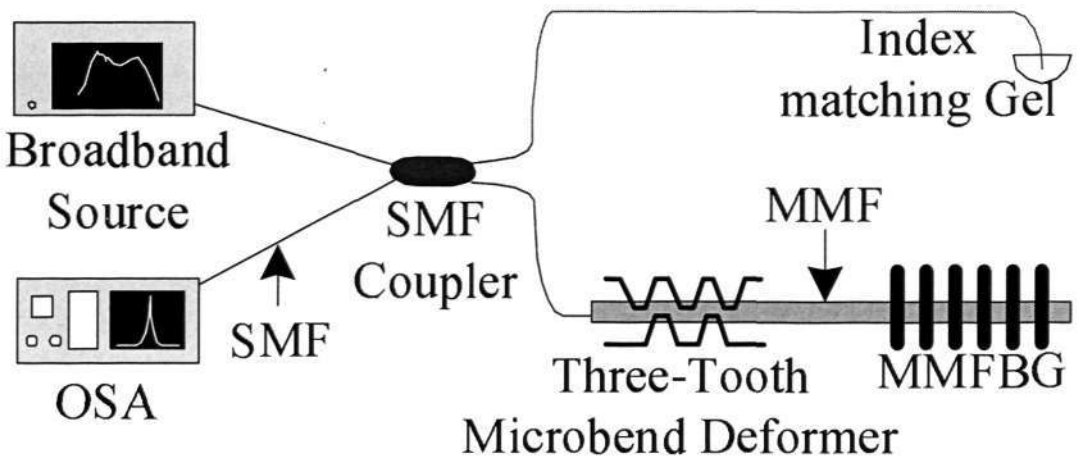

Fig. 6.2 Experimental setup to measure the reflection spectra of an MMFBG

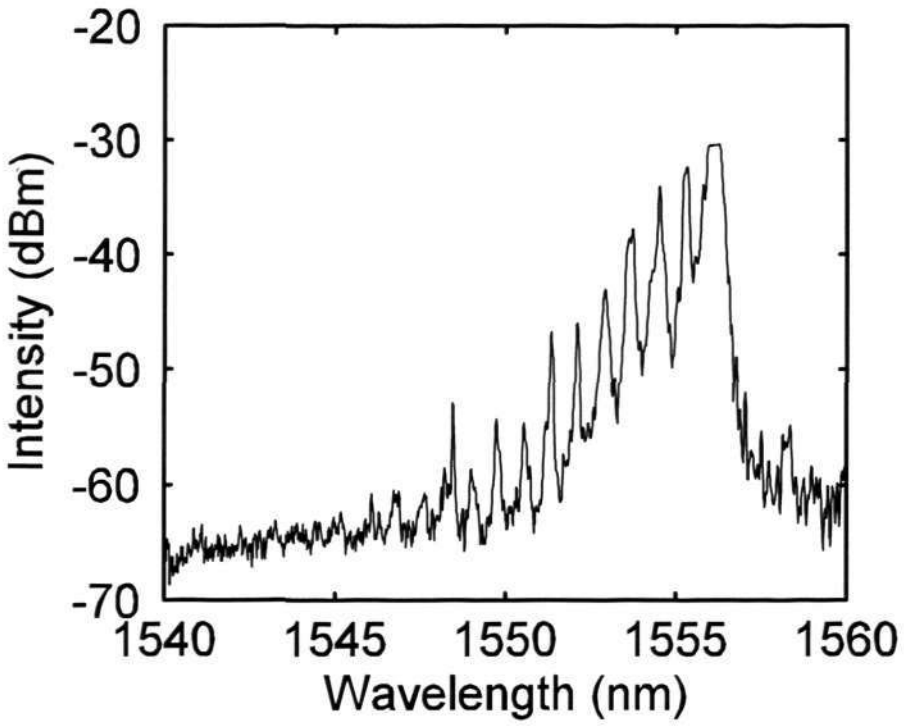

(a)

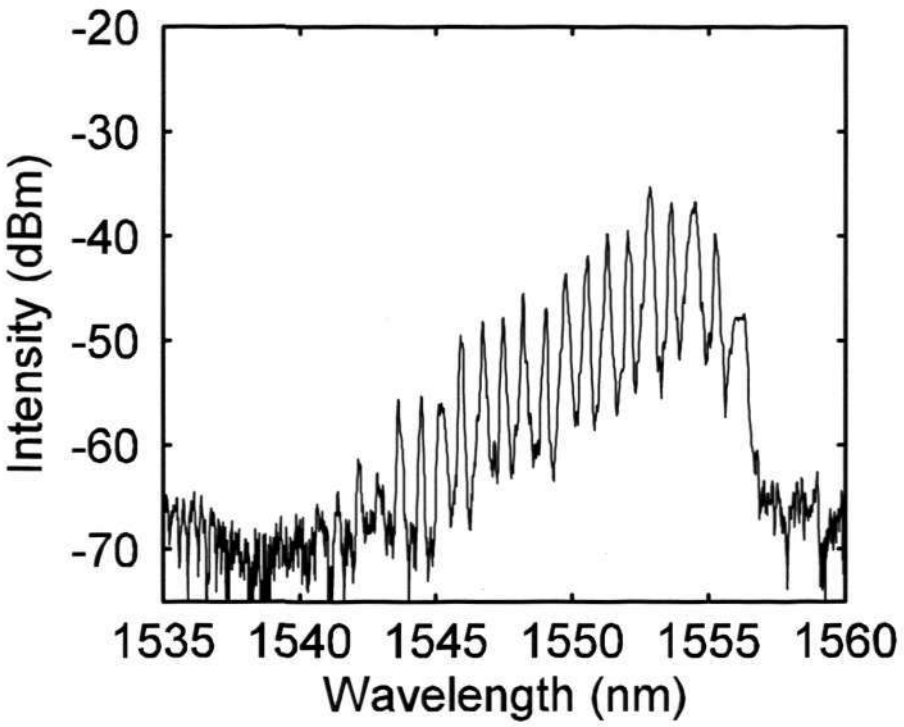

(b)

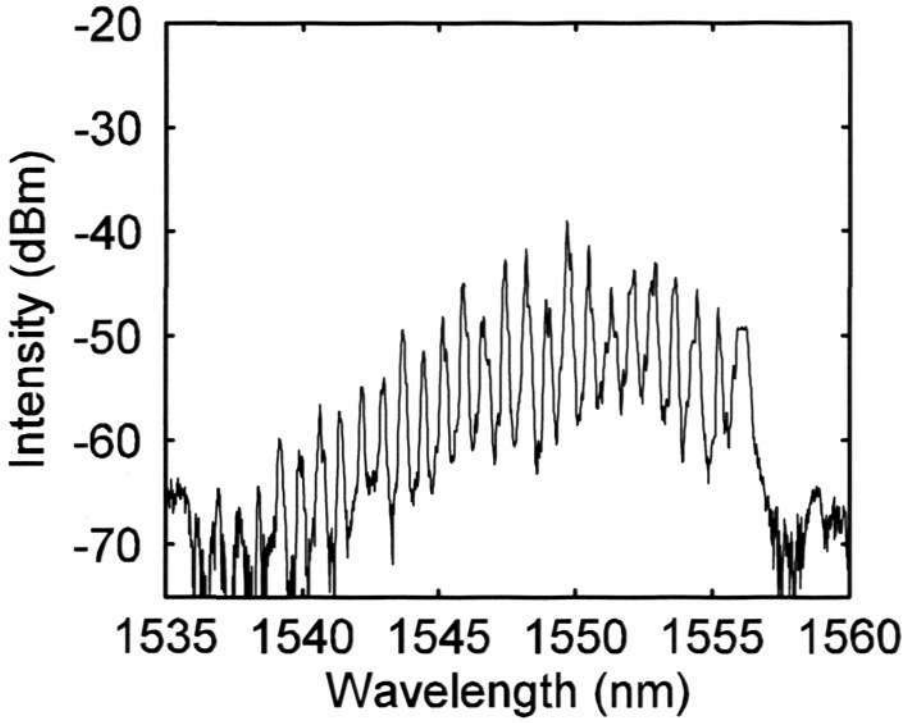

(c)

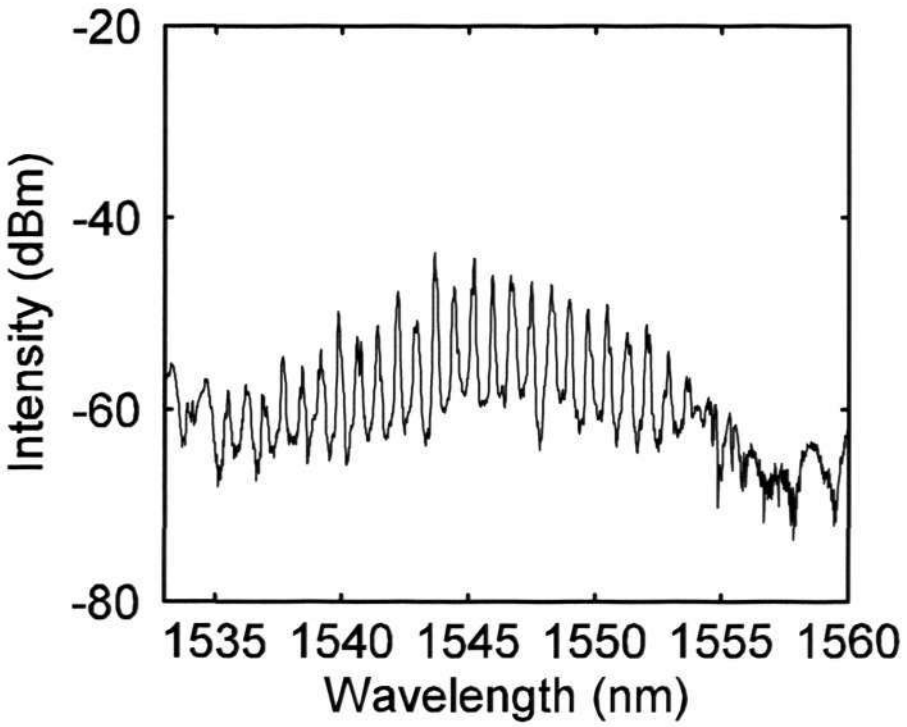

(d)

Fig. 6.3 Reflection spectra of the fiber subject to microbending measured with an FBG introduced at the other end of the fiber for (a) $\delta = 0$ μm, (b) $\delta = 16$ μm, and (c) $\delta = 22$ μm, and (d) $\delta = 28$ μm

6.3.2 Experimental results and discussions

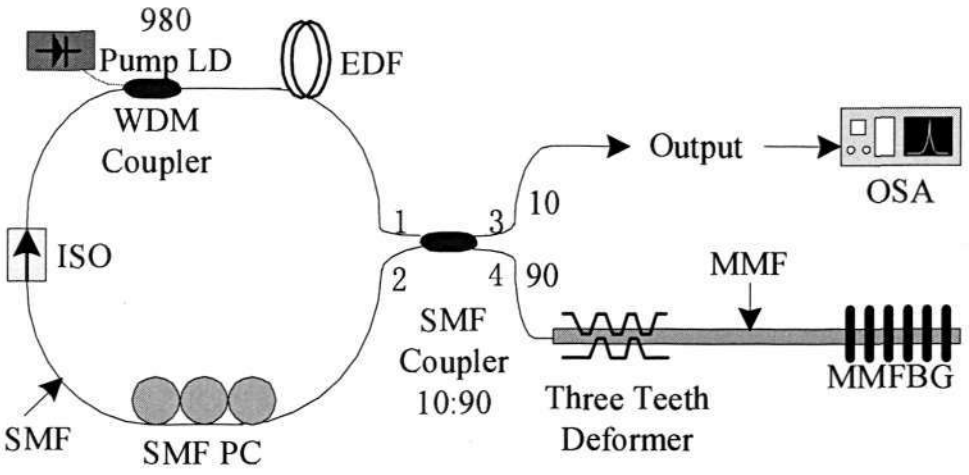

Fig. 6.4 Experimental configuration for the wavelength-switching EDFL using the microbending scheme

Fig. 6.4 sho ws the configuration of the proposed EDFL using the microbending scheme. A 6m long EDF, with ~1200ppm of erbium doping, is optically pumped by a 980nm laser diode (LD) through a WDM fiber coupler. A 90:10 fused fiber coupler acts as a 10% output coupler for the laser cavity. The isolator (ISO) ensures that the ring laser is unidirectional. The uniform MMFBG is fusion-spliced to port 4 of the SMF coupler, acting as the reflection mirror. The output (port 3 of the coupler) is measured with an OSA (Advantest Q8384). A polarization controller (PC) is used in the cavity to control the polarization components in the laser output spectrum. The three-tooth deformer with the Λ of 1mm is applied to the MMF to change the mode coupling condition. The adjustable microbending displacement δ of the deformer allows the flexible tuning of the mode coupling efficiency.

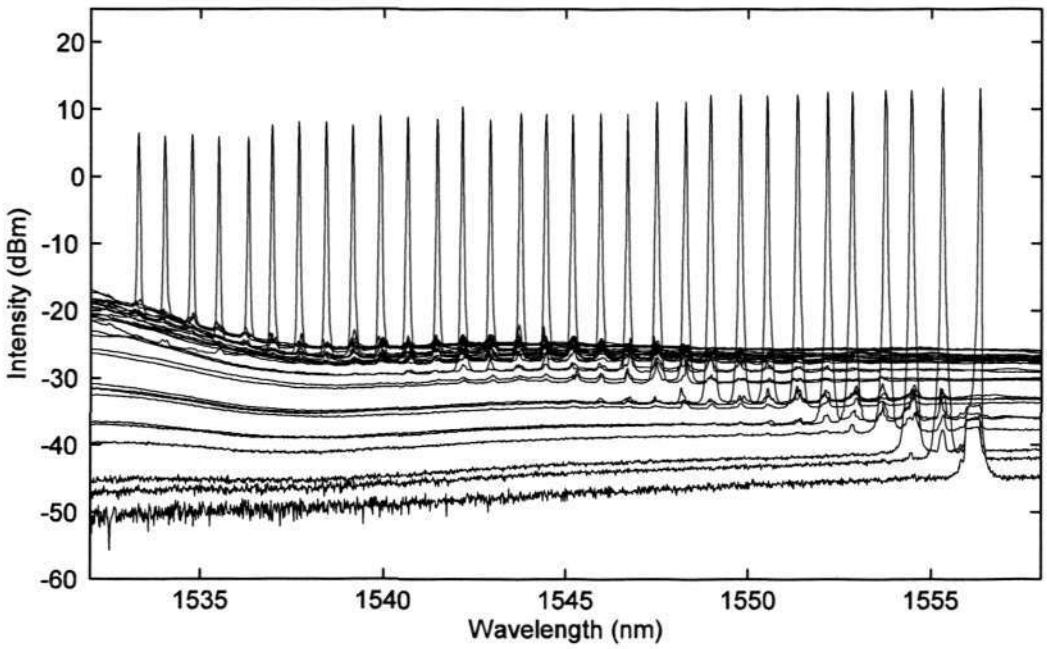

Fig. 6.5 All lasing lines with considerable Signal to ASE ratio obtained in the experiment for the microbending scheme

Without microbending, a single lasing line at 1556.26nm was obtained, corresponding to the reflection to the fundamental mode at the wavelength λ_1. By gradually increasing the microbending displacement of the deformer, the lasing wavelength blue shifted to a neighboring shorter wavelength. In fact, multiple reflections covered a wide wavelength range at different wavelengths as shown in Fig. 6.3. The single wavelength lasing, however, was stabilized by exploiting the homogeneous gain broadening in the EDF at room temperature, which successfully suppressed the side reflection peaks with lower reflectivity. Therefore, the lasing wavelength was only determined by the highest reflection.

When the EDF was pumped with a 60mw of 980nm LD, as was shown in Fig. 6.5, 31 discrete wavelengths were obtained ranging from 1533.28nm to 1556.26nm, where

the lasing line spacing is about 0.8nm exactly as what has been predicted by Eq. (3.8) in Chapter 3. When the lasing line blue shifted to a short wavelength, it came up with a raised amplified spontaneous emission (ASE) noise level and a slightly reduced lasing peak power due to the microbending loss. In Fig. 6.1, at the SMF/MMF interface, the high-order modes seem to have been filtered out when the light was being transmitted from the MMF to the SMF. Therefore, at large microbending displacement values, the power loss at the SMF/MMF interface was high compared to those with small microbending displacements. In addition, a large δ led to considerable radiation loss. Therefore, las er operation wa s not possible for those reflections to very high order modes (say, below 1533nm) due to high radiation loss. Nevertheless, high signal to ASE noise ratio was achieved for all lasing wavelengths. By using 980nm pump laser with a power of 60mw, the peak power of the laser at 1556.26nm was 20.94mW, and the lasing peak power reduced to 3.98mW at 1533.28nm. The output lasing was found to be stable, and no significant power or wavelength variation could be observed at room temperature. During the experiment, the maximum amplitude variation was measured to be less than 0.2dB. The range of switchable lasing wavelengths and the channel spacing could be changed by the MMFBG parameters.

The wavelength-switching phenomenon was no more than another manifestation of the mode coupling process shown in Chapter 5 (Fig. 5.2). According to the theory developed in Chapter 5, as the order of the mode increased, the reflection peak of the

FBG and hence the lasing wavelength decreased. Indeed, it was observed experimentally that the lasing wavelength shifted to the shorter wavelength, as the amount of microbending increased. A comparison of the mode orders, corresponding to the lasing lines due to reflections to the same principal modes and those calculated from the microbending theory, was given in Fig. 6.6. To take into account the effect of the fiber coating, the theoretical microbending displacements shown in Fig. 6 were already scaled up by the factor of 2.7, which was obtained from comparing the experimental results for a coated fiber with the simulation results for a bare fiber, as was discussed in the previous section. The theoretical results were found to agree reasonably well with the experimental results. In Fig. 6.6, the disagreement between the experiment and theory for high order modes is understandable, and the reason is given as follows. When taking into account of the coating effect, scale factor of 2.7 is used for the calculated results. The coating effect, however, is relatively small when the microbending displacement is large. Therefore, the scaled calculated results are slightly greater than the experimental results at large microbending displacements. It is noted that the coupling to the $HG_{16,0}$ or $HG_{17,0}$ mode did not lead to lasing, because for such a high-order mode, the coupling efficiency was so low that the gain of the erbium-doped fiber was unable to compensate for the cavity loss. In the experiments, extra lasing lines were present between those lines that corresponded to reflections to the same principal modes by the FBG. A total of 31 lasing wavelengths were actually obtained. These extra lasing lines were produced by couplings between principal modes in different orders through the FBG, which were not shown in Fig. 6.6.

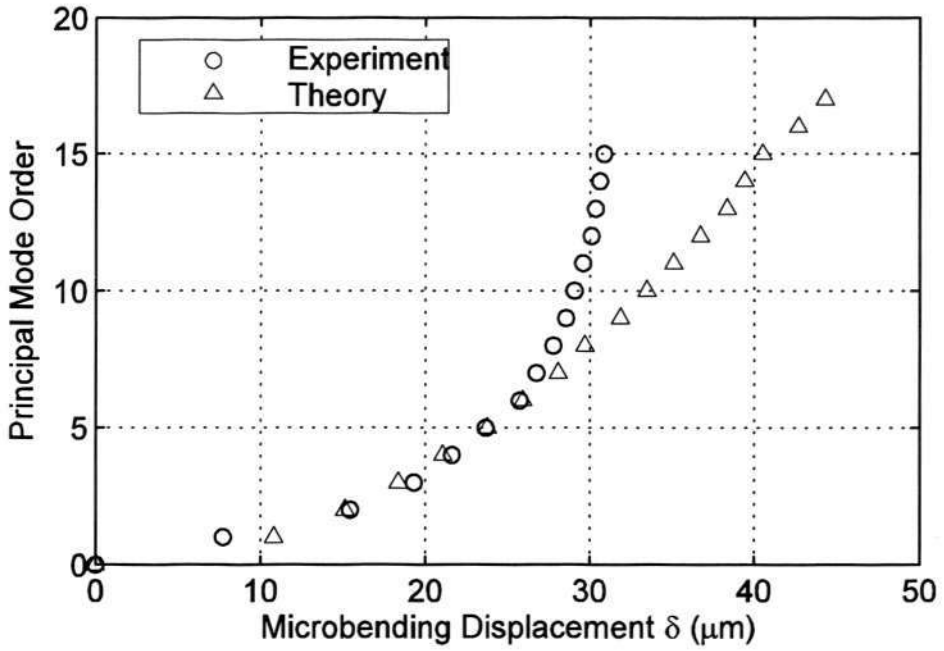

Fig. 6.6 Dependence of the mode order p of the dominantly coupled mode on the microbending displacement, when only the HG_{00} mode is launched into a three-tooth microbending deformer with a pitch of 1 mm.

6.4 Alignment scheme

In section 6.3, a wavelength-switching scheme based on microbending was described for the MMFBG incorporated EDFL. It is well known, that in a GRIN MMF, different order of modes are spatially distributed along the radial direction, and therefore the offset-launching techniques have been developed for exciting higher order modes [57]. Such mode selection techniques obviously are useful in designing the wavelength-switchable EDFL incorporating an MMFBG. In this section, both the theory and experiment are demonstrated for the alignment scheme based EDFL.

6.4.1 Principle of operation

The proposed alignment scheme, that changes the spatial mode distribution in an MMF, is to launch the light to different radial positions on the cross section of the MMF with an SMF [57, 116]. At each radial launching position a certain mode with the order m is favorably excited. Reflected by the MMFBG at the wavelength λ_n, this mode is coupled back to the SMF most efficiently as well, since it has the best overlapping integral with the SMF than any other mode. Therefore, the reflection at λ_n leads to lasing, provided that it is continuously pumped in a fiber ring laser cavity.

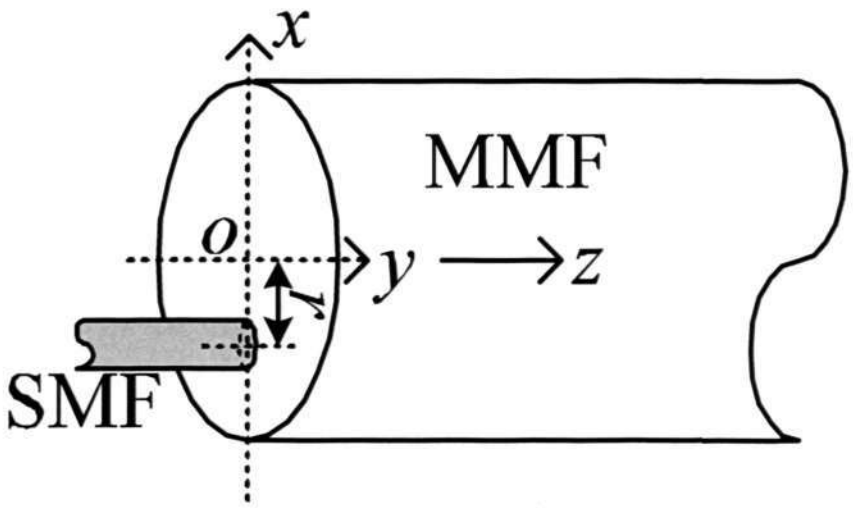

Fig. 6.7 Alignment of an SMF to MMF

A theoretical analysis has been developed to study the mode excitation when a Gaussion beam launched into an GRIN MMF [57], which is used here to obtain the relationship between the order m of the preferentially excited mode and the radial launching position r. As is shown in Fig. 6.7, the SMF and the MMF are placed end to end closely to each other. The light is launched into the MMF at the radial position r.

The launching beam can be assumed as a Gaussian beam under the condition of zero wave front, having the following components in Cartesian coordinates,

$$E_{in} = (2/w)(\pi Y_0 n_0)^{-1/2} \exp\{-[(x-r)^2 + y^2\}/w^2\}, \tag{6.1}$$

where n_0 and Y_0 are the refractive index and the intrinsic admittance of free space, respectively; w is the beam radius associated with the Gaussian beam. Since the SMF and the MMF have been placed closely, it is reasonable to assume that the beam width w matches well with the fundamental mode.

By using the Hermite-Gaussian mode here, the excitation coefficient for mode $HG_{p,q}$ is given as

$$C_{p,q} = (n_0 Y_0)^{1/2} \iint E_{in} \psi_{p,q}(x, y, 0) dx dy, \tag{6.2}$$

where $\psi_{p,q}(x,y,z)$ is the scalar wave field that has been given in Chapter 2 Eq. (2.14).

By solving Eq. (6.2), an analytical solution is obtained to show the order of the maximum excited mode group at tilt and offset launching conditions [57]. If the beam width w, launched to the MMF, is matched to the fundamental mode w_0 by writing $w = w_0$, without any tilt angle the order of the maximum excited mode group at offset launching condition becomes

$$m_{\max} = r^2 / w_0^2 + 1, \tag{6.3}$$

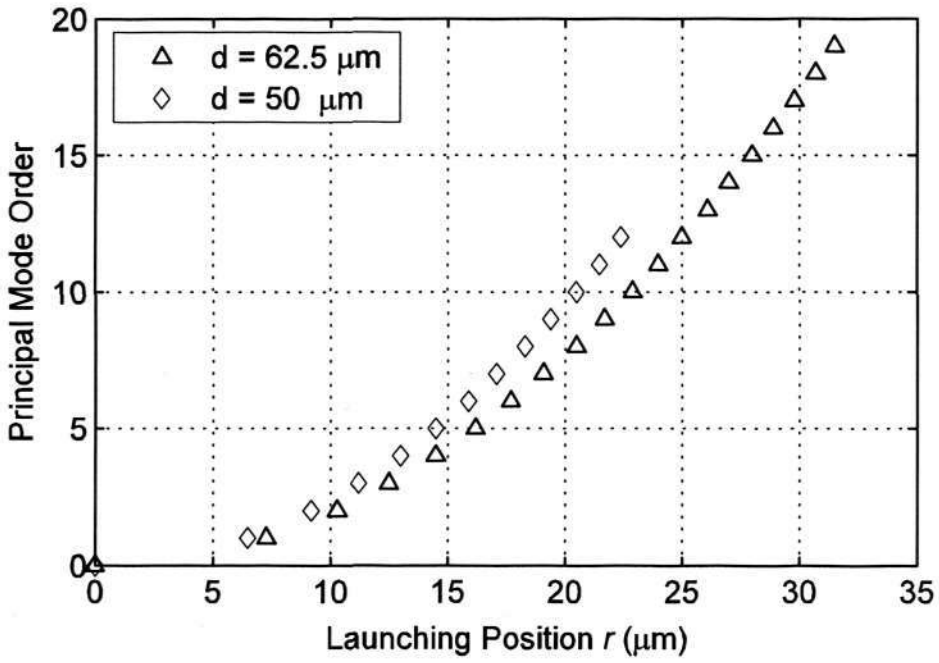

Fig. 6.8 Calculated dependence of the mode order p of the preferentially excited mode on the launching position r for 50 μm and 62.5 μm core diameter GRIN MMF.

Eq. (6.3) suggests that the order of the maximum excited mode increases together with the radial launching position. Therefore, when launching a broadband light source to an MMFBG from an SMF, the spectral response of the MMFBG varies with the radial launching position r of the SMF with reference to the axis of the MMF. With the help of Eq. (6.3), the dependence of the mode order p on the launching position r is calculated for 50 μm and 62.5 μm core diameter GRIN MMFs, as is shown in Fig. 6.8. By neglecting mode coupling in the MMF that is connected to the MMFBG, the excited mode groups are reflected by the MMFBG at different wavelengths where the phase matching condition is satisfied. According to the characteristics of the spatial mode distribution in the MMF, interestingly only those

reflected mode groups form a wavelength-dependent mode field on the cross section of the MMF. Therefore, the distribution of amplitudes at different wavelengths is determined by the spatially distributed MMF modes.

The spatial position of the SMF against the MMF can select the spatial mode groups that are coupled back to the SMF owing to the mode and wavelength dependent field on the cross section of the MMF. At the SMF/MMF interface, the fraction of the optical power launched back into the SMF is determined by the overlapping of the composite electric field. The spatial mode that is best matched to the SMF will propagate in it with the highest power. The reflection to this favorably coupled mode takes place at the wavelength λ_n and therefore eventually leads to lasing at this wavelength. The alignment tuning can be achieved with a resolution of 0.1 μm.

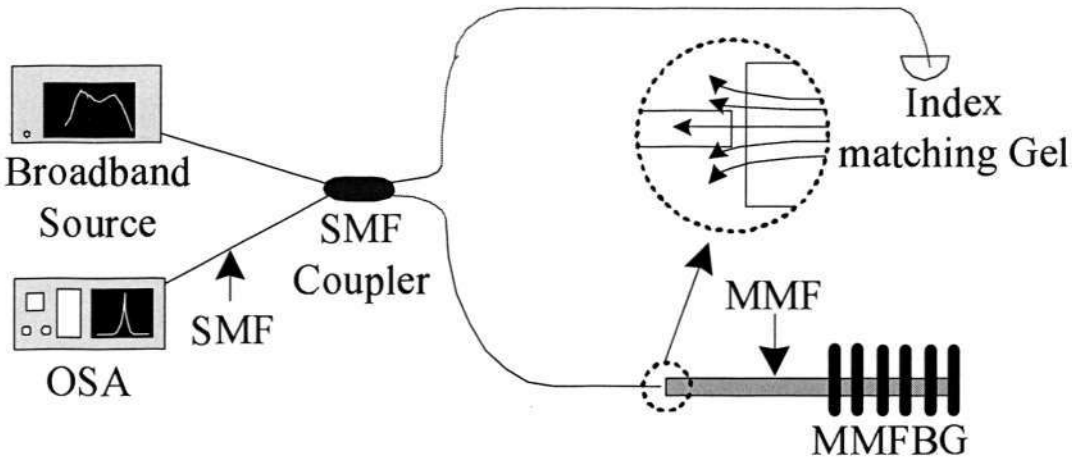

Fig. 6.9 Experimental setup for measuring the MMFBG spectra by using the alignment technique

To confirm the above analysis, the reflection spectra of the MMFBG were measured by using the alignment technique. Fig. 6.9 illustrates the experimental configuration for measuring the MMFBG spectra. The light was produced by a Broadband Source (Photonik) and was launched into an MMFBG at a radial position *r* that can be varied from the center of the fiber to the core/cladding interface. Then the light was reflected back by the MMFBG, filtered by the SMF, and collected by an OSA (Advantest Q8384) through an SMF coupler.

Fig. 6.10 shows the transmission and reflection spectra of the MMFBG at different axial position *r*.

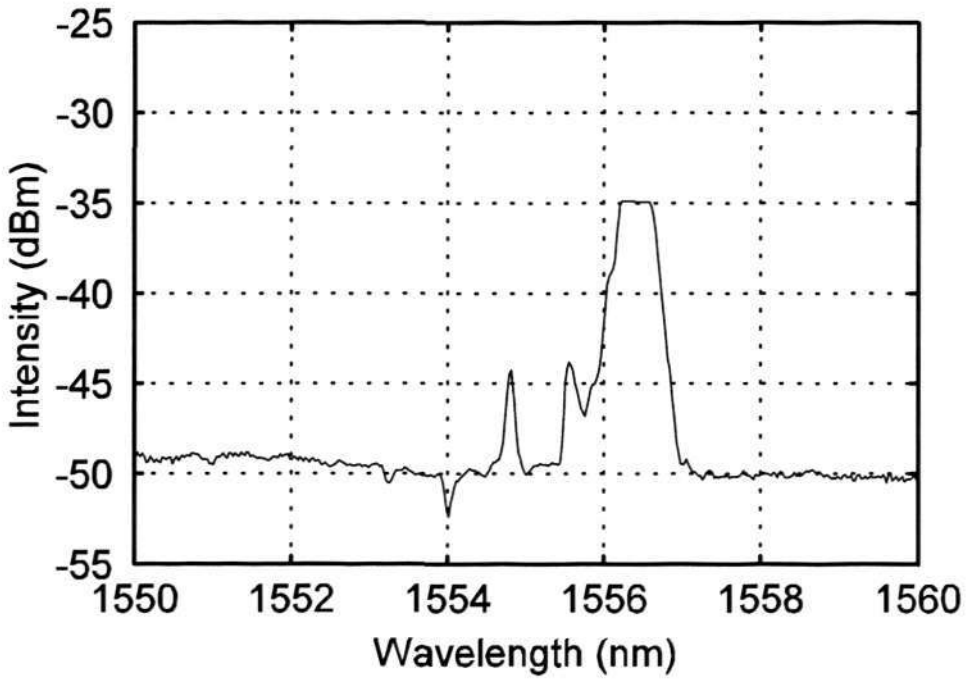

(a)

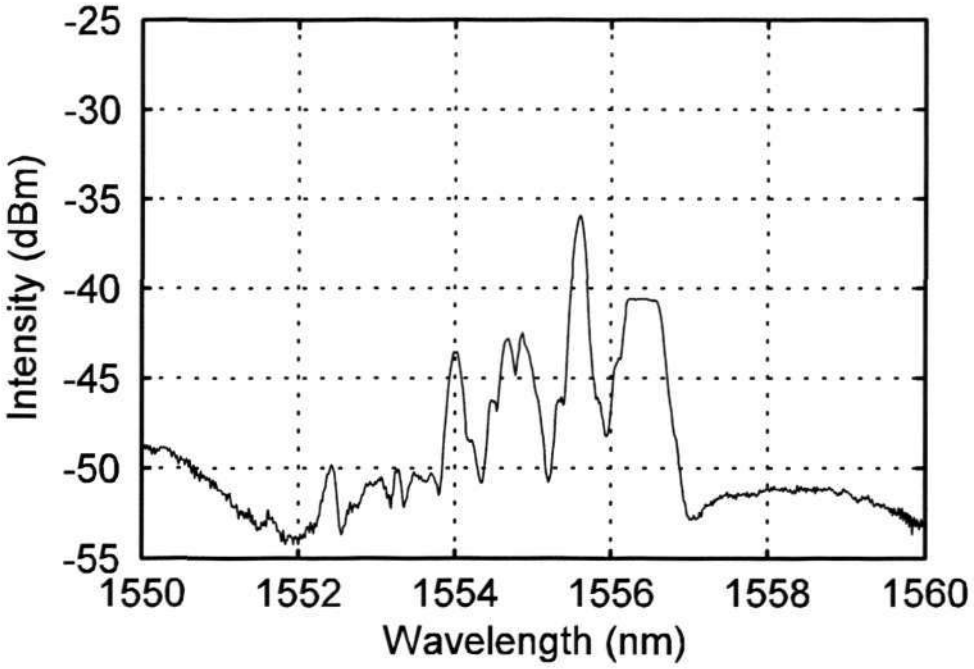

(b)

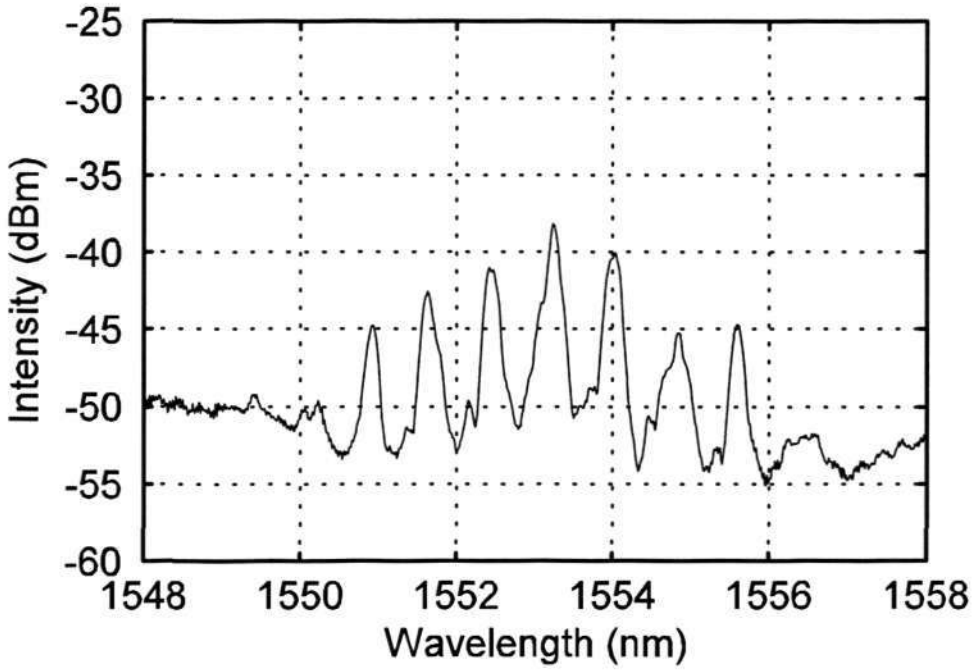

(c)

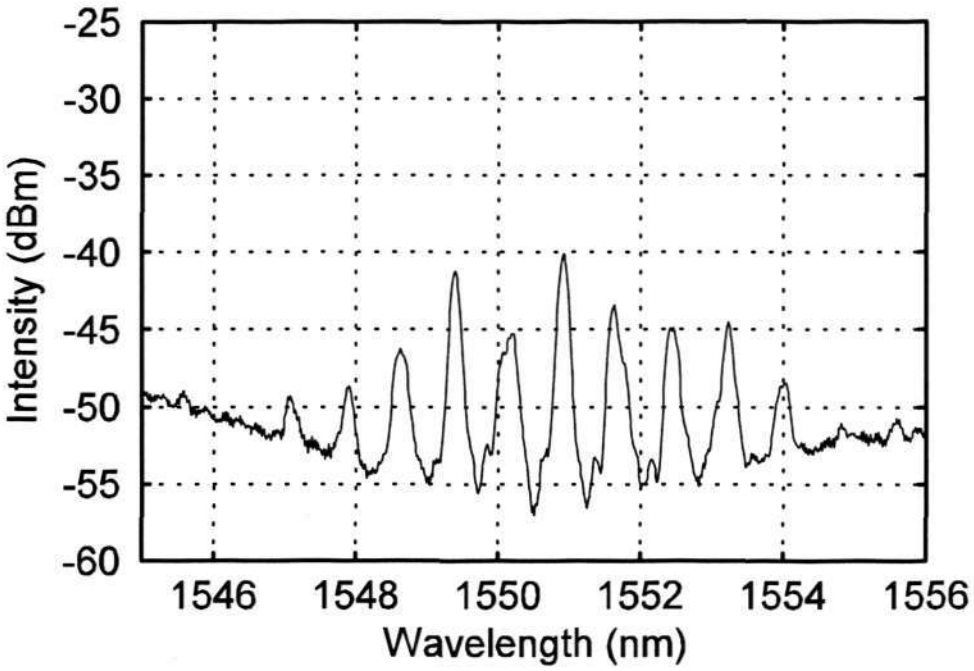

(d)

Fig. 6.10 Reflection spectra (dotted lines) of the MMFBG measured with 0.1nm resolution for different axial misalignments: (a) $r = 0$ μm; (b) $r = 3$ μm; (c) $r = 8$ μm; and (d) $r = 14$ μm

In Fig. 6.10 (a), by aligning the SMF to the MMF axis, three reflection peaks were observed having considerable reflectivity at 1556.43nm, 1555.58nm and 1554.78nm, respectively. At the axis-alignment condition, the fundamental mode was preferentially excited, and therefore was reflected by the MMFBG with the highest power. By increasing r, the axis-alignment condition was not satisfied any more. Therefore, a high-order mode can be excited preferentially instead of the fundamental mode. The order of the preferentially excited mode was exclusively determined by the launching position r, as was shown in Eq. (6.3). In Fig. 6.10 (b), at $r = 3$ μm, the reflection at λ_2 had the maximum reflectivity. By gradually increasing the r value to r

= 8 μm and r = 14 μm, in Fig. 6.10 (c) and (d), respectively, the fifth and eighth reflections were observed to have the strongest reflectivity.

6.4.2 Experimental results and discussions

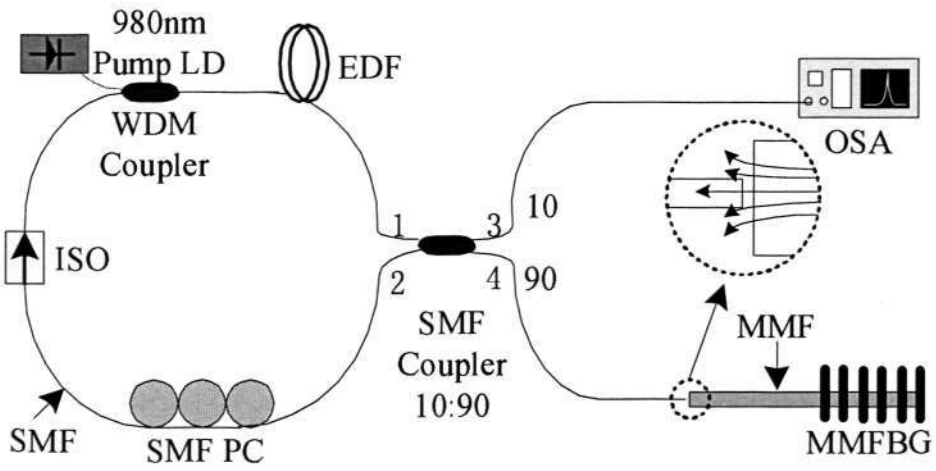

Fig. 6.11 Configuration of MMFBG based Erbium-doped fiber laser

Based on the above analysis, the alignment scheme for an MMFBG assisted wavelength-switchable EDFL was proposed, as shown in Fig. 6.11. Similar to the microbending scheme (Fig. 6.4), a 6 m section of highly concentrated erbium-doped fiber (EDF) (~1200 ppm) is optically pumped by the 980nm laser diode (LD) through a WDM fiber coupler. A 90:10 fused fiber coupler acts as a 10% output coupler for the ring laser cavity. The ISO ensures that the ring laser is unidirectional. A PC is used to control the polarization in the laser cavity. At the port 4 of the coupler, the SMF performs as a point-like beam source to launch the light to the MMF. They are

closely placed and in parallel in order to minimize the loss and the beam size launched into the MMF. The output (port 3 of the coupler) is measured using an OSA (Advantest Q8384).

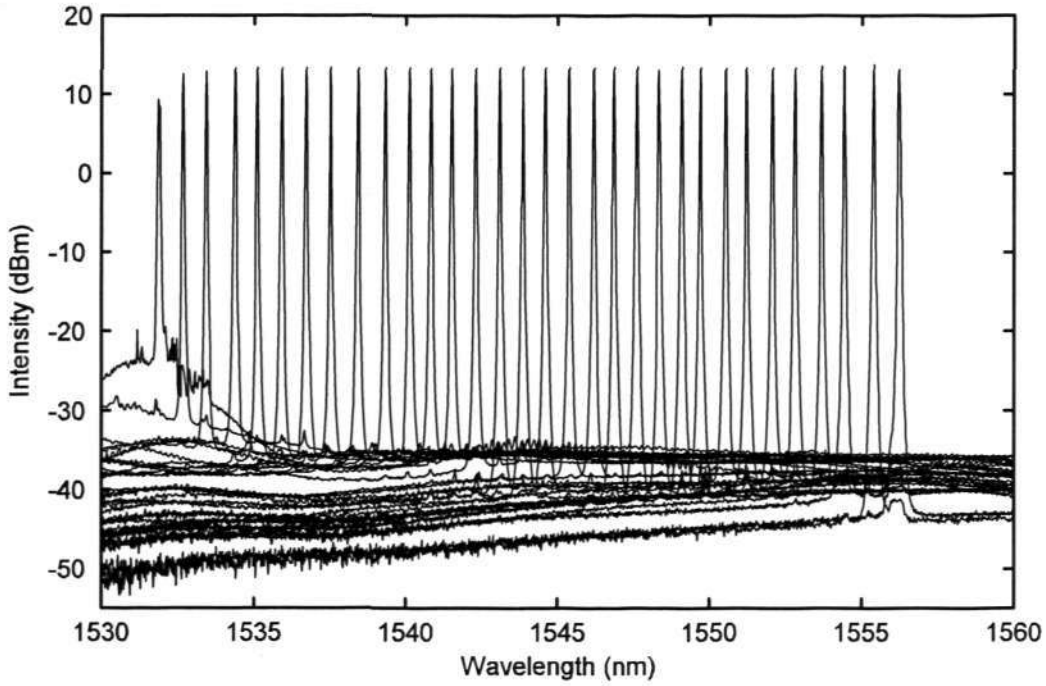

Fig. 6.12 Spectra of the wavelength-switchable EDFL at different lasing wavelengths measured with 0.05nm resolution

When the SMF was aligned to the axis of the MMF, a single-wavelength lasing at 1556.43nm was observed. By gradually increasing *r*, the lasing wavelength shifted to the short wavelength. The single-wavelength lasing was stabilized by exploiting the homogeneous gain broadening of the EDF at room temperature. The reflection peaks with low reflectivity were successfully suppressed and the reflection peak with the highest reflectivity determined the lasing wavelength. As was shown in Fig. 6.12, when the EDF was pumped with 60mW of 980nm LD, 32 discrete wavelengths

ranging from 1531.83nm to 1556.43nm at the output of the EDFL were obtained. The output peak power of the lasing from 1534.12nm to 1556.43nm was more than 20mw. But, the appreciable reduction of lasing peak power can be seen at 1533.35nm and eventually the lasing peak power was minimum at 1531.83nm (~8.46mw). No lasing was observed below 1531.83nm, because the position of the SMF approached the cladding region of the 62.5μm MMF and a significant amount of power was coupled to the cladding. Except for the lasing at 1531.83nm, more than 40dB of signal to ASE noise ratio was achieved for all the other wavelengths. It was observed that the lasing peak power was almost flat over a wide wavelength range owing to the gain saturation of the EDF [140]. The channel spacing between two adjacent lasing wavelengths was about 0.8nm. For those short lasing wavelengths, the ASE noise level was raised because of the increased power loss during the light transmission from the MMF to the SMF when the axial misalignment was increased. For 60mw pump power at 980nm, by maintaining the mode coupling condition in the MMF, the output lasing was found to be very stable, and no significant power and wavelength variation could be observed over a long period of time at room temperature.

The experimental results for the dependence of the preferentially excited mode on the launching position has been compared with the theoretical values calculated by Eq. (6.3), as was shown in Fig. 6.13.

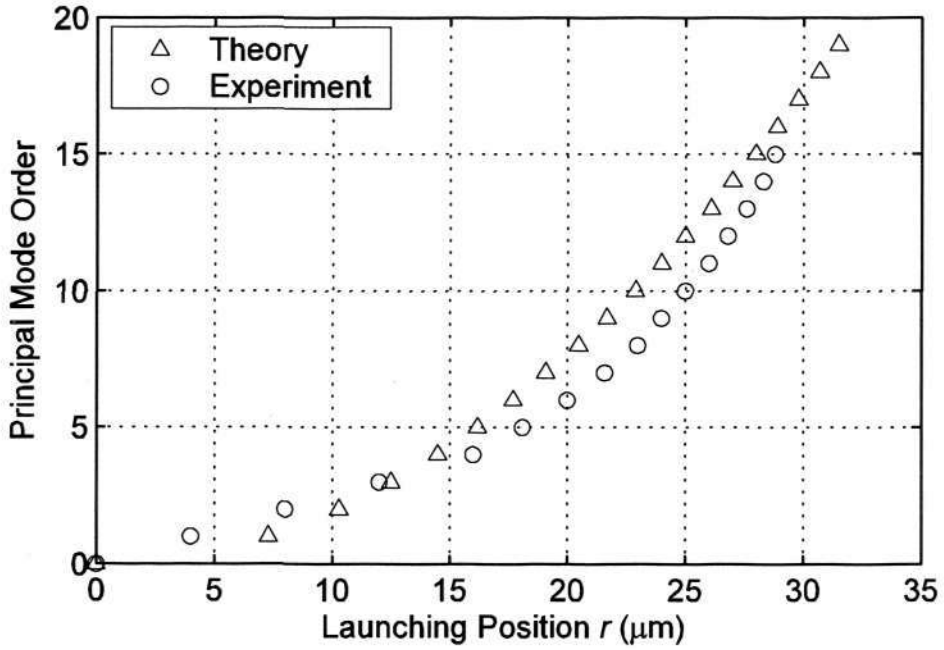

Fig. 6.13 Dependence of the mode order p of the preferentially excited mode on the launching position r

Very good agreement has been found between the theoretical calculations and the experimental results. It can be seen that the order of the preferentially excited mode increases when the launching position is moving towards the axis of the MMF. In a way the experimental results could be the justifications of the theory, where the order of preferentially excited mode and the modal power distribution can be observed clearly from both the lasing wavelength and the MMFBG reflection spectra. The slight difference between the experiment and theory is because, in the calculation, the Gaussian beam radius launched to the MMF was assumed to be the same as the spot radius of the fundamental mode w_0. In fact, the launched Gaussian beam radius should be larger than the spot size of the fundamental mode, as the gap between the SMF and

the MMF leads to considerable beam broadening and the spot size of the SMF would be larger than that of the fundamental mode. Therefore, in the experimental results shown in Fig. 6.13, a relatively small r value of ~4μm can lead to the preferentially excitation of the second order mode. Note that in Fig. 6.13 the reflections to those high-order preferentially excited modes near cutoff are unable to lead to lasing because a significant amount of power is coupled to the cladding when r has a large value. Extra lasing lines in Fig. 6.12 between adjacent principal modes are produced by the coupling of these two modes through the FBG, which are not shown in Fig. 6.13.

In both the configurations used to achieve wavelength switching, namely, the microbending scheme and the alignment scheme, the lasing was not in the purely single longitudinal mode. This was due to the degeneracy in the mode spectrum of the MMFBG and the long laser cavity led to multiple longitudinal modes. The lasing linewidth, however, was measured to be less than 0.06nm, and no wavelength variation was observed with the OSA. Therefore, it would meet the requirement of normal applications, and the multi-longitudinal mode lasing could be improved by employing proper lasing cavity designs. The repeatability of the wavelength-switching schemes was very good and the experimental results displayed good consistency

In comparison with other techniques that can be used to control the excitation of lasing modes [101, 139, 141-147], the two proposed schemes in this chapter have many advantages. First, wavelength switching is realized with a single MMFBG; second, a number of discrete lasing wavelengths are achieved over a wide wavelength range; third, all the lasing lines are almost equally spaced of ~0.8nm without being affected by the temperature change. The main disadvantage of the proposed schemes is the switching of lasing lines require a operation time, as both schemes are based on mechanically tuning methods.

6.5 Conclusions

In summary, this chapter presented the applications of the MMFBG in erbium-doped fiber lasers. Two schemes to achieve wavelength-switchable fiber lasers using MMFBG were demonstrated in this chapter. By using microbending and spatially launching techniques respectively to preferentially excite different order of mode, the reflection spectrum of MMFBG varied accordingly, which led to a single wavelength lasing at the selected wavelength. The dependence of modal power distribution on microbending displacement and launching position were analyzed theoretically and experimentally.

For both schemes, more than 30 discrete lasing lines have been obtained over a wide wavelength range (> 25 nm). The spacing of neighboring lasing was about 0.8

nm and was controllable according to the difference between propagation constants of adjacent modes. Single-wavelength lasing was successfully realized by exploiting the homogenous gain broadening of the erbium-doped fiber at room temperature.

The microbending scheme, employing periodic microbend to tune the modal power distribution in an MMF, modified the order of preferentially excited mode and the number of modes that were excited. Power reduction and an increased ASE noise were observed to be significant as a considerable amount of power were coupled to the radiation mode. Therefore an averaging signal to ASE noise ratio of ~30dB was obtained for all the lasing lines. For the alignment scheme, less power was coupled to the cladding modes, and therefore an averaging signal to ASE noise ratio of ~35dB was achieved for all lasing lines. The number of lasing lines obtained in our experiments for microbending scheme and alignment scheme were 31 and 32, respectively.

CHAPTER 7

CONCLUSIONS AND RECOMMENDED FUTURE WORKS

7.1 Conclusions

The goal of this dissertation was to study the periodic structures formed in GRIN MMF, which included FBGs, LPGs, and periodic microbending structures. The analysis relied upon the coupled-mode theory to obtain the conditions for phase matching of mode coupling along the periodic structures in GRIN MMF. The grating fabrication techniques, light transmission characteristics, and their potential applications in optical communications and optical fiber sensors were presented in detail.

Grating structures formed with laser irradiation were studied. The phase mask technique employing UV irradiation was used to fabricate the MMFBG. The spectral characteristics of MMFBG were analyzed, which confirmed that its spectral response could be varied by the change of the modal power distribution. Instead of using the UV method, the LPGs in GRIN MMFs studied in the thesis were fabricated with the CO_2 laser irradiation, which induced geometrical changes in the fiber and led to a

strong mode coupling. Their transmission characteristics were studied to confirm that strong mode couplings take place in the grating when the pitch of the grating is equal to the critical spatial period of the fiber. This critical spatial period was found to be wavelength independent.

Critical spatial period was used for the design of MMF LPGs for sensing applications. Such LPGs can give good sensitivities to strain and changes in the surrounding refractive index and therefore be used as effective physical and chemical sensors.

In order to look into the mode coupling mechanism at a periodic microbend, a theoretical model was developed for studying the microbend-induced mode coupling in a GRIN MMF. In particular, very simple analytical results were derived for a parabolic-profile MMF. For such a fiber, the fundamental mode can be coupled preferentially to a specific high-order mode at a microbend and the order of the dominantly coupled mode increases progressively as the amount of microbending increases.

This mirobending theory can be used for quantitative study of the function of a microbend-based mode scrambler that is commercially available. The MMFBG was used to measure the modal power distribution in order to confirm that the theoretical studies for a microbend-based mode scrambler. The experimental results from

measuring the near-field patterns of a GRIN MMF that was subjected to microbending as well as its reflection spectra from an FBG agreed well with the theoretical predictions.

The microbending theory should be also useful for the evaluation and design of microbend-based devices and sensors. An FBG-assisted microbend sensor consisting of the SMF leads at both the input and the output was proposed and demonstrated for simultaneous measurement of microbending displacement and temperature. The proposed sensor combined the advantages of an intensity-based sensor (simple configuration and low cost) and a wavelength-based sensor (absolute measurement and multiplexing capability). Two configurations were proposed for the implementation of the sensor with either a tunable filter in conjunction with a broadband source or a tunable laser.

The use of MMFBGs in the optical communications was proposed. The MMFBG was demonstrated effectively as reflectors to implement the wavelength-switchable fiber lasers in SMF systems. The ability of the uniform MMFBG to reflect different fiber modes at different wavelengths was utilized. Two wavelength-switching schemes have been proposed to select the lasing wavelength of the erbium-doped fiber laser using the MMFBG as the reflector. The first wavelength-switching scheme was achieved by taking advantage of our microbending theory, where the lasing wavelength was selected by tuning the microbending on a GRIN MMF. In the second

wavelength-switching scheme, the modal power distribution was modified by varying the alignment between the SMF and MMF. A large number of discrete lasing wavelengths have been successfully achieved with high signal to ASE noise ratio for both schemes. It is also believed that the MMFBG based wavelength-switchable fiber laser could be flexibly designed by employing proper grating and MMF parameters.

7.2 Recommended future work

The studies on the periodic structures in the MMF are still in the early stages as compared to the extensive research studies on the grating structures in the SMF. There are many avenues for the research presented in this dissertation to be extended in the future.

The theories for the grating structures in GRIN MMF need to be further elaborated. It should be noted that the mode couplings in the grating structures involve the coupling between modes in different orders. Therefore, it suggests that the index modulations or geometrical deformations along the grating are not uniform. In order to obtain the exact coupling coefficients of the coupling taking places between the modes in different orders, the further understanding of the non-uniform index/geometrical distribution along the grating region should be required. The integrity of the theory and the quantification of the performances for the multimode fiber gratings are suggested for future research.

One interesting question is that whether the periodic structures in MMF can be used in the MMF based transmission systems, as the MMF has been widely adopted in the local area networks and the ever-increasing demand on the transmission capacity is limited by the unavoidable intermodal dispersions in the MMF. By considering the fact that SMF gratings are playing an important role in SMF related telecommunication systems, the periodic structure in MMF has a great potential to be used for overcoming the bandwidth issue. The near field images presented in this thesis have already shown that the mode coupling and conversion effects induced by the periodic structure in a GRIN MMF. It may open the door for the enhancement of the transmission capacity of an MMF, as a number of studies have suggested that the excitation of a higher order mode rather than the fundamental mode in transmission will effectively enhance the product of bandwidth and distance of an MMF link [114-117].

One common issue that needs to be extended as the future work is the implementations of the sensing applications proposed in this thesis. In particular, a study of the effect of the fiber coating on the MMF used as a microbend sensor is expected, as the soft and thick coating of the fiber affects the performances of the GRIN MMF undergoing microbending. In addition, the packaging and integration techniques are also desirable for the sensors that have been presented.

Another topic for future research is to expand the study of period structure into other types of MMFs, including the step-index MMF and the polymer multimode optical fibers. It is expected that the properties of other kinds of MMF will lead to other interesting applications. In addition, it would also be interesting to look into other fabrication techniques, such as HF etching and side polishing.

APPENDIX A
MAXWELL'S EQUATIONS

In the International System of Units, Maxwell's equations are

$$\nabla \times \vec{E} = -\frac{\partial \vec{B}}{\partial t}, \tag{A.1}$$

$$\nabla \times \vec{H} = \vec{J} + \frac{\partial \vec{D}}{\partial t}, \tag{A.2}$$

$$\nabla \cdot \vec{D} = \rho_f, \tag{A.3}$$

$$\nabla \cdot \vec{B} = 0, \tag{A.4}$$

where $\vec{E}$ and $\vec{H}$ are electric and magnetic field vectors, respectively, and $\vec{D}$ and $\vec{B}$ are corresponding electric and magnetic flux densities. The current density vector $\vec{J}$ and the charge density ρ_f represent the sources for the electromagnetic field. In the absence of free charges in a medium such as optical fibers, $\vec{J} = 0$ and $\rho_f = 0$.

The flux densities $\vec{D}$ and $\vec{B}$ arise in response to the electric and magnetic field $\vec{E}$ and $\vec{H}$ propagating inside the medium and are related to them through the constitutive relations given by

$$\vec{D} = \varepsilon_0 \vec{E} + \vec{P}, \tag{A.5}$$

$$\vec{B} = \mu_0 \vec{H} + \vec{M}. \tag{A.6}$$

where ε_0 is the vacuum permittivity, μ_0 is the vacuum permeability, and $\vec{P}$ and $\vec{M}$ are the induced electric and magnetic polarizations. For a nonmagnetic medium such as optical fibers, $\vec{M} = 0$.

AUTHOR'S PUBLICATIONS

This research work has led to the publications of 6 journal papers and 2 conference papers.

1. **L. Su** and C. Lu, "Wavelength-switching fibre laser based on multimode fibre Bragg gratings," Electronics Letters, vol. 41, pp. 11-13, 2005. (related to Chapters 3 and 6)

2. **L. Su**, C. Lu, J. Z. Hao, Z. H. Li, and Y. X. Wang, "Design of wavelength-switching erbium-doped fiber lasers with a multimode fiber Bragg grating using spatial-mode excitation and selection techniques," IEEE Photonics Technology Letters, vol. 17, pp. 315-317, 2005. (related to Chapters 3 and 6)

3. **L. Su**, K. S. Chiang, and C. Lu, "Microbend-induced mode coupling in a graded-index multimode fiber," Applied Optics, Vol. 44, No. 34, pp. 7394-7402, Dec 2005. (related to Chapters 5 and 6)

4. **L. Su**, K. S. Chiang, and C. Lu, "Fiber-Bragg-Grating Incorporated Microbend Sensor for Simultaneous Mechanical-Parameter and Temperature Measurement," IEEE Photonics Technology Letters, Vol. 17, No. 12, pp. 2697-2699, Dec, 2005. (related to Chapter 5)

5. **L. Su**, K. S. Chiang, and C. Lu, "CO_2-laser induced long-period gratings in graded-index multimode fibers for sensor applications," IEEE Photonics Technology Letters, Vol. 18, No. 1, pp. 190-192, Jan,2006. (related to Chapter 4)

6. X. Dong, **L. Su**, P. Shum, Y. Chung, and C.C. Chan, "Wavelength-selective all-fiber filter based on a single long-period fiber grating and a misaligned splicing point," Optics Communications, Vol. 258, pp. 159-163, 2006. (related to Chapter 6)

7. **L. Su** and C. Lu, "Multimode fiber Bragg grating based fiber lasers and optical sensors," Optical Fiber Communications Conference (OFC) 2005. (related to Chapters 3 and 6)

8. **L. Su**, C. Lu, and K. S. Chiang, "CO_2-laser fabricated long-period grating sensors in graded-index multimode fibers," Optical Fiber Communications Conference (OFC) 2006. (related to Chapter 4)

REFERENCES

[1] K. O. Hill and G. Meltz, "Fiber Bragg grating technology fundamentals and overview," *Journal of Lightwave Technology*, vol. 15, pp. 1263 - 1276, 1997.

[2] A. D. Kersey, M. A. Davis, H. J. Patrick, M. LeBlanc, K. P. Koo, C. G. Askins, M. A. Putnam, and E. J. Friebele, "Fiber grating sensors," *Journal of Lightwave Technology*, vol. 15, pp. 1442-1463, 1997.

[3] I. K. Hwang, S. H. Yun, and B. Y. Kim, "Long-period fiber gratings based on periodic microbends," *Optics Letters*, vol. 24, pp. 1263-1265, 1999.

[4] S. H. Yun, I. K. Hwang, and B. Y. Kim, "All-fiber tunable filter and laser based on two-mode fiber," *Optics Letters*, vol. 21, pp. 27-29, 1996.

[5] J. L. Zyskind, J. W. Sulhoff, P. D. Magill, K. C. Reichmann, V. Mizrahi, and D. J. DiGiovanni, "Transmission at 2.5 Gbit/s over 654 km using an erbium-doped fiber grating laser source," *Electronics Letters*, vol. 29, pp. 1105, 1993.

[6] C. R. Giles, "Lightwave applications of fiber Bragg gratings," *Journal of Lightwave Technology*, vol. 15, pp. 1391-1404, 1997.

[7] C. R. Giles, T. Erdogan, and V. Mizrahi, "Reflection-induced changes in the optical spectra of 980-nm QW lasers," *IEEE Photonics Technology Letters*, vol. 6, pp. 903-906, 1994.

[8] P. B. Hansen, L. Eskildsen, S. G. Grubb, A. M. Vengsarkar, S. K. Korotky, T. A. Strasser, J. E. J. Alphonsus, J. J. Veselka, D. J. DiGiovanni, D. W. Peckham, D. Truxal, W. Y. Cheung, S. G. Kosinski, and P. F. Wysocki, "Unrepeatered WDM transmission experiment with 8 channels of 10 Gb/s over 352 km," *IEEE Photonics Technology Letters*, vol. 8, pp. 1082-1084, 1996.

[9] C. R. Giles, V. Mizrahi, and T. Erdogan, "Polarization-independent phase conjugation in a reflective optical mixer," *IEEE Photonics Technology Letters*, vol. 7, pp. 126-128, 1995.

[10] F. Forghieri, R. W. Tkach, A. R. Chraplyvy, and D. Marcuse, "Reduction of four-wave mixing crosstalk in WDM systems using unequally spaced channels," *IEEE Photonics Technology Letters*, vol. 6, pp. 754-756, 1994.

[11] V. Mizrahi, T. Erdogan, D. J. DiGiovanni, P. J. Lemaire, W. M. MacDonald, S. G. Kosinski, S. Cabot, and J. E. Sipe, "Four channel fibre grating

demultiplexer," *Electronics Letters*, vol. 30, pp. 780-781, 1994.

[12] R. J. Nuyts, Y. K. Park, and P. Gallion, "Dispersion equalization of a 10 Gb/s repeatered transmission system using dispersion compensating fibers," *Journal of Lightwave Technology*, vol. 15, pp. 31-42, 1997.

[13] F. Ouellette, "Dispersion cancellation using linearly chirped Bragg grating filters in optical waveguides," *Optics Letters*, vol. 12, pp. 847-849, 1987.

[14] W. W. Morey, G. Meltz, and W. H. Glenn, "Fiber optic Bragg grating sensors," *Proc. SPIE*, vol. 1169, pp. 98-107, 1989.

[15] Y. J. Rao, "In-fibre Bragg grating sensors," *Meas. Sci. Technol.*, vol. 8, pp. 355-375, 1997.

[16] X. W. Shu, K. Chisholm, I. Felmeri, K. Sugden, A. Gillooly, L. Zhang, and I. Bennion, "Highly sensitive transverse load sensing with reversible sampled fiber Bragg gratings," *Applied Physics Letters*, vol. 83, pp. 3003-3005, 2003.

[17] A. Iadicicco, S. Campopiano, A. Cutolo, M. Giordano, and A. Cusano, "Nonuniform Thinned Fiber Bragg Gratings for Simultaneous Refractive Index and Temperature Measurements," *IEEE Photonics Technology Letters*, vol. 17, pp. 1495-1497, 2005.

[18] A. M. Vengsarkar, P. J. Lemaire, J. B. Judkins, V. Bhatia, T. Erdogan, and J. E. Sipe, "Long-period fiber gratings as band-rejection filters," *Journal of Lightwave Technology*, vol. 14, pp. 58-65, 1996.

[19] A. M. Vengsarkar, J. R. Pedrazzani, J. B. Judkins, P. J. Lemaire, N. S. Bergano, and C. R. Davidson, "Long-period fiber-grating-based gain equalizers," *Optics Letters*, vol. 21, pp. 336-338, 1996.

[20] V. Bhatia and A. M. Vengsarkar, "Optical fiber long-period grating sensors," *Optics Letters*, vol. 21, pp. 692-694, 1996.

[21] H. J. Patrick, C. C. Chang, and S. T. Vohra, "Long period fibre gratings for structural bend sensing," *Electronics Letters*, vol. 34, pp. 1773-1775, 1998.

[22] H. J. Patrick, A. D. Kersey, and F. Bucholtz, "Analysis of the response of long period fiber gratings to external index of refraction," *Journal of Lightwave Technology*, vol. 16, pp. 1606-1612, 1998.

[23] H. J. Patrick, G. M. Williams, A. D. Kersey, J. R. Pedrazzani, and A. M. Vengsarkar, "Hybrid fiber Bragg grating/long period fiber grating sensor for strain/temperature discrimination," *IEEE Photonics Technology Letters*, vol. 8, pp. 1223-1225, 1996.

[24] Y. Liu, L. Zhang, J. A. R. Williams, and I. Bennion, "Optical bend sensor based on measurement of resonance mode splitting of long-period fiber grating," *IEEE Photonics Technology Letters*, vol. 12, pp. 531-533, 2000.

[25] V. Bhatia, D. Campbell, R. O. Claus, and A. M. Vengsarkar, "Simultaneous strain and temperature measurement with long-period gratings," *Optics Letters*, vol. 22, pp. 648-650, 1997.

[26] M. N. Ng, Z. Chen, and K. S. Chiang, "Temperature compensation of long-period fiber grating for refractive-index sensing with bending effect," *IEEE Photonics Technology Letters*, vol. 14, pp. 361-362, 2002.

[27] I. B. Sohn, J. G. Baek, N. K. Lee, H. W. Kwon, and J. W. Song, "Gain flattened and improved EDFA using microbending long-period fibre gratings," *Electronics Letters*, vol. 38, pp. 1324-1325, 2002.

[28] J. N. Blake, B. Y. Kim, and H. J. Shaw, "Fiber-optic modal coupler using periodic microbending," *Optics Letters*, vol. 11, pp. 177-179, 1986.

[29] J. H. Lim, K. S. Lee, J. C. Kim, and B. H. Lee, "Tunable fiber gratings fabricated in photonic crystal fiber by use of mechanical pressure," *Optics Letters*, vol. 29, pp. 331-333, 2004.

[30] V. Arya, K. A. Murphy, A. Wang, and R. O. Claus, "Microbend losses in singlemode optical fibers: theoretical and experimental investigation," *Journal of Lightwave Technology*, vol. 13, pp. 1998-2002, 1995.

[31] G. Meltz, W. W. Morey, and W. H. Glenn, "Formation of Bragg gratings in optical fibers by a transverse holographic method," *Optics Letters*, vol. 14, pp. 823-825, 1989.

[32] T. Mizunami, T. V. Djambova, T. Niiho, and S. Gupta, "Bragg gratings in multimode and few-mode optical fibers," *Journal of Lightwave Technology*, vol. 18, pp. 230-235, 2000.

[33] S. T. Lee, R. D. Kumar, P. S. Kumar, P. Radhakrishnan, C. P. G. Vallabhan, and V. P. N. Nampoori, "Long period gratings in multimode optical fibers: application in chemical sensing," *Optics Communications*, vol. 224, pp. 237-241, 2003.

[34] V. V. Namboodiri, A. V. Scaria, V. P. N. Nampoori, V. M. Nandakumaran, and P. Radhakrishnan, "Refractive Index Measurement using Multimode Fibers with long period grating," *Proc. of SPIE*, vol. 5459, pp. 415-419, 2004.

[35] K. J. Grant, A. Roberts, D. N. Jamieson, C. Cher, and B. Rout, "Long period gratings in multimode fiber fabricated with high-energy ion implantation," *Fiber and Integrated Optics*, vol. 22, pp. 225-237, 2003.

[36] M. Viziri and C.-L. Chen, "Etched fibers as strain gauges," *Applied Optics*, vol. 10, pp. 836-841, 1992.

[37] D. D. Davis, T. K. Gaylord, E. N. Glytsis, S. G. Kosinski, S. C. Mettler, and A. M. Vengsarkar, "Long-period fibre grating fabrication with focused CO_2 laser pulses," *Electronics Letters*, vol. 34, pp. 302-303, 1998.

[38] J. N. Fields and J. H. Cole, "Fiber microbend acoustic sensor," *Applied Optics*, vol. 19, pp. 3265-3267, 1980.

[39] N. Lagakos, J. H. Cole, and J. A. Bucaro, "Microbend fiber-optic sensor," *Applied Optics*, vol. 26, pp. 2171-2180, 1987.

[40] J. W. Berthold, "Historical review of microbend fiber-optic sensors," *Journal of Lightwave Technology*, vol. 13, pp. 1193-1199, 1995.

[41] J. Berthold, W. Ghering, and D. Varshneya, "Design and characterization of a high temperature fiber-optic pressure transducer," *Journal of Lightwave Technology*, vol. 5, pp. 870-876, 1987.

[42] R. Olshansky, "Mode coupling effects in graded-index optical fibers," *Applied Optics*, vol. 14, pp. 935-945, 1975.

[43] H. F. Taylor, "Power loss at directional change in dielectric waveguides," *Applied Optics*, vol. 13, pp. 642-647, 1974.

[44] H. F. Taylor, "Losses at corner bends in dielectric waveguides," *Applied Optics*, vol. 16, pp. 711-716, 1977.

[45] H. F. Taylor, "Bending effects in optical fibers," *Journal of Lightwave Technology*, vol. LT-2, pp. 617-628, 1984.

[46] A. W. Snyder and J. D. Love, *Optical waveguide theory*. London ; New York: Chapman and Hall, 1983.

[47] M.-Y. Loke and J. N. McMullin, "Simulation and measurement of radiation loss at multimode fiber macrobends," *Journal of Lightwave Technology*, vol. 8, pp. 1250-1256, 1990.

[48] D. Donlagic and M. Zavrsnik, "Fiber-optic microbend sensor structure," *Optics Letters*, vol. 22, pp. 837-839, 1997.

[49] G. P. Agawal, *Fiber-Optic Communications Systems*, Third ed. New York: John Wiley & Sons, 2002.

[50] G. Keiser, *Optical fiber communications*, 3rd ed. Boston: McGraw-Hill, 2000.

[51] A. Yariv, *Optical electronics in modern communications*, 5th ed. New York:

Oxford University Press, 1997.

[52] J. Gowar, *Optical communication systems*, 2nd ed. New York: Prentice Hall, 1993.

[53] D. Gloge and E. A. J. Marcatili, "Multimode theory of graded-core fibers," *Bell System Technical Journal*, vol. 52, pp. 1563-1578, 1973.

[54] S. Kawakami and T. Nishizawa, "An optical waveguide with the optimum distribution of the refractive index with reference to waveform distortion," *IEEE Trans. Microwave Theory and Tech.*, vol. MTT-16, pp. 814-818, 1968.

[55] C. N. Kurtz and W. Streifer, "Guided Waves in Inhomogeneous Focusing Media Part I: Formulation, Solution for Quadratic Inhomogeneity," *IEEE Trans. Microwave Theory and Tech.*, vol. 17, pp. 11-15, 1969.

[56] G. L. Yip and S. Nemoto, "The Relations Between Scalar Modes in a Lenslike Medium and Vector Modes in a Self-Focusing Optical Fiber," *IEEE Trans. Microwave Theory and Tech.*, vol. 23, pp. 260- 263, 1975.

[57] J. Saijonmaa, A. B. Sharma, and S. J. Halme, "Selective excitation of parabolic-index optical fibers by Gaussian beams," *Applied Optics*, vol. 19, pp. 2442-2452, 1980.

[58] O. Katsunari, *Fundamentals of Optical Waveguides*. San Diego: Academic Press, 2000.

[59] "Transverse mode," in *http://www.physicsdaily.com/physics/Transverse_mode:* Physics Daily, 2005.

[60] E. Zauderer, "Complex argument Hermite-Gaussian and Laguerre-Gaussian beams," *Journal of the Optical Society of America A*, vol. 3, pp. 465-469, 1986.

[61] A. E. Siegman, "Hermite-Gaussian functions of complex argument as optical-beam eigenfunctions," *Journal of the Optical Society of America A*, vol. 63, pp. 1093-1094, 1973.

[62] D. Marcuse, *Theory of Dielectric Optical Waveguides*, 2nd ed: Academic Press, 1991.

[63] D. Gloge, "Optical power flow in multimode fibers," *Bell System Technical Journal*, vol. 51, pp. 1767-1783, 1972.

[64] L. Jeunhomme and J. P. Pocholle, "Mode coupling in a multimode optical fiber with microbends," *Applied Optics*, vol. 14, pp. 2400-2405, 1975.

[65] K. O. Hill, Y. Fujii, D. C. Johnson, and B. S. Kawasaki, "Photosensitivity in

optical fiber waveguides: Application to reflection filter fabrication," *Applied Physics Letters*, vol. 32, pp. 647-649, 1978.

[66] R. Kashyap, *Fiber Bragg gratings*. San Diego: Academic Press, 1999.

[67] D. K. W. Lam and B. K. Garside, "Characterization of single-mode optical fiber filters," *Applied Optics*, vol. 20, pp. 440-445, 1981.

[68] K. O. Hill, B. Malo, F. Bilodeau, D. C. Johnson, and J. Albert, "Bragg Gratings Fabricated in Monomode Photosensitive Optical Fiber by Uv Exposure through a Phase Mask," *Applied Physics Letters*, vol. 62, pp. 1035-1037, 1993.

[69] B. H. Kim, Y. Park, T.-J. Ahn, D. Y. Kim, B. H. Lee, Y. Chung, U. C. Paek, and W.-T. Han, "Residual stress relaxation in the core of optical fiber by CO_2 laser irradiation," *Optics Letters*, vol. 26, pp. 1657-1659, 2001.

[70] G. Kakarantzas, T. E. Dimmick, T. A. Birks, R. L. Roux, and P. S. J. Russell, "Miniature all-fiber devices based on CO_2 laser micro structuring of tapered fibers," *Optics Letters*, vol. 26, pp. 1137-1139, 2001.

[71] J. N. Fields, C. K. Asawa, O. G. Ramer, and M. K. Barnoski, "Fiber optic pressure sensor," *Journal of the Acoustical Society of America*, vol. 67, pp. 816-818, 1980.

[72] G. Oscroft, "Intrisic fibre optic sensors," presented at International Conference on Fibre Optics and Opto-Electronics, London, UK, 1987.

[73] S. J. Mihailov, C. W. Smelser, P. Lu, R. B. Walker, D. Grobnic, H. M. Ding, G. Henderson, and J. Unruh, "Fiber Bragg gratings made with a phase mask and 800-nm femtosecond radiation," *Optics Letters*, vol. 28, pp. 995-997, 2003.

[74] K. M. Davis, K. Miura, N. Sugimoto, and K. Hirao, "Writing waveguides in glass with a femtosecond laser," *Optics Letters*, vol. 21, pp. 1729-1731, 1996.

[75] Y. Kondo, K. Nouchi, T. Mitsuyu, M. Watanabe, P. G. Kazansky, and K. Hirao, "Fabrication of long-period fiber gratings by focused irradiation of infrared femtosecond laser pulses," *Optics Letters*, vol. 24, pp. 646-648, 1999.

[76] M. L. von Bibra, A. Roberts, and J. Canning, "Fabrication of long-period fiber gratings by use of focused ion-beam irradiation," *Optics Letters*, vol. 26, pp. 765-767, 2001.

[77] M. Vaziri and C. L. Chen, "Etched Fibers as Strain-Gauges," *Journal of Lightwave Technology*, vol. 10, pp. 836-841, 1992.

[78] M. Vaziri and C. L. Chen, "Optical-Fiber Strain Sensors with Asymmetric

Etched Structures," *Applied Optics*, vol. 32, pp. 6399-6406, 1993.

[79] R. J. Bartlett, R. Philip-Chandy, P. Eldridge, D. F. Merchant, R. Morgan, and P. J. Scully, "Plastic optical fibre sensors and devices," *Transactions of the Institute of Measurement and Control*, vol. 22, pp. 431-457, 2000.

[80] K. H. Wanser, K. F. Voss, and A. D. Kersey, "Novel fiber devices and sensors based on multimode fiber Bragg gratings," presented at Proc. SPIE, 1994.

[81] H. G. Yu, C. Q. Xu, Y. Wang, J. Wojcik, Z. L. Peng, and P. Mascher, "External-cavity semiconductor laser with Bragg grating in multimode fiber," *IEEE Photonics Technology Letters*, vol. 16, pp. 2341-2343, 2004.

[82] T. Mizunami, T. Hamada, and T. Yamamoto, "External-fiber-grating vertical-cavity surface-emitting lasers," *IEEE Photonics Technology Letters*, vol. 12, pp. 1558-1560, 2000.

[83] W. Zhao and R. O. Claus, "Optical fiber grating sensors in multimode fibers," *Smart Materials & Structures*, vol. 9, pp. 212-214, 2000.

[84] A. D. Kersey, M. A. Davis, H. J. Patrick, M. LeBlanc, K. P. Koo, C. G. Askins, M. A. Putnam, and E. J. Friebele, "Fiber grating sensors," *Journal of Lightwave Technology*, vol. 15, pp. 1442-1463, 1997.

[85] J. N. Fields, "Attenuation of a parabolic-index fiber with periodic beads," *Applied Physics Letters*, vol. 36, pp. 799-801, 1980.

[86] D. Donlagic and B. Culshaw, "Microbend sensor structure for use in distributed and quasi-distributed sensor systems based on selective launching and filtering of the modes in graded index multimode fiber," *Journal of Lightwave Technology*, vol. 17, pp. 1856-1868, 1999.

[87] T. Lee, N. A. George, G. P. Sureshkumar, P. Radhakrishnan, C. P. G. Vallabhan, and V. P. N. Nampoori, "Chemical sensing with microbent optical fiber," *Optics Letters*, vol. 26, pp. 1541-1543, 2001.

[88] X. F. Yang, C. L. Zhao, J. Q. Zhou, X. Guo, J. H. Ng, X. Q. Zhou, and C. Lu, "The characteristics of fiber slanted gratings in multimode fiber," *Optics Communications*, vol. 229, pp. 161-165, 2004.

[89] T. Erdogan, "Cladding-mode resonances in short- and long-period fiber grating filters," *Journal of the Optical Society of America a-Optics Image Science and Vision*, vol. 14, pp. 1760-1773, 1997.

[90] T. Erdogan, "Fiber grating spectra," *Journal of Lightwave Technology*, vol. 15, pp. 1277-1294, 1997.

[91] S. Takahashi and S. Shibata, "Thermal variation of attenuation for optical fibers," *J. Non-Cryst. Solids*, vol. 30, pp. 359-370, 1979.

[92] D. Grobnic, S. J. Mihailov, C. W. Smelser, and H. Ding, "Sapphire fiber Bragg grating sensor made using femtosecond laser radiation for ultrahigh temperature applications," *IEEE Photonics Technology Letters*, vol. 16, pp. 2505-2507, 2004.

[93] A. Martin, R. Badcock, C. Nightingale, and G. F. Fernando, "A novel optical fiber-based strain sensor," *IEEE Photon. Technol. Lett.*, vol. 9, pp. 982-984, 1997.

[94] S. P. Guo and S. Albin, "Transmission property and evanescent wave absorption of cladded multimode fiber tapers," *Optics Express*, vol. 11, pp. 215-223, 2003.

[95] J. Villatoro, D. Monzon-Hernandez, and D. Luna-Moreno, "In-line optical fiber sensors based on cladded multimode tapered fibers," *Applied Optics*, vol. 43, pp. 5933-5938, 2004.

[96] J. Villatoro, D. Monzon-Hernandez, and D. Talavera, "High resolution refractive index sensing with cladded multimode tapered optical fibre," *Electronics Letters*, vol. 40, pp. 106-107, 2004.

[97] X. F. Chen, K. M. Zhou, L. Zhang, and I. Bennion, "Optical chemsensor based on etched tilted Bragg grating structures in multimode fiber," *IEEE Photonics Technology Letters*, vol. 17, pp. 864-866, 2005.

[98] D. Donlagic and B. Culshaw, "Microbend sensor structure for use in distributed and quasi-distributed sensor systems based on selective launching and filtering of the modes in graded index multimode fiber," *Journal of Lightwave Technology*, vol. 17, pp. 1856-1868, 1999.

[99] D. Donlagic and B. Culshaw, "Propagation of the fundamental mode in curved graded index multimode fiber and its application in sensor systems," *Journal of Lightwave Technology*, vol. 18, pp. 334-342, 2000.

[100] O. G. Okhotnikov, T. Jouhti, J. Konttinen, S. Karirinne, and M. Pessa, "1.5-mu m monolithic GaInNAs semiconductor saturable-absorber mode locking of an erbium fiber laser," *Optics Letters*, vol. 28, pp. 364-366, 2003.

[101] Q. H. Mao and J. W. Y. Lit, "Switchable multiwavelength erbium-doped fiber laser with cascaded fiber grating cavities," *IEEE Photonics Technology Letters*, vol. 14, pp. 612-614, 2002.

[102] G. E. Town, L. Chen, and P. W. E. Smith, "Dual wavelength modelocked fiber laser," *IEEE Photonics Technology Letters*, vol. 12, pp. 1459-1461, 2000.

[103] J. Daniel, J. M. Costa, P. LeBoudec, G. Stephan, and F. Sanchez, "Generalized bistability in an erbium-doped fiber laser," *Journal of the Optical Society of America B-Optical Physics*, vol. 15, pp. 1291-1294, 1998.

[104] Y. Z. Xu, H. Y. Tam, W. C. Du, and M. S. Demokan, "Tunable dual-wavelength-switching fiber grating laser," *IEEE Photonics Technology Letters*, vol. 10, pp. 334-336, 1998.

[105] J. Chow, G. Town, B. Eggleton, M. Ibsen, K. Sugden, and I. Bennion, "Multiwavelength generation in an erbium-doped fiber laser using in-fiber comb filters," *IEEE Photonics Technology Letters*, vol. 8, pp. 60-62, 1996.

[106] E. Lacot, F. Stoeckel, and M. Chenevier, "Dynamics of an Erbium-Doped Fiber Laser," *Physical Review A*, vol. 49, pp. 3997-4008, 1994.

[107] J. L. Zyskind, V. Mizrahi, D. J. Digiovanni, and J. W. Sulhoff, "Short Single Frequency Erbium-Doped Fiber Laser," *Electronics Letters*, vol. 28, pp. 1385-1387, 1992.

[108] N. Park, J. W. Dawson, and K. J. Vahala, "Multiple Wavelength Operation of an Erbium-Doped Fiber Laser," *IEEE Photonics Technology Letters*, vol. 4, pp. 540-541, 1992.

[109] E. Yoshida, Y. Kimura, and M. Nakazawa, "Laser Diode-Pumped Femtosecond Erbium-Doped Fiber Laser with a Sub-Ring Cavity for Repetition Rate Control," *Applied Physics Letters*, vol. 60, pp. 932-934, 1992.

[110] J. L. Zyskind, J. W. Sulhoff, Y. Sun, J. Stone, L. W. Stulz, G. T. Harvey, D. J. Digiovanni, H. M. Presby, A. Piccirilli, U. Koren, and R. M. Jopson, "Singlemode Diode-Pumped Tunable Erbium-Doped Fiber Laser with Linewidth Less Than 5.5khz," *Electronics Letters*, vol. 27, pp. 2148-2149, 1991.

[111] N. Park and P. F. Wysocki, "24-line multiwavelength operation of erbium-doped fiber-ring laser," *IEEE Photonics Technology Letters*, vol. 8, pp. 1459-1461, 1996.

[112] N. Park, J. W. Dawson, K. J. Vahala, and C. Miller, "All Fiber, Low Threshold, Widely Tunable Single-Frequency, Erbium-Doped Fiber Ring Laser with a Tandem Fiber Fabry-Perot Filter," *Applied Physics Letters*, vol. 59, pp. 2369-2371, 1991.

[113] E. Desurvire, J. L. Zyskind, and J. R. Simpson, "Spectral gain hole-burning at 1.53 μm in erbium-doped fiber amplifiers," *IEEE Photonics Technology Letters*, vol. 2, pp. 246-248, 1990.

[114] L. Raddatz, I. H. White, D. G. Cunningham, and M. C. Nowell, "Increasing the

bandwidth-distance product of multimode fibre using offset launch," *Electronics Letters*, vol. 33, pp. 232-233, 1997.

[115] L. Raddatz, I. H. White, D. G. Cunningham, and M. C. Nowell, "Influence of restricted mode excitation on bandwidth of multimode fiber links," *IEEE Photonics Technology Letters*, vol. 10, pp. 534-536, 1998.

[116] L. Raddatz, I. H. White, D. G. Cunningham, and M. C. Nowell, "An experimental and theoretical study of the offset launch technique for the enhancement of the bandwidth of multimode fiber links," *Journal of Lightwave Technology*, vol. 16, pp. 324-331, 1998.

[117] M. Webster, L. Raddatz, I. H. White, and D. G. Cunningham, "A statistical analysis of conditioned launch for gigabit ethernet links using multimode fiber," *Journal of Lightwave Technology*, vol. 17, pp. 1532-1541, 1999.

[118] L. Jeunhomme and J. P. Pocholle, "Selective mode excitation of graded index optical fibers," *Applied Optics*, vol. 17, pp. 463-468, 1978.

[119] E. Snitzer and R. Woodcock, "Y_b^{3+}-E_r^{3+} glass laser," *Applied Physics Letters*, vol. 6, pp. 45-46, 1965.

[120] E. Snitzer, "Glass lasers," *Applied Optics*, vol. 5, pp. 1487-1499, 1966.

[121] J. Hegarty, M. M. Broer, B. Golding, J. R. Simpson, and J. B. MacChesney, "Photon Echoes below 1 K in a Nd^{3+}-Doped Glass Fiber," *Applied Physics Letters*, vol. 51, pp. 2033-2035, 1983.

[122] S. B. Poole, D. N. Payne, and M. E. Fermann, "Fabrication of low-loss optical fibres containing rare-earth ions," *Electronics Letters*, vol. 21, pp. 737-738, 1985.

[123] R. J. Mears, L. Reekie, I. M. Jauncey, and D. N. Payne, "Low-Noise Erbium-Doped Fiber Amplifier Operating at 1.54μm," *Electronics Letters*, vol. 23, pp. 1026-1028, 1987.

[124] E. Desurvire, J. R. Simpson, and P. C. Becker, "High-gain erbium-doped traveling-wave fiber amplifier," *Optics Letters*, vol. 12, pp. 888-890, 1987.

[125] M. Nakazawa, Y. Kimura, and K. Suzuki, "Efficient Er^{3+}-doped optical fiber amplifier pumped by a 1.48μm InGaAsP laser diode," *Applied Physics Letters*, vol. 54, pp. 295-297, 1989.

[126] C. R. Giles and E. Desurvire, "Modeling erbium-doped fiber amplifiers," *Journal of Lightwave Technology*, vol. 9, pp. 271-283, 1991.

[127] Y. T. Chieng, G. J. Cowle, and R. A. Minasian, "Optimization of wavelength

tuning of erbium-doped fiber ring lasers," *Journal of Lightwave Technology*, vol. 14, pp. 1730-1739, 1996.

[128] G. J. Cowle, D. N. Payne, and D. Reid, "Single-frequency travelling-wave erbium-doped fibre loop laser," *Electronics Letters*, vol. 27, pp. 229-230, 1991.

[129] I. N. Duling, III, "Subpicosecond all-fibre erbium laser," *Electronics Letters*, vol. 27, pp. 544-545, 1991.

[130] L. Talaverano, S. Abad, S. Jarabo, and M. Lopez-Amo, "Multiwavelength fiber laser sources with Bragg-grating sensor multiplexing capability," *Journal of Lightwave Technology*, vol. 19, pp. 553-558, 2001.

[131] A. T. Alavie, S. E. Karr, A. Othonos, and R. M. Measures, "A Multiplexed Bragg Grating Fiber Laser Sensor System," *IEEE Photonics Technology Letters*, vol. 5, pp. 1112-1114, 1993.

[132] S. M. Melle, A. T. Alavie, S. Karr, T. Coroy, K. X. Liu, and R. M. Measures, "A Bragg Grating-Tuned Fiber Laser Strain Sensor System," *IEEE Photonics Technology Letters*, vol. 5, pp. 263-266, 1993.

[133] A. D. Kersey and W. W. Morey, "Multielement Bragg-Grating Based Fiber-Laser Strain Sensor," *Electronics Letters*, vol. 29, pp. 964-966, 1993.

[134] G. Das and J. W. Y. Lit, "L-band multiwavelength fiber laser using an elliptical fiber," *IEEE Photonics Technology Letters*, vol. 14, pp. 606-608, 2002.

[135] X. P. Dong, S. P. Li, K. S. Chiang, M. N. Ng, and B. C. B. Chu, "Multiwavelength erbium-doped fibre laser based on a high-birefringence fibre loop mirror," *Electronics Letters*, vol. 36, pp. 1609-1610, 2000.

[136] X. W. Shu, S. Jiang, and D. X. Huang, "Fiber grating Sagnac loop and its multiwavelength-laser application," *IEEE Photonics Technology Letters*, vol. 12, pp. 980-982, 2000.

[137] G. J. Cowle and D. Y. Stepanov, "Multiple wavelength generation with brillouin/erbium fiber lasers," *IEEE Photonics Technology Letters*, vol. 8, pp. 1465-1467, 1996.

[138] A. J. Poustie, N. Finlayson, and P. Harper, "Multiwavelength Fiber Laser Using a Spatial Mode Beating Filter," *Optics Letters*, vol. 19, pp. 716-718, 1994.

[139] Y. W. Lee and B. Lee, "Wavelength-switchable erbium-doped fiber ring laser using spectral polarization-dependent loss element," *IEEE Photonics Technology Letters*, vol. 15, pp. 795-797, 2003.

[140] A. Bellemare, M. Karbsek, C. Riviere, F. Babin, G. He, V. Roy, and G. W. Schinn, "A broadly tunable erbium-doped fiber ring laser: experimentation and modeling," *Selected Topics in Quantum Electronics, IEEE Journal of*, vol. 7, pp. 22-29, 2001.

[141] S. Hu, L. Zhan, Y. J. Song, W. Li, S. Y. Luo, and Y. X. Xia, "Switchable multiwavelength erbium-doped fiber ring laser with a multisection high-birefringence fiber loop mirror," *IEEE Photonics Technology Letters*, vol. 17, pp. 1387-1389, 2005.

[142] M. Delgado-Pinar, J. Mora, A. Diez, J. L. Cruz, and M. V. Andres, "Wavelength-switchable fiber laser using acoustic waves," *IEEE Photonics Technology Letters*, vol. 17, pp. 552-554, 2005.

[143] J. Liu, J. P. Yao, J. Yao, and T. H. Yeap, "Single-longitudinal-mode multiwavelength fiber ring laser," *IEEE Photonics Technology Letters*, vol. 16, pp. 1020-1022, 2004.

[144] X. H. Feng, Y. G. Liu, S. G. Fu, S. Z. Yuan, and X. Y. Dong, "Switchable dual-wavelength ytterbium-doped fiber laser based on a few-mode fiber grating," *IEEE Photonics Technology Letters*, vol. 16, pp. 762-764, 2004.

[145] C. L. Zhao, X. F. Yang, C. Lu, N. J. Hong, X. Guo, P. R. Chaudhuri, and X. Y. Dong, "Switchable multi-wavelength erbium-doped fiber lasers by using cascaded fiber Bragg gratings written in high birefringence fiber," *Optics Communications*, vol. 230, pp. 313-317, 2004.

[146] B. A. Yu, J. Kwon, S. Chung, S. W. Seo, and B. Lee, "Multiwavelength-switchable SOA-fibre ring laser using sampled Hi-Bi fibre grating," *Electronics Letters*, vol. 39, pp. 649-650, 2003.

[147] S. P. Reilly, S. W. James, and R. P. Tatam, "Tunable and switchable dual wavelength lasers using optical fibre Bragg grating external cavities," *Electronics Letters*, vol. 38, pp. 1033-1034, 2002.